

1 **Measurement of the Higgs boson**
2 **transverse momentum spectrum in**
3 **the WW decay channel at 8 TeV and**
4 **first results at 13 TeV**

5 Lorenzo Viliani
6 of University of Florence

7 PhD Thesis
8

Abstract

The cross section for Higgs boson production in pp collisions is studied using the $H \rightarrow W^+W^-$ decay mode, followed by leptonic decays of the W bosons, leading to an oppositely charged electron-muon pair in the final state. The measurements are performed using data collected by the CMS experiment at the LHC with pp collisions at a centre-of-mass energy of 8 TeV, corresponding to an integrated luminosity of 19.4 fb^{-1} . The Higgs boson transverse momentum (p_T) is reconstructed using the lepton pair p_T and missing p_T . The differential cross section times branching fraction is measured as a function of the Higgs boson p_T in a fiducial phase space defined to match the experimental acceptance in terms of the lepton kinematics and event topology. The production cross section times branching fraction in the fiducial phase space is measured to be $39 \pm 8\text{ (stat)} \pm 9\text{ (syst)}\text{ fb}$. The measurements are compared to theoretical calculations based on the standard model to which they agree within experimental uncertainties.

²⁵ Contents

²⁶ 1. Electroweak and QCD physics at LHC	³
²⁷ 2. The CMS experiment at the LHC	⁵
2.1. The Large Hadron Collider	5
2.2. The <i>Compact Muon Solenoid</i> experiment	9
2.2.1. The solenoid	12
2.2.2. The tracker	13
2.2.3. The electromagnetic calorimeter (ECAL)	17
2.2.4. The hadron calorimeter (HCAL)	19
2.2.5. The muon system	20
2.3. The CMS trigger system	23
2.3.1. The Level-1 trigger	23
2.3.2. The high level trigger (HLT)	25
2.4. Event reconstruction and particle identification	26
2.4.1. The Particle Flow technique	26
2.4.2. Leptons reconstruction and identification	28
2.4.3. Jets reconstruction and identification	28
2.5. The CMS framework	28
⁴³ 3. Higgs boson properties in the $H \rightarrow WW$ decay channel	²⁹
3.1. Higgs boson phenomenology at LHC	29
3.1.1. Higgs boson production mechanisms	29
3.1.2. Higgs boson decay channels	29
3.2. The $H \rightarrow WW$ decay channel	29
3.2.1. The $H \rightarrow WW \rightarrow 2\ell 2\nu$ signature	29
3.2.2. Physics objects definition	29
3.2.3. Background processes	29
3.3. Experimental results of the Higgs boson measurements	29
⁵² 4. Measurement of the Higgs boson transverse momentum at 8 TeV using $H \rightarrow WW \rightarrow 2\ell 2\nu$ decays	³¹
4.1. Introduction	31
4.2. Data sets, triggers and MC samples	33
4.2.1. Data sets and triggers	33
4.2.2. Monte Carlo samples	35

58	4.3. Analysis Strategy	37
59	4.3.1. Event reconstruction and selections	38
60	4.3.2. Fiducial phase space	41
61	4.3.3. Binning of the p_T^H distribution	41
62	4.4. Background estimation	42
63	4.4.1. Top quark background	42
64	4.4.2. WW background	52
65	4.4.3. Other backgrounds	56
66	4.5. Systematic uncertainties	60
67	4.5.1. Background normalization uncertainties	60
68	4.5.2. Experimental uncertainties	62
69	4.5.3. Theoretical uncertainties	63
70	4.5.4. Statistics uncertainty of the simulated samples	65
71	4.5.5. Treatment of systematic uncertainties in the shape analysis	66
72	4.6. Signal extraction	66
73	4.6.1. Fitting procedure	67
74	4.6.2. Signal and background yields	70
75	4.7. Unfolding	72
76	4.7.1. Treatment of systematic uncertainties	76
77	4.8. Results	78
78	5. Search for the SM Higgs boson in the $H \rightarrow WW$ channel with the first 13 TeV LHC data	83
80	5.1. Introduction	83
81	5.2. Data and simulated samples	83
82	5.3. Analysis strategy	88
83	5.3.1. Event reconstruction	88
84	5.3.2. Event selection and background rejection	93
85	5.3.3. Signal extraction	95
86	5.4. Background estimation	100
87	5.4.1. WW background	100
88	5.4.2. Top quark background	100
89	5.4.3. Jet-induced (or Fake) background	102
90	5.4.4. DY background	102
91	5.4.5. Other backgrounds	103
92	5.5. Systematic uncertainties	104
93	5.6. Results	106
94	6. Search for high mass resonances decaying to a W boson pair with first 13 TeV LHC data	109
95	6.1. Introduction	109
96	6.2. Data and simulated samples	109
97	6.3. Analysis strategy	111

99	6.4. Background estimation	114
100	6.5. Systematic uncertainties	117
101	6.6. Signal extraction and limit setting	117
102	6.7. Results	121
103	7. Conclusions	127
104	A. Fiducial region definition and optimization	129
105	Bibliography	137

Chapter 1.

¹⁰⁷ Electroweak and QCD physics at
¹⁰⁸ LHC

Chapter 2.

¹⁰⁹ The CMS experiment at the LHC

¹¹⁰ In this chapter, the main characteristics of the Large Hadron Collider (LHC particle
¹¹¹ accelerator and Compact Muon Solenoid (CMS) experiment are described.

¹¹² 2.1. The Large Hadron Collider

¹¹³ The LHC [1–4] at CERN, officially inaugurated on 21st October 2008, is the largest and
¹¹⁴ most powerful hadron collider ever built. Installed in the underground tunnel which hosted
¹¹⁵ the Large Electron Positron Collider (LEP) [5–7], the leptonic accelerator in operation until
¹¹⁶ 2nd November 2000, the LHC accelerator has the shape of a circle with a length of about
¹¹⁷ 27 km and is located underground at a depth varying between 50 m to 175 m, straddling the
¹¹⁸ Franco-Swiss border near Geneva. It is designed to collide two 7 TeV counter-circulating
¹¹⁹ beams of protons resulting in a center-of-mass energy of 14 TeV, or two beams of heavy
¹²⁰ ions, in particular lead nuclei at an energy of 2.76 TeV/nucleon in the center-of-mass frame.

¹²¹ The transition from a leptonic collider to a hadronic collider entailed the following
¹²² advantages: first, it has been possible to build a machine that having the same size of the
¹²³ previous one (and therefore accommodated in the same LEP tunnel, substantially reducing
¹²⁴ the cost and time of construction), could reach a higher energy in the center-of-mass
¹²⁵ frame. This is due to the much lower amount of energy loss through synchrotron radiation
¹²⁶ emitted by the accelerated particles, that is proportional to the fourth power of the ratio
¹²⁷ E/m between their energy and their mass. Secondly, the composite structure of protons
¹²⁸ compared to the elementary structure of electrons allows LHC to be able to simultaneously
¹²⁹ access a wider energy spectrum, despite the production of many low energies particles in a
¹³⁰ complex environment. This is a particularly important feature for a machine dedicated to
¹³¹ the discovery of “new” physics.

¹³² In Fig. 2.1 a schematic description of the accelerator complex installed at CERN is shown.
¹³³ The acceleration is performed in several stages [4]. The protons source is a *Duoplasmatron*:
¹³⁴ the protons are obtained by removing electrons from a source of hydrogen gas and then
¹³⁵ sent to the LINAC2, a 36 m long linear accelerator which generates a pulsed beam with
¹³⁶ an energy of 50 MeV using Radio Frequency Quadrupoles (RFQ) and focusing quadrupole
¹³⁷ magnets. The beam is subsequently sent to the Proton Synchrotron Booster (PSB), a
¹³⁸ circular accelerator consisting of four superimposed synchrotron rings with a circumference
¹³⁹ of about 160 m, which increases the proton energy up to 1.4 GeV. Then, protons are

140 injected into the Proton Synchrotron (PS), a single synchrotron ring with a circumference
 141 of about 600 m where the energy is increased to 25 GeV. The sequential combination of
 142 these two synchrotrons also allows to create a series of protons bunches interspersed by
 143 25 ns as required for the correct operation of LHC. The final proton injection stage is the
 144 Super Proton Synchrotron (SPS), a synchrotron with a circumference of approximately
 145 7 km where protons reach an energy value of 450 GeV. Subsequently, protons are extracted
 146 and injected into the LHC ring via two transmission lines, to generate two beams running
 147 in opposite directions in two parallel pipes and which are accelerated up to the energy of
 148 interest. In the two pipes an ultrahigh vacuum condition is maintained (about 10^{-10} Torr)
 149 to avoid the spurious proton interactions with the gas remnants. At full intensity, each
 150 proton beam consists of 2808 bunches and each bunch contains around 10^{11} protons. The
 151 beams are squeezed and collide for a length of about 130 m at four interaction points where
 152 the four main experiments (ALICE, ATLAS, CMS and LHCb) are placed:

- 153 • CMS (Compact Muon Solenoid) [8] and ATLAS (A Toroidal LHC ApparatuS) [9] are
 154 two general-purpose detectors designed to investigate the largest possible spectrum of
 155 physics. In particular, they have been devoted to the detection of particles produced
 156 by a Higgs boson decay and to look for any evidence of possible new physics. The use
 157 of two detectors chasing the same objectives but designed independently is crucial for
 158 a cross-check of any possible new discovery;
- 159 • LHCb (LHC beauty) [10] is an experiment primarily designed to study CP (combined
 160 Charge conjugation and Parity symmetry) violation in electroweak interactions and to
 161 study asymmetries between matter and antimatter through the analysis of rare decays
 162 of hadrons containing b quarks. The detector is also able to perform measurements in
 163 the forward region, at small polar angles with respect to the beam line;
- 164 • ALICE (A Large Ion Collider Experiment) [11] is an experiment studying heavy ions
 165 collisions, through the production of a new state of matter called quark-gluon plasma.

166 Two other smaller experiments are located along the circumference of the LHC accelerator,
 167 TOTEM and LHCf, which focus on particles emitted in the forward direction. TOTEM
 168 (TOTal Elastic and diffractive cross section Measurement) [12] measures the proton-proton
 169 interaction cross section and accurately monitors the luminosity of the LHC using detectors
 170 positioned on either side of the CMS interaction point. LHCf (LHC forward) [13] is made
 171 up of two detectors which sit along the LHC beamline, at 140 m either side of the ATLAS
 172 collision point. It makes use of neutral particles thrown forward by LHC collisions as a
 173 source to simulate the interaction with the atmosphere of very high energy cosmic rays
 174 (between 10^{17} TeV and 10^{20} TeV) in laboratory conditions.

175 A series of about 1200 magnetic dipoles bend the beams along the accelerator ring.
 176 They are located along the “arc” structures of the circumference. The ring, in fact, can
 177 be subdivided into octants, with eight curve regions (the “arcs”) separated by rectilinear
 178 regions. In these straight regions, instead, almost 400 focusing and defocusing quadrupoles
 179 are located, which maintain the beam stable along the orbit, and some other small multipolar
 180 magnets (sextupoles and octupoles) are used to make additional minor corrections to the
 181 beam direction. A radio frequency acceleration system, consisting of 16 superconducting

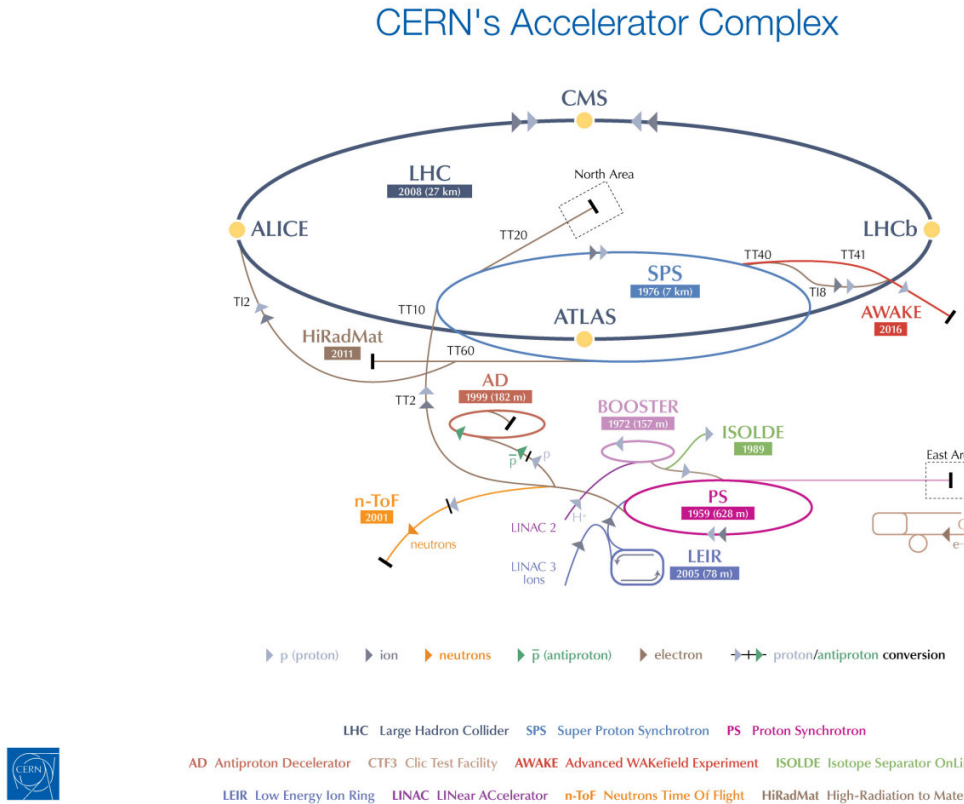


Figure 2.1.: Schematic description of the accelerator complex installed at CERN.

radio-frequency resonant cavities, is used to increase the proton energy by 0.5 MeV with each beam revolution. The 7 TeV per-beam-energy limit on the LHC is not determined by the electric field generated by the radiofrequency cavity but by the magnetic field necessary to maintain the protons in orbit, given the current technology for the superconducting magnets, which is about 5.4 T on average.

One of the most important parameters of an accelerator is the instantaneous luminosity \mathcal{L} , which gives a measure of the rate of events one can expect given the process cross section. In fact, for a given physics process with cross section σ , producing N events for unit of time, the instantaneous luminosity is defined by the following equation:

$$N = \sigma \mathcal{L} \quad . \quad (2.1)$$

The LHC design luminosity is $\mathcal{L} = 10^{34} \text{ cm}^{-2} \text{s}^{-1}$, leading to around 1 billion proton interactions per second.

¹⁹³ The instantaneous luminosity is a parameter which depends on the construction charac-
¹⁹⁴ teristics of the accelerator, and can be expressed by the following approximated formula:

$$\mathcal{L} = f \frac{n_1 n_2}{4\pi\sigma_x\sigma_y} , \quad (2.2)$$

¹⁹⁵ where n_1 and n_2 are the number of particles contained in the two bunches colliding at
¹⁹⁶ a frequency f , and σ_x and σ_y are the beam sizes in the transverse plane. At LHC, the
¹⁹⁷ bunches collide with $f = 40$ MHz and the transverse size of the beam can be squeezed down
¹⁹⁸ to around 15 μm . Then, the integrated luminosity L is defined as the time integral of the
¹⁹⁹ instantaneous luminosity:

$$L = \int \mathcal{L} dt . \quad (2.3)$$

²⁰⁰ The main parameters of the LHC machine are listed in Table 2.1.

²⁰¹ The LHC started to be operative in September 2008 but, due to a faulty interconnection
²⁰² between two magnets which caused a helium leakage in the tunnel, the operation was
²⁰³ stopped and restarted in March 2010. During 2010 and 2011 LHC ran successfully and
²⁰⁴ provided proton proton collisions at a center-of-mass energy of 7 TeV, delivering a total
²⁰⁵ integrated luminosity of about 6.1 fb^{-1} . The encouraging results in the Higgs boson search
²⁰⁶ provided by the ATLAS and CMS Collaborations led to the decision of extending the data
²⁰⁷ taking period to the end of 2012, and to increase the center-of-mass energy up to 8 TeV.
²⁰⁸ During 2012, LHC delivered to the experiments an integrated luminosity of 23.3 fb^{-1} . After
²⁰⁹ the first long shutdown (LS1), a two years period started in the early 2013 where the LHC
²¹⁰ operation stopped for maintenance and upgrade, the LHC started again delivering proton
²¹¹ proton collisions on 3rd June 2015, at the new record center-of-mass energy of 13 TeV.
²¹² During the 2015 the LHC delivered an integrated luminosity of 4.2 fb^{-1} . Nowadays, LHC is
²¹³ still colliding bunches of protons at $\sqrt{s} = 13 \text{ TeV}$, reaching unprecedented instantaneous
²¹⁴ luminosities and delivering a total integrated luminosity of 31 fb^{-1} . The cumulative delivered
²¹⁵ luminosity versus time for the different LHC data taking periods is shown in Fig. 2.2.

²¹⁶ As the instantaneous luminosity increases, the probability of multiple proton proton
²¹⁷ interactions to occur in a single bunch crossing grows higher as well. In this instance, the
²¹⁸ main goal is the identification and reconstruction of a single primary collision where the
²¹⁹ physics event of interest occurs among the background of the additional proton proton
²²⁰ interactions. Such backgrounds are due to processes occurring with very high probability,
²²¹ like the production of low- p_T jets. These additional collisions are known as pile up (PU).
²²² During the LHC current run the average number of pile up events is 23, with some event
²²³ exhibiting over 45 pile up collisions.

Table 2.1.: LHC technical parameters for proton proton collisions.

Parameter	Value
Maximum dipole magnetic field	8.33 T
Dipole operating temperature	1.9 K
Beam energy at injection	450 GeV
Beam energy at collision (nominal)	7 TeV
Beam energy at collision (2012)	4 TeV
Beam energy at collision (2015–2016)	6.5 TeV
Maximum instantaneous luminosity (nominal)	$10^{34} \text{ cm}^{-2}\text{s}^{-1}$
Maximum instantaneous luminosity (2012)	$7.7 \cdot 10^{33} \text{ cm}^{-2}\text{s}^{-1}$
Maximum instantaneous luminosity (2015–2016)	$1.2 \cdot 10^{34} \text{ cm}^{-2}\text{s}^{-1}$
Number of bunches per proton beam (nominal)	2808
Number of bunches per proton beam (2012)	1380
Number of bunches per proton beam (2015–2016)	2220
Maximum number of protons per bunch	$1.69 \cdot 10^{11}$
Bunch separation in time (nominal)	25 ns
Bunch separation in time (2012)	50 ns
Bunch separation in time (2015–2016)	25 ns
Collision frequency (nominal)	40 MHz
Collision frequency (2012)	20 MHz
Collision frequency (2015–2016)	40 MHz
Energy loss per turn at 14 TeV	7 keV

2.2. The *Compact Muon Solenoid* experiment

The CMS apparatus is a general purpose detector situated in one of the four LHC interaction points¹. The detector is designed to investigate a wide range of physics, from the search of the Higgs boson, to SM measurements and BSM physics searches. To achieve this goal, the detector is able to identify and reconstruct all the physics objects that may be produced in the proton proton collisions: electrons, muons, photons and jets. The main feature of the CMS detector is a superconducting solenoidal magnet which is capable to produce a

¹The CMS detector is placed in a cavern 100 m underground in the area called Point 5, near the village of Cessy, in France.

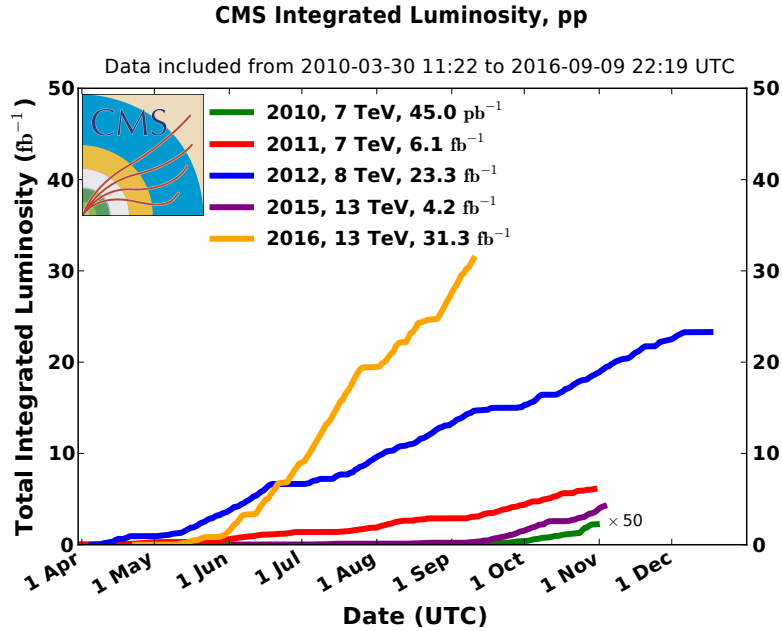


Figure 2.2.: Cumulative luminosity versus day delivered to CMS during proton proton collisions.

3.8 T magnetic field. Such a strong magnetic field is the key aspect which permits to have a compact design of the detector. The detector has a cylindrical structure, which is typical of general purpose detectors, which consists of several cylindrical detecting layers, coaxial with the beam direction (*barrel* region), closed at both ends with detecting disks (*endcap* region), in such a way to ensure the hermetic closure of the apparatus.

The coordinate system used by CMS is a right-handed Cartesian system, with the origin at the center of the detector, in the nominal beam collision point. The x -axis is chosen to point radially towards the center of the LHC circumference and the y -axis is directed upwards along the vertical. The z -axis is oriented along the beam direction, according to the anticlockwise direction of the LHC ring if seen from above. The CMS cylindrical symmetry and the Lorentz invariant description of the proton proton collisions, suggest the use of a pseudo-angular reference frame, described by the triplet of coordinates (r, ϕ, η) , where r is the distance from the z -axis, ϕ is the azimuthal angle, measured starting from the x -axis positive direction, and η is the pseudorapidity, defined by the following equation:

$$\eta = -\ln \left(\tan \frac{\theta}{2} \right) \quad , \quad (2.4)$$

where θ is the polar angle. The use of pseudorapidity is preferred over the polar angle because differences in pseudorapidity are Lorentz invariant under boosts along the z -axis.

²⁴⁷ In the limit of ultrarelativistic particles the pseudorapidity coincides with the rapidity y :

$$y = \frac{1}{2} \ln \left(\frac{E + p_z}{E - p_z} \right) \quad , \quad (2.5)$$

²⁴⁸ where E is the particle energy and p_z is the momentum projection along the z -axis.

²⁴⁹ The schematic view of the CMS detector, which has a length of 21.5 m, a diameter of
²⁵⁰ 15 m and a weight of about 14000 tons, is shown in Fig. 2.3. From the inner region to the
²⁵¹ outer one, the various CMS sub-detectors are:

- **Silicon tracker:** it occupies the region $r < 1.2$ m and $|\eta| < 2.5$. It is composed of an inner silicon pixel vertex detector and a surrounding silicon microstrip detector, with a total active area of about 215 m². It is used to reconstruct charged particle tracks and vertices;
- **Electromagnetic calorimeter (ECAL):** placed in the region $1.2 \text{ m} < r < 1.8 \text{ m}$ and $|\eta| < 3$, it consists of many scintillating crystals of lead tungstate (PbWO_4). It is used for the measurement of the trajectory and the energy released by electrons and photons;
- **Hadronic calorimeter (HCAL):** it is placed in the region $1.8 \text{ m} < r < 2.9 \text{ m}$ and $|\eta| < 5$. It is made up of brass layers alternated with plastic scintillators and it is used to measure the direction and energy deposited by the hadrons produced in the interactions;
- **Superconducting solenoidal magnet:** it occupies the region $2.9 \text{ m} < r < 3.8 \text{ m}$ and $|\eta| < 1.5$ and generates an internal uniform magnetic field with an intensity of 3.8 T, pointing along the direction of the beams. The magnetic field is necessary to bend the trajectories of charged particles, in order to allow the measurement of their momentum through the curvature observed in the tracking system. The magnetic field lines are closed by an external 21 m long iron yoke, that has a diameter of 14 m. Outside the return yoke, a residual 1.8 T magnetic field is present, pointing in the opposite direction with respect to the internal field;
- **Muon system:** the outermost system, which is placed in the region $4 \text{ m} < r < 7.4 \text{ m}$ and $|\eta| < 2.4$, has the purpose of reconstructing the tracks of muons passing through it. It consists of Drift Tubes (DT) in the barrel region and Cathode Strip Chambers (CSC) in the endcaps. A complementary system of Resistive Plate Chambers (RPC) is used both in the barrel and endcaps. The muon chambers are housed inside the iron structure of the return yoke.

²⁷⁸ In Fig. 2.4 the response of the various CMS sub-detectors to the passage of different types
²⁷⁹ of particles is sketched. In the following sections a brief description of each sub-detector is
²⁸⁰ given.

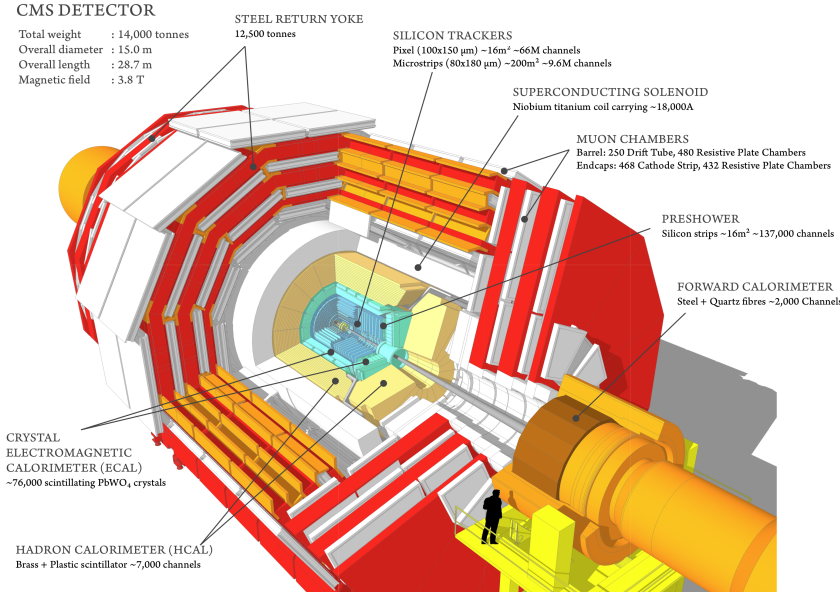


Figure 2.3.: Schematic view of the CMS detector showing its sub-detectors.

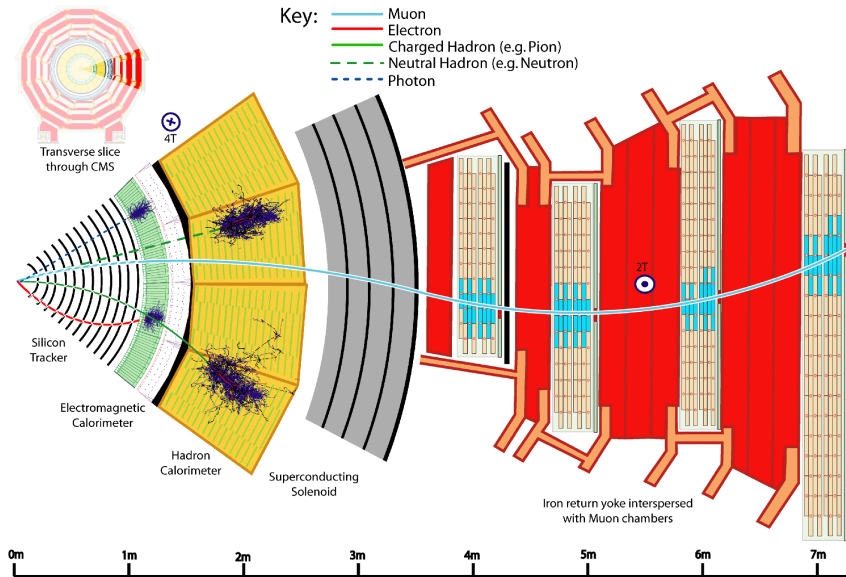


Figure 2.4.: Schematic view of a slice of the CMS detector, showing the sub-detectors response to the passage of different types of particles.

2.2.1. The solenoid

The CMS magnet [14], which contains the tracker, the electromagnetic and the hadronic calorimeters, is the biggest superconducting solenoid ever built. The solenoid can generate a magnetic field of 3.8 T in the internal bore, which has a diameter of 6 m and a length of

285 12.5 m. The energy stored in the magnet is about 2.7 GJ at full current. The superconductor
 286 is made of four Niobium-Titanium layers and it is cooled down to about 4 K through a
 287 liquid Helium cooling plant. In case of a quench, when the magnet loses its superconducting
 288 property, the energy is dumped to resistors within 200 ms. The magnet return yoke of
 289 the barrel is composed with three sections along the z -axis; each one is split into 4 layers
 290 (holding the muon chambers in the gaps). Most of the iron volume is saturated or nearly
 291 saturated, and the field in the yoke is about the half (1.8 T) of the field in the central
 292 volume.

293 2.2.2. The tracker

294 The silicon tracker is the detector closest to the beam collision point. Its goal is the
 295 high resolution reconstruction of the trajectories of charged particles originating from the
 296 interaction point and the identification of the position of secondary vertices produced by
 297 particles with a short mean life time (in particular hadrons containing the b quark, that
 298 decay after few hundred of μm). The events produced in the proton proton collisions can
 299 be very complex and track reconstruction is an entangled pattern recognition problem.
 300 Indeed, at the nominal instantaneous luminosity of operation, an average of about 20 pile up
 301 events overlapping to the event of interest are expected, leading to about 1000 tracks to be
 302 reconstructed every 25 ns. In order to make the pattern recognition easier, two requirements
 303 are fundamental:

- 304 • a low occupancy detector;
- 305 • a large redundancy of the measured points (*hits*) per track.

306 The first requirement is achieved building a detector with high granularity². The redundancy
 307 of the hits is instead achieved having several detecting layers, and is necessary to reduce the
 308 ambiguity on the assignment of the hits to a given track. Nevertheless, the amount of tracker
 309 material has to be as low as possible, in order to avoid compromising the measurement
 310 of the particle trajectory. An excessive amount of material would indeed deteriorate the
 311 measurement, mainly because of the increased probability of particle multiple scattering.
 312 The outer detectors such as ECAL would be influenced by the material as well, for example
 313 because of the increased probability for a photon to convert to an electron-positron pair
 314 in the tracker material. For this reasons, the tracker layers are limited in number and
 315 thickness.

316 The tracker comprises a large silicon strip detector with a small silicon pixel detector
 317 inside it. In the central η region, the pixel tracker consists of three co-axial barrel layers at
 318 radii between 4.4 cm and 10.2 cm and the strip tracker consists of ten co-axial barrel layers
 319 extending outwards to a radius of 110 cm. Both sub-detectors are completed by endcaps on
 320 either side of the barrel, each consisting of two disks in the pixel tracker, and three small
 321 plus nine large disks in the strip tracker. The endcaps extend the acceptance of the tracker

²The granularity of a detector is defined as the angular range ($\Delta\eta \times \Delta\phi$) that each individual element is able to resolve.

up to $|\eta| < 2.5$. A three-dimensional schematic view of the tracker is shown in Fig. 2.5, while in Fig. 2.6 a pictorial representation of a slice of the tracker is displayed, showing the various layers of the sub-detectors.

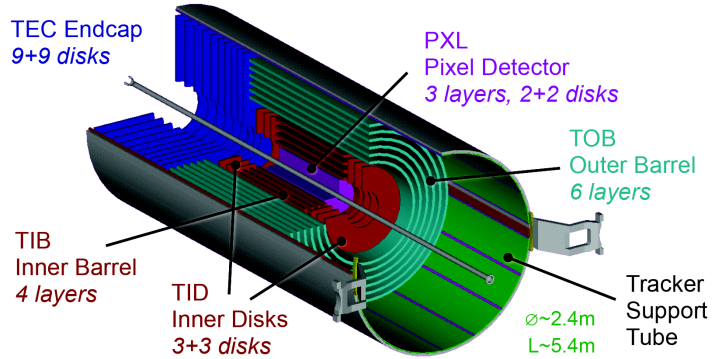


Figure 2.5.: Three-dimensional schematic view of the CMS silicon tracker.

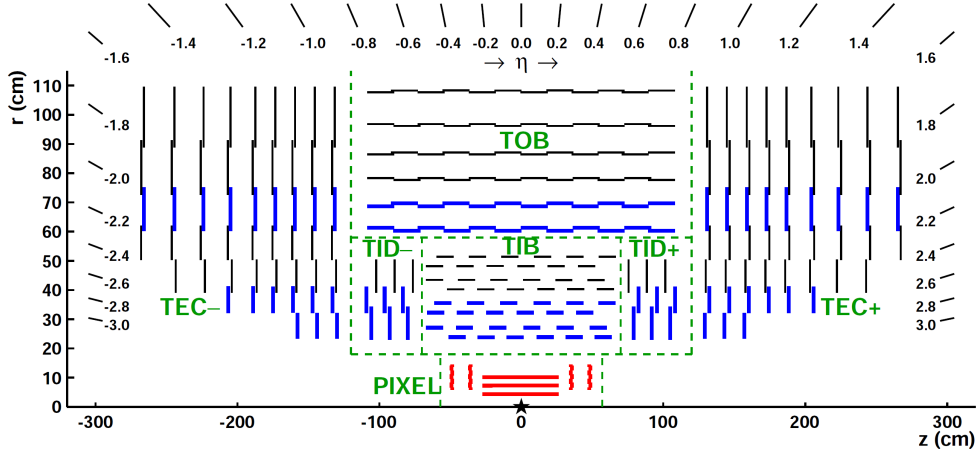


Figure 2.6.: Pictorial view of a tracker slice in the r - z plane. Pixel modules are shown in red, single-sided strip modules are depicted as black thin lines and strip stereo modules are shown as blue thick lines.

The whole tracker has a cylindrical shape with a length of 5.8 m and a diameter of 2.5 m, with the axis aligned to the beams direction. The average number of hits per track is 12-14, in order to have a high reconstruction efficiency and a low rate of fake tracks.

The material budget of the tracker as obtained from a simulation of the detector is shown in Fig. 2.7, reported both in units of radiation length t/X_0 and in units of nuclear interaction length t/λ_I , as a function of η . The region $1 < |\eta| < 2$ exhibits a larger material budget due to the presence of cables and services.

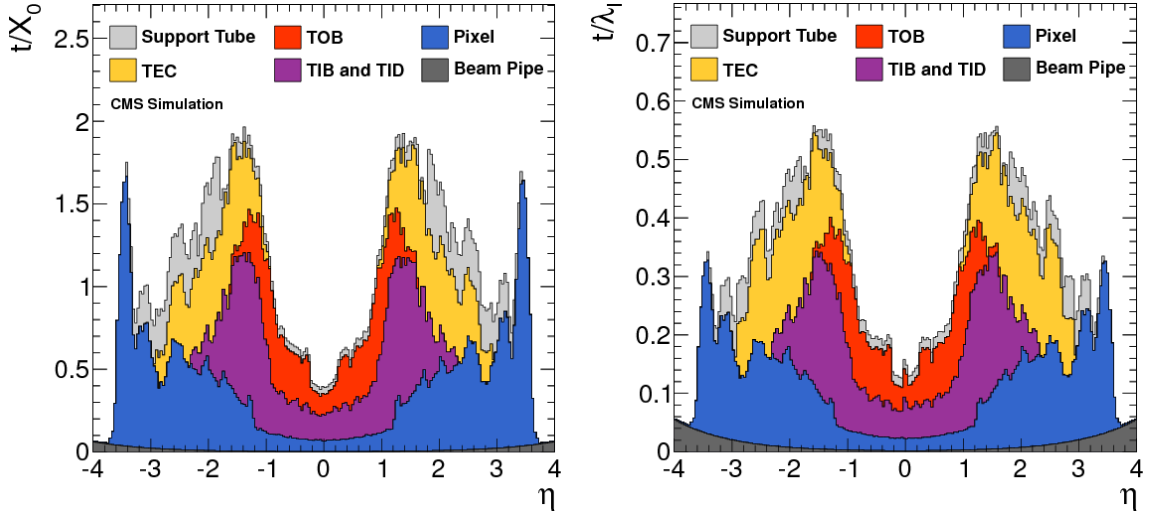


Figure 2.7.: Total thickness t of the tracker material expressed in units of X_0 (left) and λ_I (right), as a function of η . The contribution to the total material budget of each part of the detector is shown.

332 The pixel detector

333 The pixel detector, shown in Fig. 2.8, is mainly used as starting point in the CMS track
 334 reconstruction and is of fundamental importance for the reconstruction of primary and
 secondary vertices. The pixel detector is placed in the closest position to the collision point,

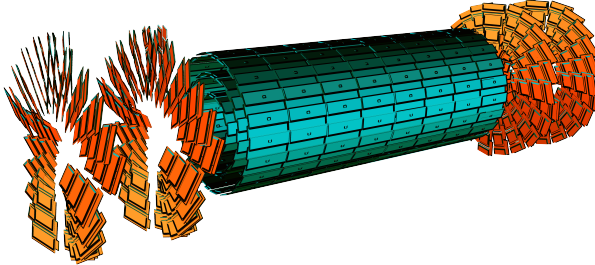


Figure 2.8.: Schematic view of the CMS pixel detector.

335 where the amount of radiation is larger. It is placed in the region $|\eta| < 2.5$ and consists of
 336 three cylindrical layers 53 cm long in the barrel region, located at $r = 4.4, 7.3$ and 10.2 cm,
 337 and two pairs of endcap disks with radii between 6 and 15 cm at $z = \pm 34.5$ and ± 46.5 cm,
 338 covering a total area of about 1 m^2 . The detector is composed of many modules, for a total
 339 of 768 in the barrel and 672 in the endcaps. Each endcap is composed of 24 segments,
 340 each one tilted with respect to the adjacent ones and containing 7 modules. Each module
 341 consists of several units which contain a highly segmented silicon sensor with a thickness of
 342 250 μm . In order to achieve an optimal vertex position resolution in both the (r, ϕ) and
 343

³⁴⁴ z -coordinates, a design with a rectangular pixel shape with an area of $150 \times 100 \mu\text{m}^2$ was
³⁴⁵ adopted, with the $100 \mu\text{m}$ size oriented along the (r, ϕ) direction in the barrel region, and
³⁴⁶ along the z -direction in the endcap region. The achievable hit reconstruction resolution is
³⁴⁷ about $10 - 15 \mu\text{m}$ in the barrel and $15 \mu\text{m}$ in the endcaps.

³⁴⁸ The microstrip detector

³⁴⁹ In this region of the detector the radiation flow is low enough to allow the use of a
³⁵⁰ less segmented device, such as the silicon microstrip detector. The microstrip tracker is
³⁵¹ composed of 15148 silicon modules, covering a total area of about 193 m^2 with a total of
³⁵² 9.3 million strips. Two types of modules are installed: single sided modules consist of one
³⁵³ sensor stucked onto a carbon fiber support together with the readout electronics, with the
³⁵⁴ silicon strips laying along the z direction in the barrel and along the (r, ϕ) direction in the
³⁵⁵ endcaps. The other type of module, referred to as stereo-module, consists of two sensors
³⁵⁶ stucked together back to back and tilted of a relative angle of 100 mrad. This combination
³⁵⁷ allows a three-dimensional measurement of the particle interaction point, providing the
³⁵⁸ information along the z -direction. The whole microstrip tracker is 5.4 m long and extends
³⁵⁹ up to $r = 1.1 \text{ m}$. As the pixel detector, the microstrip detector consists of a barrel and an
³⁶⁰ endcap region and is divided into four distinct parts, as shown in Fig. 2.6. The barrel is
³⁶¹ made up of the following parts:

- ³⁶² • TIB (*Tracker Inner Barrel*): it consists of four cylindrical coaxial layers, covering the
³⁶³ region up to $|z| < 65 \text{ cm}$. In this region the detectors have a thickness of $300 \mu\text{m}$ and
³⁶⁴ the strips are separated by a variable pitch between 80 and $120 \mu\text{m}$. The first two
³⁶⁵ layers are composed of stereo modules while the other layers have single-sided modules.
³⁶⁶ Since the strips are oriented along the z axis, the position resolution is more precise
³⁶⁷ in the (r, ϕ) direction, about $23 - 34 \mu\text{m}$, with respect to the z direction, where a
³⁶⁸ resolution of about $230 \mu\text{m}$ is obtained thanks to the stereo modules.
- ³⁶⁹ • TOB (*Tracker Outer Barrel*): it consists of six cylindrical coaxial layers, placed in the
³⁷⁰ region $55 \text{ cm} < r < 65 \text{ cm}$ and $|z| < 110 \text{ cm}$. Stereo modules are mounted on the two
³⁷¹ inner layers. Since the density of particles passing through this region is lower with
³⁷² respect to the TIB, the pitch between the strips is larger ($120 - 180 \mu\text{m}$) and the
³⁷³ strips are longer (190 mm). The spatial resolution varies in the range $25 - 52 \mu\text{m}$ in
³⁷⁴ the (r, ϕ) direction, and is about $530 \mu\text{m}$ in the z coordinate in the stereo modules.

³⁷⁵ The endcaps are also made up of two parts:

- ³⁷⁶ • TID (*Tracker Inner Disk*): it consists of six disks, three per side, placed orthogonally
³⁷⁷ with respect to the beam axis, between the TIB and the TOB. The modules are
³⁷⁸ positioned in a ring shape, with the strips oriented in the radial direction, and they
³⁷⁹ are alternately placed on the internal and on the external side of the disk. The two
³⁸⁰ innermost rings of the TID are equipped with stereo modules. The thickness of the
³⁸¹ silicon is $300 \mu\text{m}$.
- ³⁸² • TEC (*Tracker EndCap*): each one of the two TEC is made of nine disks which extend
³⁸³ to the region $120 \text{ cm} < |z| < 280 \text{ cm}$. Each disk is divided into 8 slices in each of which

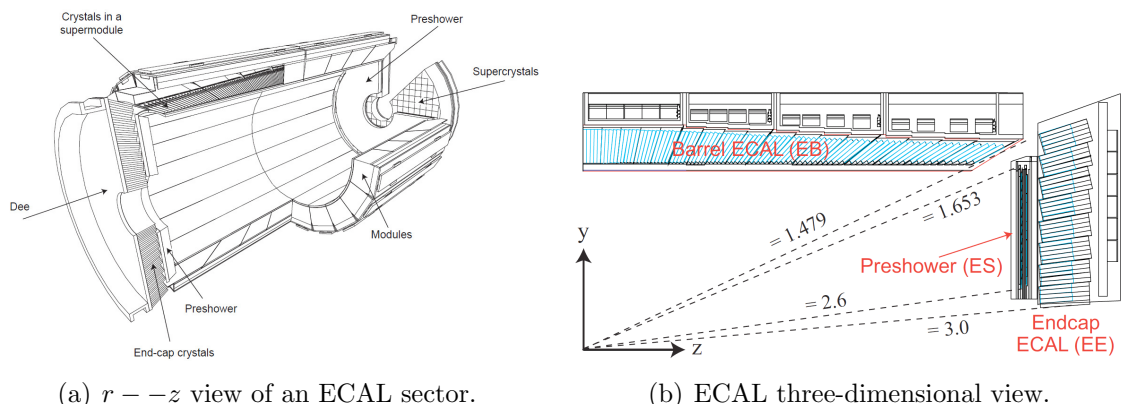
a number ranging from 4 to 7 modules are mounted in a ring shape, depending on the position along z . Also in this case the modules are alternately mounted on the internal and on the external side of the disk, with the strips radially oriented. On the two innermost rings and on the fifth one the stereo modules are installed to measure the z coordinate. The thickness of the sensors range between 300 and 500 μm depending on the disk.

The tracker is operated at low temperature in order to reduce those radiation damage induced effects that have a temperature dependence, such as the increase of the leakage current and the long-term increase of the depletion voltage (also called reverse annealing)³.

The alignment of the tracker modules is very important to obtain a high spatial resolution. Deviations are caused by assembly inaccuracy, deformations due to cooling and stress from the magnetic field. Therefore, three methods are used for the tracker alignment. The geometry was determined during the assembly to an accuracy of 80 to 150 μm . An infrared laser system is used for continuous monitoring of the position of selected tracker modules. The final alignment is done with tracks from well known physics processes, e.g. cosmic muons or muon pairs from the J/Ψ , Υ or Z decays.

2.2.3. The electromagnetic calorimeter (ECAL)

The main function of an electromagnetic calorimeter is to identify electrons and photons and to measure accurately their energy. The CMS electromagnetic calorimeter (ECAL) [15, 16], shown in Fig. 2.9, is a hermetic homogeneous calorimeter with cylindrical geometry, composed of many scintillating crystals of lead tungstate (PbWO_4) with a truncated pyramidal shape. As the other detectors it consists of two parts, the ECAL barrel (EB), which contains 61200 crystals, and two endcaps (EE) containing 7324 crystals each one.



(a) $r - z$ view of an ECAL sector.

(b) ECAL three-dimensional view.

Figure 2.9.: Schematic representation of the CMS electromagnetic calorimeter.

³The tracker in Run 1 was operated at a temperature of +4°C, but during the Long Shutdown 1 a new cooling dry gas plant has been installed and the tracker is now operating at the lower temperature of -15°C.

The characteristics of the PbWO₄ crystals make them an appropriate choice for operation at LHC. The high density ($\rho = 8.3 \text{ g/cm}^3$), short radiation length ($X_0 = 0.89 \text{ cm}$) and small Molière radius⁴ (2.2 cm) allow to build a compact and high granularity calorimeter. Another advantage of this material is the radiation hardness and the fast scintillation decay time ($\tau = 10 \text{ ns}$), that permits to collect about 80% of the produced light within the 25 ns interval between two consecutive bunch crossings. The main drawbacks of this material are the low light yield ($\sim 10 \text{ photoelectrons/MeV}$) and the strong dependence on the operating temperature, that makes it necessary to keep the crystals at a stabilized temperature (18°C).

The crystals are grouped into 5×5 matrices called *towers*. The barrel has an inner radius of 129 cm, a length of 630 cm and extends in the region $|\eta| < 1.479$. The crystals in the barrel have the following dimensions: $22 \times 22 \text{ mm}^2$ at the front face, $26 \times 26 \text{ cm}^2$ at the rear face, and a length of 23 cm, corresponding to $25.8X_0$, and are mounted in a quasi-projective geometry, in order to have the long side tilted by 3° with respect to the direction pointing to the interaction point, both in the η and ϕ coordinates. This is done to avoid the empty spaces between adjacent crystals to be aligned with the direction pointing to the interaction point. The granularity of the EB is about 1°. Avalanche photodiodes (APDs) are used as photodetectors connected with the crystals in the barrel region.

Each endcap covers the region $1.479 < |\eta| < 3$ and is formed by two semicircular aluminium halves called *dees*. Crystals in endcaps have a length of 22 cm, a frontal area equal to $28.6 \times 28.6 \text{ mm}^2$ and a rear surface of $30 \times 30 \text{ mm}^2$. In the endcaps the crystals are arranged in a $\eta - \phi$ symmetry. The photodetectors used to collect the light produced in the endcap crystals are single stage vacuum phototriodes (VPTs), because this region experiences a rather high particle flux and VPTs are more robust against radiation damages with respect to APDs. A preshower system is installed in front of the ECAL endcaps in order to separate the showers produced by a primary γ from those produced by forward emitted π^0 . This detector, which covers the region $1.653 < |\eta| < 2.6$, is a sampling calorimeter consisting of two lead disks ($2X_0$ and $1X_0$ thick respectively) that initiate the electromagnetic shower from incoming photons or electrons, with silicon strip sensors after each disk, which measure the deposited energy as well as the shower transverse profile.

The energy resolution of a homogeneous calorimeter can be expressed by the sum in quadrature of three terms, as shown in the following formula:

$$\left(\frac{\sigma_E}{E}\right)^2 = \left(\frac{a}{\sqrt{E}}\right)^2 + \left(\frac{b}{E}\right)^2 + c^2 \quad (2.6)$$

The stochastic term a dominates at low energies: it includes the contribution of statistical fluctuations in the number of generated and collected photoelectrons. This term takes into account the crystal light emission, the light collection efficiency and the photodetector

⁴The Molière radius R_M characterizes the transverse development of an electromagnetic shower in a calorimeter. On average 90% of the energy deposited by a shower is contained inside a cylinder with radius R_M .

⁴⁴² quantum efficiency⁵. The noise term b includes the contributions of pile up events and
⁴⁴³ electronic noise, both due to the photodetector and preamplifier. These contributions
⁴⁴⁴ depend on η and on the LHC operational luminosity. The constant term c , dominant at
⁴⁴⁵ high energies, takes into account several contributions. The most relevant are the non-
⁴⁴⁶ uniformity of the longitudinal light collection, the intercalibration errors and the leakage
⁴⁴⁷ of energy from the rear side of the crystal. The ECAL barrel resolution for electrons was
⁴⁴⁸ measured using test beams to be:

$$\left(\frac{\sigma_E}{E}\right)^2 = \left(\frac{2.8\% \text{ GeV}^{1/2}}{\sqrt{E}}\right)^2 + \left(\frac{12\% \text{ GeV}^{1/2}}{E}\right)^2 + (0.3\%)^2 , \quad (2.7)$$

⁴⁴⁹ where E is the energy measured in GeV.

⁴⁵⁰ 2.2.4. The hadron calorimeter (HCAL)

⁴⁵¹ The hadron calorimeter (HCAL) [17] is used together with ECAL to make a complete
⁴⁵² calorimetric system for the jet energy and direction measurement. Moreover, thanks
⁴⁵³ to its hermetic structure, it can measure the energy imbalance in the transverse plane,
⁴⁵⁴ E_T^{miss} , a typical signature of non interacting particles, such as neutrinos. The HCAL is
⁴⁵⁵ a sampling calorimeter covering the region $|\eta| < 5$. As shown in Fig. 2.10, it is divided
⁴⁵⁶ in four sub-detectors: HB (*Barrel Hadronic Calorimeter*), located in the barrel region
⁴⁵⁷ inside the solenoid, extending up to $|\eta| < 1.4$; HE (*Endcap Hadronic Calorimeter*), placed
⁴⁵⁸ in the endcaps region inside the magnet, covering the region $1.3 < |\eta| < 3$ and partially
⁴⁵⁹ overlapping with the HB coverage; HO (*Outer Hadronic Calorimeter*), also known as
⁴⁶⁰ *tail-catcher*, placed along the inner wall of the magnetic field return yoke, just outside of
⁴⁶¹ the magnet; HF (*Forward Hadronic Calorimeter*), a sampling calorimeter consisting of
⁴⁶² quartz fibers sandwiched between iron absorbers, consisting of two units placed in the very
⁴⁶³ forward region ($3 < |\eta| < 5$) outside the magnetic coil. The quartz fibers emit Cherenkov
⁴⁶⁴ light with the passage of charged particles and this light is detected by radiation resistant
⁴⁶⁵ photomultipliers. In order to maximize particle containment for a precise missing transverse
⁴⁶⁶ energy measurement, the amount of absorber material was maximized, reducing therefore
⁴⁶⁷ the amount of the active material. Since HCAL is mostly placed inside the magnetic coil,
⁴⁶⁸ a non-magnetic material like brass was chosen as absorber. HB and HE are therefore
⁴⁶⁹ made with 5 cm brass absorber layers interleaved with 3.7 mm plastic scintillators. The
⁴⁷⁰ scintillation light is collected by wavelength shifting (WLS) fibres and read out by hybrid
⁴⁷¹ photodiodes (HPD). The granularity of the calorimeter is $\Delta\eta \times \Delta\phi = 0.087 \times 0.087$ for
⁴⁷² $|\eta| < 1.6$ and $\Delta\eta \times \Delta\phi \approx 0.17 \times 0.17$ for $|\eta| \geq 1.6$. HO is made of 5 rings installed in
⁴⁷³ the wheel that compose the return yoke and is divided in 12 sectors, each one covering
⁴⁷⁴ a 30° angle in ϕ . It consists of scintillating layers, with the same granularity as HB, and
⁴⁷⁵ the solenoid coil is used as an additional absorber to increase the effective depth of the

⁵The quantum efficiency is the ratio between the number of collected electron-hole pairs (or photoelectrons)
and the number of photons incident on the photodetector.



Figure 2.10.: Longitudinal view of the CMS detector showing the HCAL sub-detectors.

476 calorimeter in the barrel region, which is extended up to $11.8 \lambda_I$, thus improving the energy
477 resolution.

478 The energy resolution in the different regions of HCAL can be parametrized using a
479 stochastic and a constant term, as follows:

$$\begin{aligned} \left(\frac{\sigma_E}{E}\right)^2 &= \left(\frac{90\% \text{GeV}^{1/2}}{\sqrt{E}}\right)^2 + (4.5\%)^2 && \text{in the barrel/endcap ,} \\ \left(\frac{\sigma_E}{E}\right)^2 &= \left(\frac{172\% \text{GeV}^{1/2}}{\sqrt{E}}\right)^2 + (9\%)^2 && \text{in the HF ,} \end{aligned} \quad (2.8)$$

480 where E is expressed in GeV.

481 2.2.5. The muon system

482 The CMS muon system [18] is dedicated to the identification and measure of high p_T muons,
483 in combination with the tracker. The system is placed outside the magnetic coil, embedded
484 in the return yoke, to fully exploit the 1.8 T return flux. As shown in Fig. 2.11, the system
485 consists of three types of independent gaseous particle detectors:

- 486 • *Drift Tubes* (DT) are placed in the barrel region, where the occupancy is relatively
487 low ($< 10 \text{ Hz/m}^2$);
- 488 • *Cathode Strip Chambers* (CSC) are installed in the endcaps, where the occupancy is
489 higher ($> 100 \text{ Hz/m}^2$);
- 490 • *Resistive Plate Chambers* (RPC) are placed both in the barrel and endcaps.

491 The DT system is placed in the region of the barrel with $|\eta| < 1.2$, where the magnetic
492 field is sufficiently weak and homogeneous. Along the longitudinal direction, the barrel

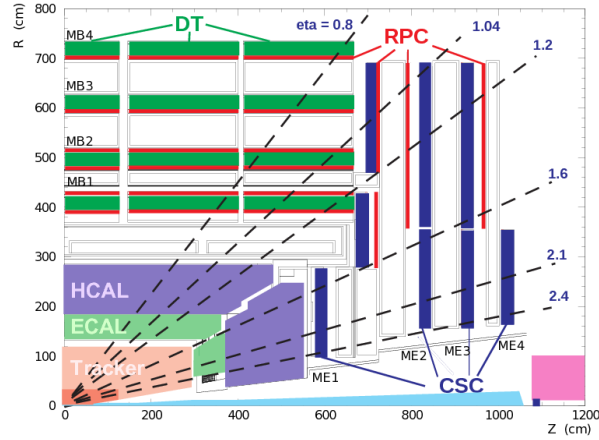


Figure 2.11.: Schematic view of a quadrant of the CMS muon system.

region is divided in 5 wheels, which are subdivided in 12 sectors covering a 30° azimuthal angle each. The wheels are composed of 4 concentric rings of chambers, called *stations*, interspersed in the layers of the iron return yoke, and each one formed by 12 DT chambers. The basic element of the DT system is a rectangular drift tube cell with a transverse size of $13 \times 42 \text{ mm}^2$ and a variable length from 2 to 4 m. The chambers are filled with a gas mixture of Ar (85%) and CO₂ (15%) and are grouped in the radial direction to form detection layers. Groups of four layers form a *superlayer*. In each superlayer two chambers have anode wires parallel to the beam axis and two have perpendicular wires, thus providing two measurements of the (r, ϕ) coordinate and two measurements of the z coordinate of the track hit positions. As shown in Fig. 2.12, each chamber is made of a stainless steel anode

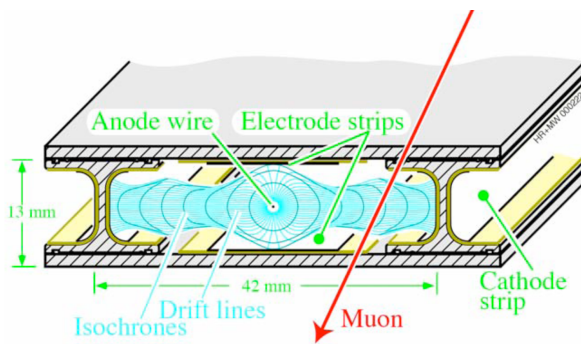


Figure 2.12.: Schematic representation of a drift tube chamber, showing the drift lines in presence of magnetic field.

wire between two parallel aluminium plates with “T” shaped spacer cathodes, isolated from the aluminium plates with polycarbonate plastic, and the hit resolution is about $100 \mu\text{m}$ in both (r, ϕ) and (r, z) directions.

506 In the endcaps, the high and non-uniform magnetic field and the particle rate do not
 507 allow to use drift tubes detectors to perform measurements. Therefore, a solution based
 508 on the CSC detector has been adopted. CSC are multi-wire proportional chambers with
 509 the cathodes segmented into strips oriented radially and transversely with respect to the
 510 anode wires (see Fig. 2.13), allowing a simultaneous measurement of two coordinates (r
 511 through the wires and ϕ using the strips). The CSC chambers are filled with a gas mixture
 512 of Ar (40%), CO₂ (50%) and CF₄ (10%) and provide a spatial resolution of about 80–85 μm .
 513 The drift path of the charge carriers is shorter with respect to the drift tubes, therefore
 514 these detectors can be placed in regions with higher flows of charged particles and less
 homogeneous magnetic fields. The CSC coverage is $0.8 < |\eta| < 2.4$.

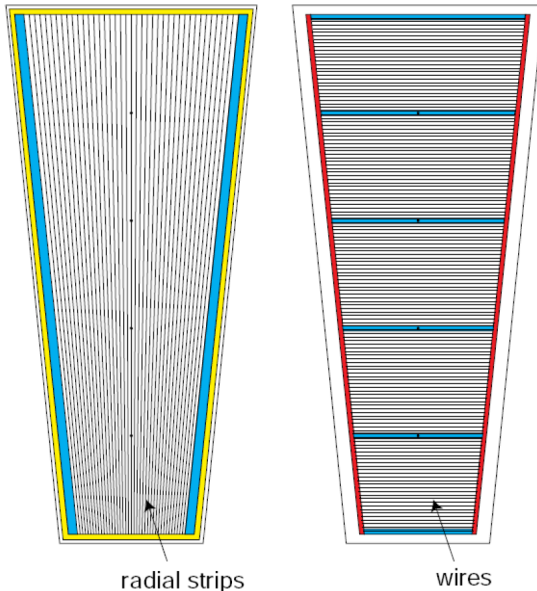


Figure 2.13.: Schematic representation of CSC cathode (left) and anode (right) panels.

515
 516 RPCs are used both in barrel and endcaps, complementing DT and CSC systems, in
 517 order to ensure robustness and redundancy to the muon spectrometer. RPCs are gaseous
 518 detectors characterized by a coarse spatial resolution, but are able to perform precise time
 519 measurements, comparable with the ones provided by scintillators. These chambers are
 520 made of 4 bakelite planes, with a bulk resistivity of 10^{10} – $10^{11} \Omega\text{cm}$. The 2 mm gap between
 521 the plates is filled with a mixture of C₂H₂F₄ (94.5%) and Isobutane. The central part of the
 522 chamber is equipped with insulated aluminum strips, used to collect the signal generated by
 523 crossing particles. In the barrel the strips are rectangularly segmented and run along the
 524 beam axis, whereas the endcaps are equipped with trapezoidal shaped strips. The detector
 525 operates in avalanche mode, and covers the region $|\eta| < 2.1$.

526 2.3. The CMS trigger system

527 The LHC can provide proton-proton interactions at a crossing frequency of 40 MHz and,
 528 for each bunch crossing, several collisions can occur (approximately 20 at the nominal
 529 instantaneous luminosity). Since it is impossible to store and process the large amount
 530 of data associated with the resulting large number of events, a drastic rate reduction has
 531 to be achieved. In fact the speed at which data can be written to mass storage is limited
 532 and, moreover, the vast majority of events produced is not interesting for physics analyses,
 533 because it involves low transverse momentum interactions (also called *minimum bias events*).
 534 The task of reducing this rate is accomplished by the CMS trigger system, which is the start
 535 of the physics event selection. CMS makes use of a two-stage trigger system, consisting of a
 536 *Level-1* trigger (L1) [19] and a *High Level Trigger* (HLT) [20].

537 Level-1 trigger runs on dedicated processors, and accesses coarse level granularity
 538 information from calorimetry and muon system. A L1 Trigger decision has to be taken for
 539 each bunch crossing within $3.2\ \mu\text{s}$. Its task is to reduce the data flow from 40 MHz to about
 540 100 kHz.

541 The High Level Trigger is responsible for reducing the L1 output rate down to a maximum
 542 rate of the order of 1 kHz. The HLT code runs on a farm of commercial processors and can
 543 access the full granularity information of all the sub-detectors.

544 The main characteristics of the CMS trigger system are described in the following.

545 2.3.1. The Level-1 trigger

546 The L1 trigger is responsible for the identification of electrons, muons, photons, jets and
 547 missing transverse energy. It is required to have a high and carefully understood efficiency.
 548 Its output rate and speed are limited by the readout electronics and by the performances
 549 of the data acquisition (DAQ) system [20]. It consists of three main subsystems:

- 550 • L1 Calorimeter Trigger;
- 551 • L1 Muon Trigger;
- 552 • L1 Global Trigger.

553 The L1 Global Trigger is responsible for combining the output of L1 Calorimeter Trigger
 554 and L1 Muon Trigger and for making the decision to either retain the event or discard it.
 555 The organization of CMS L1 Trigger is schematically summarized in Fig. 2.14.

556 L1 Calorimeter Trigger

557 **Controllare se stato cambiato qualcosa nel Run2**

558 The input for the L1 Calorimeter Trigger are calorimeter towers, which are clusters
 559 of signals collected both from ECAL and HCAL. Towers are calculated by calorimeter
 560 high level readout circuits, called Trigger Primitive Generators. The Regional Calorimeter
 561 Trigger identifies electron, photon, τ and jet candidates together with their transverse energy
 562 and sends the information to the Global Calorimeter Trigger. The Global Calorimeter

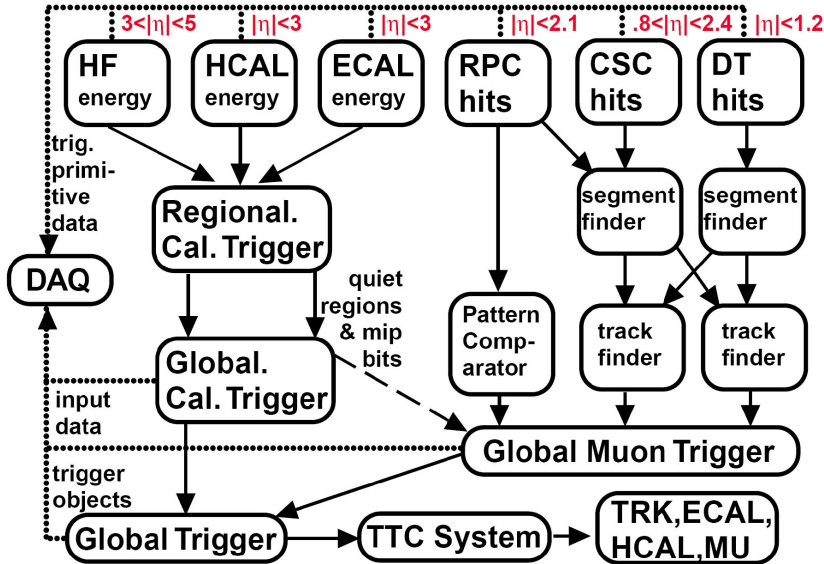


Figure 2.14.: Schematic representation of the Level-1 trigger components.

563 Trigger sorts the candidates according to their transverse energy and sends the first four
 564 objects to the L1 Global Trigger.

565 L1 Muon Trigger

566 Controllare se stato cambiato qualcosa nel Run2

567 The L1 Muon Trigger is actually a composite system itself: information from RPC, CSC
 568 and DT specific triggers are combined in the so called L1 Global Muon Trigger.

569 The RPC trigger electronics builds Track Segments, gives an estimate of their p_T and
 570 sends these segments to the Global Muon Trigger. It also provides the CSC logic unit with
 571 information to solve hit position ambiguities in case of two or more muon tracks crossing
 572 the same CSC chamber.

573 The CSC trigger builds Local Charged Tracks (LCT), that is track segments made out
 574 of the cathode strips only, and assign a p_T value and a quality flag to the LCTs. The best
 575 three LCTs in each sector of nine CSC chambers are passed to the CSC Track Finder, that
 576 uses the full CSC information to build tracks, assigns them a p_T and a quality flag and
 577 sends them to the Global Muon Trigger.

578 DTs are equipped with Track Identifier electronics, which is able to find groups of
 579 aligned hits in the four chambers of a superlayer. Those Track Segments are sent to the
 580 DT Track Correlator that tries to combine segments from two superlayers, measuring the
 581 ϕ angle. The best two segments are sent to the DT Track Finder that builds tracks and
 582 sends them to the Global Muon Trigger.

583 The Global Muon Trigger sorts the RPC, CSC and DT muon tracks and tries to combine
584 them. The final set of muons is sorted according to the quality, and the best four tracks
585 are passed to the L1 Global Trigger.

586 **L1 Global Trigger**

587 **Controllare se stato cambiato qualcosa nel Run2**

588 The L1 Global Trigger is responsible for collecting objects created from the Calorimeter
589 and Muon Triggers and for making a decision whether to retain the event or not. In case
590 the event is accepted, the decision is sent to the Timing Trigger and Control System, that
591 commands the readout of the remaining subsystems.

592 In order to take the decision, the L1 Global Trigger sorts the ranked objects produced
593 by calorimetry and muon system and checks if at least one of the thresholds in the L1
594 trigger table is passed.

595 **2.3.2. The high level trigger (HLT)**

596 The High Level Trigger is designed to reduce the L1 output rate down to about 1000 events/s,
597 which is the amount that will be written to mass storage. HLT code runs on commercial
598 processors and performs reconstruction using the information from all sub-detectors. Events
599 passing the HLT are stored on local disk or in CMS Tier 0⁶.

600 Data read from sub-detectors are assembled by a builder unit and then assigned to
601 a switching network that dispatches events to the processor farm. The CMS switching
602 network has a bandwidth of 1 Tbit/s. This simple design ensures maximum flexibility to
603 the system, the only limitation being the total bandwidth and the number of processors.
604 The system can be easily upgraded adding new processors or replacing the existing ones
605 with faster ones as they become available. Since the algorithms have a fully software
606 implementation, improvements to the algorithms can be easily implemented and do not
607 require any hardware intervention.

608 Event by event, the HLT code is run on a single processor, and the time available to
609 make a decision is about 300 ms. The real time nature of this selection imposes several
610 constraints on the resources an algorithm can use. The reliability of HLT algorithms
611 is of capital importance, because events not selected by the HLT are lost. In order to
612 efficiently process events, the HLT code has to be able to quickly reject not interesting
613 events; computationally expensive algorithms must be run only on good candidates for
614 interesting events. In order to cope with this requirement the HLT code is organized in a
615 virtually layered structure:

⁶The Worldwide LHC Computing Grid (WLCG) is composed of four levels, or “Tiers”, identified with numbers 0, 1, 2 and 3. Each Tier is made up of several computer centres and provides a specific set of services; they process, store and analyse all the data from the Large Hadron Collider (LHC). Tier 0 is the CERN Data Centre. All of the data from the LHC pass through this central hub. Tier 0 distributes the raw data and the reconstructed output to Tier 1’s, and reprocesses data when the LHC is not running.

- Level 2: uses only complete muon and calorimetry information;
- Level 2.5: uses also the pixel information;
- Level 3: makes use of the full information from all the tracking detectors.

Each step reduces the number of events to be processed in the following step. The most computationally expensive tasks are executed in the Level 3; time consuming algorithms such as track reconstruction are only executed in the region of interest. Besides, since the ultimate precision is not required at a HLT level, track reconstruction is performed on a limited set of hits, and is stopped once the required resolution is achieved.

2.4. Event reconstruction and particle identification

In CMS, the physics object reconstruction and identification is based on standard algorithms developed by the collaboration and used by all the physics analyses. In this section, the techniques used for the reconstruction and identification of the physics objects of interest for $H \rightarrow WW \rightarrow 2\ell 2\nu$ analyses are described.

2.4.1. The Particle Flow technique

The Particle Flow (PF) event reconstruction technique [21] aims at the reconstruction and identification of all the stable particles in the event, i.e. electrons, muons, photons, charged and neutral hadrons, with a thorough combination of the information from all CMS sub-detectors, in order to determine their energy, direction and type. These individual particles are then used, for example, to build jets, to measure the missing transverse energy E_T^{miss} , to reconstruct the τ from their decay products, to quantify the charged lepton isolation and to tag b-jets.

The CMS detector is well suited for this purpose. Indeed, the presence of a large internal silicon tracker immersed in an intense solenoidal magnetic field allows the reconstruction of charged particles with high efficiency and small fake rate, and provides a high precision measurement of the particle p_T down to about 150 MeV, for $|\eta| \leq 2.6$. The high granularity of the ECAL calorimeter is the additional key element for the feasibility of the PF technique, allowing the reconstruction of photons and electrons with high energy resolution.

The first step of the PF technique consists in the reconstruction of the basic elements from the various sub-detectors, such as charged-particle tracks, calorimeter clusters and muon tracks. These elements, which are provided by the sub-detectors with high efficiency and low fake rate, are then connected together with a link algorithm.

The good performance of the tracking system are achieved by means of an iterative tracking strategy [22], based on the Kalman Filter algorithm [23]. The basic idea of iterative tracking is that initial iterations search for tracks that are easiest to find, e.g. high p_T tracks produced near the interaction region. After each iteration, hits associated to reconstructed tracks are removed from the hit collection, thereby reducing the combinatorial complexity and simplifying the subsequent iterations, which aim at finding more complicated set of

653 tracks, e.g. low p_T or displaced tracks. The *Iteration 0*, where the majority of tracks are
 654 reconstructed, is designed to identify prompt tracks with $p_T > 0.8$ GeV that have three
 655 hits in the three layers of the pixel detector. *Iteration 1* is used to recover prompt tracks
 656 that have only two pixel hits. *Iteration 2* aims at finding low- p_T prompt tracks while
 657 *Iterations 3–5* are intended to find tracks that originate outside the collision point, i.e.
 658 tracks produced by a secondary vertex, and to recover undetected tracks in the previous
 659 iterations. Each iteration proceeds according to four steps:

- 660 • *seeding*: initial track candidates are obtained using 2 or 3 hits in the innermost layers
 661 (these proto-tracks are called seeds);
- 662 • *pattern recognition*: this step is based on Kalman Filter and searches for hits in the
 663 outer layers that could be associated to the initial track candidate, reconstructing the
 664 particle trajectory;
- 665 • *track fitting*: in this step a fit of the trajectory is performed, using its associated hits
 666 and providing an estimate of the track parameters (p_T , η , ϕ , charge, etc.);
- 667 • *selection*: finally tracks are selected based on quality requirements.

668 The high detection efficiency of the calorimeters is based on a specific calorimeter
 669 clustering algorithm, which is performed separately in each sub-detector. The algorithm is
 670 based on three steps: in the first step, “cluster seeds” are identified as local calorimeter cells
 671 with an energy deposit above a given threshold. Then, “topological clusters” are grown
 672 from the seeds by gathering cells with at least one side in common with a cell already in the
 673 cluster, and with an energy above a given threshold. A topological cluster usually gives rise
 674 to many “particle flow clusters” as seeds, which are identified sharing the energy of each
 675 cell among the particle flow clusters, thereby allowing the determination of the particle flow
 676 cluster energy and position.

677 These elements are then connected to each other using a link algorithm, which identifies
 678 blocks of elements that are topologically compatible. For example, a charged-particle track
 679 is linked to a calorimeter particle flow cluster if the extrapolated position from the track to
 680 the calorimeter is compatible with the cluster boundaries. From these blocks, PF candidates
 681 are identified according to the following order:

- 682 • Muons: a *global muon* gives rise to a *PF muon* if its combined p_T measurement is
 683 compatible within 3 standard deviation with the one provided by the sole tracker. The
 684 corresponding track is removed from the block;
- 685 • Electrons: electrons tend to give rise to short tracks, and to lose energy by Bremsstrahlung
 686 in the tracker layers on their way to the calorimeter. The link between a charged-
 687 particle track (refitted with the Gaussian-Sum Filter [**Adam:815410**]) and one or
 688 more ECAL clusters identifies a *PF electron*. After the identification, the corresponding
 689 tracks and clusters are removed from the block.
- 690 • Charged hadrons: the remaining tracks give rise to *PF charged hadrons*. Tracks can be
 691 linked to ECAL and HCAL clusters, and the energy is determined taking into account
 692 information from calorimeters;

- 693 • Photons and neutral hadrons: ECAL clusters not linked with tracks give rise to *PF*
 694 *photons*, while the remaining HCAL clusters are identified as *PF neutral hadrons*.

695 After the identification of all PF candidates in the event, *PF jets* are clustered as described
 696 in Sec. 2.4.3. The last step is the reconstruction of the *PF* \vec{p}_T^{miss} , which is given by:

$$\vec{p}_T^{\text{miss}} = - \sum_{\text{PF obj}} \vec{p}_T^{\text{PF obj}} , \quad (2.9)$$

697 where the sum extends over all the PF objects. The E_T^{miss} is defined as the modulus of
 698 \vec{p}_T^{miss} .

699 2.4.2. Leptons reconstruction and identification

700 Muons

701 Muons produced at the collision point can go through the entire detector with a negligible
 702 energy loss, thus reaching the detector outermost part where the muon chambers are installed
 703 (see ??). Muons interact through ionization with the layers of the silicon tracker, which is
 704 able to reconstruct their tracks (*tracker track*). The muon tracks are also reconstructed
 705 using the muon system (*standalone muon track*). Based on these objects, two reconstruction
 706 approaches are used: in the first method (outside-in), for each standalone muon tracks
 707 a tracker track is searched for by extrapolating the two tracks to a common surface. If
 708 a match is found, the hits associated to the two tracks are fitted together giving rise
 709 to a *Global Muon*. The second approach (inside-out) consists in considering all tracker
 710 tracks with $p_T > 0.5$ GeV as potential muon candidates and are extrapolated to the muon
 711 system taking into account the magnetic field, the expected energy losses and the multiple
 712 scattering in the detector material. If at least one muon segment (a short track stub made
 713 of DT or CSC hits) matches the extrapolated tracks, the corresponding tracker track is
 714 identified as a *Tracker Muon*.

715 The matching with the muon system improves significantly the muon p_T resolution that
 716 can be obtained from the tracker only, especially in the region with $p_T > 200$ GeV, as shown
 717 in Fig. ??.

718 Electrons

719 2.4.3. Jets reconstruction and identification

720 Jet b tagging

721 2.5. The CMS framework

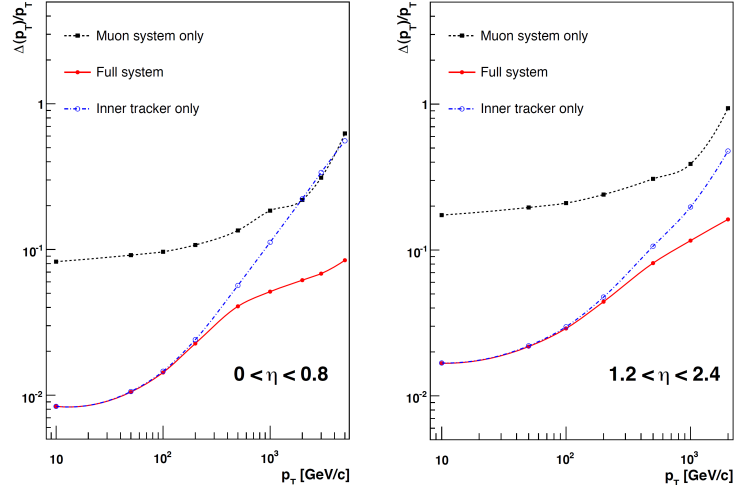


Figure 2.15.: Muon p_T resolution as a function of the muon p_T in the barrel (left) and in the endcap (right) regions. The resolution is provided for the measurement using the tracking system or the muon system only, as well as for the combination of the two methods.

Chapter 3.

⁷²² Higgs boson properties in the ⁷²³ $H \rightarrow WW$ decay channel

⁷²⁴ 3.1. Higgs boson phenomenology at LHC

⁷²⁵ The discovery of a new boson consistent with the standard model (SM) Higgs boson has
⁷²⁶ been reported by ATLAS and CMS Collaborations in 2012. The discovery has been followed
⁷²⁷ by a comprehensive set of studies of properties of this new boson in several production and
⁷²⁸ decay channels and no evidence of deviation from the SM expectation has been found so
⁷²⁹ far.

⁷³⁰ 3.1.1. Higgs boson production mechanisms

⁷³¹ 3.1.2. Higgs boson decay channels

⁷³² 3.2. The $H \rightarrow WW$ decay channel

⁷³³ The CMS studies in the $H \rightarrow WW \rightarrow 2\ell 2\nu$ decay channel include the measurement of the
⁷³⁴ Higgs properties, as well as constraints on the Higgs total decay width and gauge bosons
⁷³⁵ anomalous couplings.

⁷³⁶ 3.2.1. The $H \rightarrow WW \rightarrow 2\ell 2\nu$ signature

⁷³⁷ 3.2.2. Physics objects definition

⁷³⁸ 3.2.3. Background processes

⁷³⁹ 3.3. Experimental results of the Higgs boson ⁷⁴⁰ measurements

Chapter 4.

Measurement of the Higgs boson transverse momentum at 8 TeV using $H \rightarrow WW \rightarrow 2\ell 2\nu$ decays

4.1. Introduction

The Higgs boson production at hadron colliders is characterized by p_T^H and η . The η distribution is essentially driven by the PDF of the partons in the colliding hadrons, and it is only mildly sensitive to radiative corrections. The p_T^H distribution is instead sensitive to QCD radiative corrections. Considering the ggH production mode, at LO in perturbation theory, $\mathcal{O}(\alpha_s^2)$, the Higgs boson is always produced with p_T^H equal to zero. Indeed in order to have p_T different from zero, the Higgs boson has to recoil at least against one parton. Higher order corrections to the ggH process are numerically large and are known at NLO including full top quark mass dependence [24, 25], and at NNLO using the so-called large- m_t approximation [26–28], in which the top quark mass is assumed to be very large and the fermionic loop is replaced by an effective vertex of interaction. Starting from the NLO, the Higgs boson can be produced recoiling against other final state partons, resulting in a finite p_T^H . For this reason the LO process for Higgs production at $p_T \neq 0$ is at $\mathcal{O}(\alpha_s^3)$, and the counting of perturbative orders differs between inclusive Higgs boson production and p_T^H distribution. Also, NNLO QCD corrections in the p_T^H observable have recently been shown [29].

When $p_T^H \sim m_H$ the QCD radiative corrections to p_T^H differential cross section are theoretically evaluated using fixed-order calculations. When $p_T^H \ll m_H$ the perturbative expansion does not converge due to the presence of large logarithmic terms of the form $\alpha_s^n \ln^{2n} m_H^2/p_T^2$, leading to a divergence of $d\sigma/dp_T$ in the limit of $p_T \rightarrow 0$. For computing the p_T^H spectrum in this region soft-gluon resummation techniques are used, and matched to the fixed-order calculation in the $p_T^H \sim m_H$ region. For the p_T^H differential cross section the large- m_t calculation is a crude approximation, since it is known that the top quark mass has a non-negligible effect on the shape of the spectrum. Moreover the inclusion of the bottom quark contribution in the fermionic loop can significantly modify the p_T^H shape [30], as shown in Fig. 4.1. Hence, a precise experimental measurement of the p_T^H spectrum is important to test the existing SM calculations.

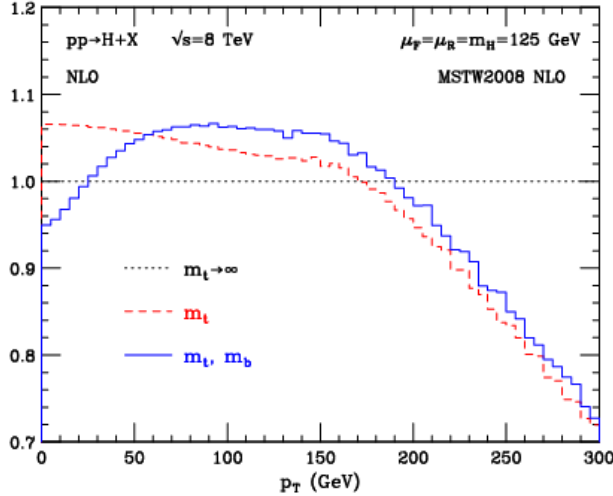


Figure 4.1.: p_T^H distribution computed at NLO (α_s^3) and normalized to the calculation obtained in the large- m_t approximation. The red dashed line corresponds to the calculation including the top quark mass while the blue line refers to the calculation including also the bottom quark effects.

Possible extensions of the SM predict a modification of the Higgs boson couplings to gluons and to the top quark. Many of these models actually predict the existence of new states that interact with the SM Higgs boson, but are beyond the direct production reach at the actual LHC energies. The effect of these new states could however show up as a deviation of the Higgs boson couplings with respect to the SM expectation. The modification of the couplings, as shown in Refs. [31, 32], can change the kinematics of the Higgs boson production and the effect can be particularly sizeable in the tail of the p_T^H distribution. Other models, such as Composite Higgs [33], predict the existence of top-partners, which are heavy resonances with the same quantum numbers as the top quark, that can interact with the Higgs boson in the ggH fermionic loop, changing the p_T^H shape with respect to what the SM predicts [34]. The measurement of the p_T^H spectrum is thus a useful tool for indirect searches of new particles predicted by theories beyond the SM.

Measurements of the fiducial cross sections and of several differential distributions, using the $\sqrt{s} = 8$ TeV LHC data, have been reported by ATLAS [35–37] and CMS [38, 39] for the $H \rightarrow ZZ \rightarrow 4\ell$ ($\ell = e, \mu$) and $H \rightarrow \gamma\gamma$ decay channels. In this chapter a measurement of the fiducial cross section times branching fraction ($\sigma \times \mathcal{B}$) and p_T spectrum for Higgs boson production in $H \rightarrow WW \rightarrow e^\pm \mu^\mp \nu\nu$ decays, based on $\sqrt{s} = 8$ TeV LHC data, is reported.

The analysis is performed looking at different flavour leptons in the final state in order to suppress the sizeable contribution of backgrounds containing a same-flavour lepton pair originating from Z boson decay.

Although the $H \rightarrow WW \rightarrow 2\ell 2\nu$ channel has lower resolution in the p_T^H measurement compared to the $H \rightarrow \gamma\gamma$ and $H \rightarrow ZZ \rightarrow 4\ell$ channels because of neutrinos in the final state, the channel has a significantly larger $\sigma \times \mathcal{B}$, exceeding those for $H \rightarrow \gamma\gamma$ by a factor of 10 and $H \rightarrow ZZ \rightarrow 4\ell$ by a factor of 85 for a Higgs boson mass of 125 GeV [40], and is

characterized by good signal sensitivity. Such sensitivity allowed the observation of a Higgs boson at the level of 4.3 (5.8 expected) standard deviations for a mass hypothesis of 125.6 GeV using the full LHC data set at 7 and 8 TeV [41].

The measurement is performed in a fiducial phase space defined by kinematic requirements on the leptons that closely match the experimental event selection.

The effect of the limited detector resolution, as well as the selection efficiency with respect to the fiducial phase space are corrected to particle level with an unfolding procedure [42], as explained in Sec. 4.7.

4.2. Data sets, triggers and MC samples

This analysis relies on the published $H \rightarrow WW$ measurements [41] in terms of code, selections and background estimates for both the ggH and VBF production mechanisms.

4.2.1. Data sets and triggers

The data sets used for the analysis correspond to 19.4 fb^{-1} at $\sqrt{s} = 8 \text{ TeV}$ of integrated luminosity composed of the following CMS data taking periods during 2012: 2012A (892 pb^{-1}), 2012B (4440 pb^{-1}), and 2012C (6898 pb^{-1}) and 2012D (7238 pb^{-1}). Data have been checked and validated and only data corresponding to good data taking quality are considered. The $e^\pm \mu^\mp$ final state is considered in this analysis.

For the data samples, the events are required to fire one of the unprescaled single-electron, single-muon or muon-electron triggers. Due to the rather high LHC instantaneous luminosity the single-lepton triggers must have high HLT p_T thresholds, otherwise the rate of these triggers would be too large to be sustained. The double-lepton triggers allow to lower down the p_T thresholds while keeping a sustainable trigger rate, thus maintaining a good sensitivity to the Higgs boson signal, for which the lepton p_T can be rather small. A brief overview of the HLT p_T criteria on the leptons is given in Table 4.1. While the HLT lepton p_T thresholds of 17 and 8 GeV for the double lepton triggers accommodate the offline lepton p_T selection of 20 and 10 GeV, the higher p_T thresholds in the single lepton triggers help partially recovering double lepton trigger inefficiencies as a high p_T lepton is on average expected due to the kinematics of the Higgs decay.

The trigger is not simulated in MC samples but the combined trigger efficiency is estimated from data and applied as a weight to all simulated events. The trigger efficiency for single and double lepton triggers is calculated using a Tag and Probe technique separately for muons and electrons, in bins of η and p_T . The Tag and Probe method uses a known mass resonance (e.g. J/Ψ , Z) to select particles of the desired type, and probe the efficiency of a particular selection criterion on these particles. In general the “tag” is an object that passes a set of very tight selection criteria designed to isolate the required particle type. Tags are often referred to as golden electrons or muons and the fake rate for passing tag selection criteria should be very small. A generic set of the desired particle type (i.e.

Table 4.1.: Highest transverse momentum thresholds applied in the lepton triggers at the HLT level. Double set of thresholds indicates the thresholds for each leg of the double lepton triggers.

Trigger Path	8 TeV
Single-Electron	$p_T > 27$ GeV
Single-Muon	$p_T > 24$ GeV
Muon-Electron	$p_T > 17$ and 8 GeV
Electron-Muon	$p_T > 17$ and 8 GeV

with potentially very loose selection criteria) known as “probes” is selected by pairing these objects with tags such that the invariant mass of the combination is consistent with the mass of the resonance. Combinatorial backgrounds may be eliminated through any of a variety of background subtraction methods such as fitting, or sideband subtraction. The definition of the probe objects depend on the specifics of the selection criterion being examined. The simple expression to get the efficiency ϵ as a function of p_T and η is given below:

$$\epsilon(p_T, \eta) = \frac{N_{\text{pass}}^{\text{probe}}}{N_{\text{pass}}^{\text{probe}} + N_{\text{fail}}^{\text{probe}}} \quad (4.1)$$

For double lepton triggers the efficiency is calculated separately for each leg of the trigger and then combined together. In the calculation the efficiencies of the two trigger legs are considered as independent, given that the correlations are very small. The combined efficiency is then used as a kinematics-dependent weight to be applied on top of simulated events.

The event efficiency ϵ_{ev} for an event with two leptons to pass the single lepton trigger is given by the following formula:

$$\epsilon_{\text{ev}} = 1 - (1 - \epsilon_{S,\ell 1}) \cdot (1 - \epsilon_{S,\ell 2}) \quad , \quad (4.2)$$

where $\epsilon_{S,\ell 1}$ and $\epsilon_{S,\ell 2}$ are the efficiencies for the leading and subleading lepton to pass the single lepton trigger. In other words, the dilepton event passes the single lepton trigger if either one of the two leptons passes the single lepton trigger, excluding the cases for which both leptons pass the trigger. For double lepton triggers, the event efficiency can be written as:

$$\epsilon_{\text{ev}} = \epsilon_{D,\ell 1}^{\text{lead}} \cdot \epsilon_{D,\ell 2}^{\text{trail}} + (1 - \epsilon_{D,\ell 1}^{\text{lead}} \cdot \epsilon_{D,\ell 2}^{\text{trail}}) \cdot \epsilon_{D,\ell 1}^{\text{trail}} \cdot \epsilon_{D,\ell 2}^{\text{lead}} \quad , \quad (4.3)$$

where $\epsilon_{D,\ell 1}^{\text{lead(trail)}}$ is the efficiency of the first lepton to pass the leading (trailing) leg of the double lepton trigger, and $\epsilon_{D,\ell 2}^{\text{lead(trail)}}$ is the efficiency of the second lepton to pass the leading (trailing) leg of the double lepton trigger. The final event efficiency applied to reweight the events in simulation is given by the boolean OR of the event efficiencies corresponding to the single and double lepton triggers, which, using Eqs. (4.2) and (4.3), can be written as:

$$\begin{aligned}\epsilon_{\text{ev}} = & 1 - (1 - \epsilon_{S,\ell 1}) \cdot (1 - \epsilon_{S,\ell 2}) + \\ & + (1 - \epsilon_{S,\ell 1}) \cdot (1 - \epsilon_{S,\ell 2}) \cdot \\ & \cdot [\epsilon_{D,\ell 1}^{\text{lead}} \cdot \epsilon_{D,\ell 2}^{\text{trail}} + (1 - \epsilon_{D,\ell 1}^{\text{lead}} \cdot \epsilon_{D,\ell 2}^{\text{trail}}) \cdot \epsilon_{D,\ell 1}^{\text{trail}} \cdot \epsilon_{D,\ell 2}^{\text{lead}}] .\end{aligned}\quad (4.4)$$

The term that multiplies the double lepton trigger event efficiency is needed to ensure that the events passing the double lepton trigger do not pass also the single lepton trigger.

4.2.2. Monte Carlo samples

Several Monte Carlo event generators are used to simulate the signal and background processes:

- The first version of the POWHEG program [43–47] (POWHEG V1) provides event samples for the $H \rightarrow WW$ signal for the gluon fusion (ggH) and VBF production mechanisms, as well as $t\bar{t}$ and tW processes [48], with NLO accuracy.
- The $qq \rightarrow W^+W^-$, Drell-Yan, ZZ, WZ, $W\gamma$, $W\gamma^*$, tri-bosons and $W+jets$ processes are generated using the MADGRAPH 5.1.3 [49] event generator.
- The $gg \rightarrow W^+W^-$ process is generated using the GG2WW 3.1 generator [50] and its cross section is scaled to the approximate NLO prediction [51, 52].
- The VH process is simulated using PYTHIA 6.426 [53].

For leading-order generators samples, the CTEQ6L [54] set of parton distribution functions (PDF) is used, while CT10 [55] is used for next-to-leading order (NLO) ones. Cross section calculations [56] at next-to-next-to-leading order (NNLO) are used for the $H \rightarrow WW$ process, while NLO calculations are used for background cross sections. The $H \rightarrow WW$ process simulation is reweighted so that the p_T^H spectrum and inclusive production cross section closely match the SM calculations that have NNLO+NNLL pQCD accuracy in the description of the Higgs boson inclusive production, in accordance with the LHC Higgs Cross Section Working Group recommendations [40]. The reweighting of the p_T^H spectrum is achieved by tuning the POWHEG generator, as described in detail in Ref. [57]. Cross sections computed with NLO pQCD accuracy [40] are used for the background processes. The contribution of the $t\bar{t}H$ production mechanisms is checked to be negligible in each bin of p_T^H (below 1%) and is not included among the different production mechanisms. In Fig. 4.2 the relative fraction of the four production mechanisms is shown for each p_T^H bin.

For all processes, the detector response is simulated using a detailed description of the CMS detector, based on the GEANT4 package [58].

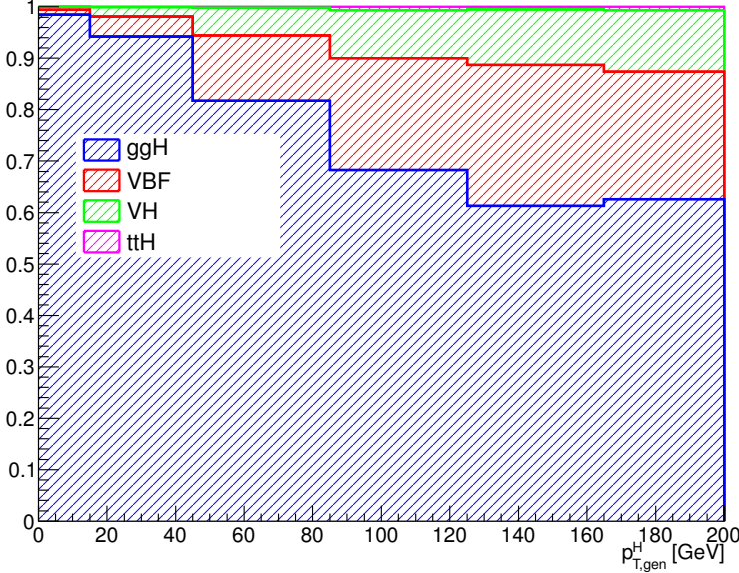


Figure 4.2.: Relative fraction of ggH, VBF, VH and ttH in each bin of the Higgs boson transverse momentum.

884 Minimum bias events are superimposed on the simulated events to emulate the additional
 885 pp interactions per bunch crossing (pileup). The number of pile-up events simulated in the
 886 MC samples (in the same bunch crossing, in time, or in the previous or following one, out
 887 of time pileup) have been generated poissonianly sampling from a distribution similar to
 888 what is expected from data. For a given range of analyzed runs, the mean number of pileup
 889 interactions per bunch crossing is estimated per luminosity block using the instantaneous
 890 luminosity provided by the LHC, integrated over the entire run range and normalized. The
 891 average number of pileup events per beam crossing in the 2011 data is about 10, and in the
 892 2012 data it is about 20.

893 The simulated events are reweighted to correct for observed differences between data
 894 and simulation in the number of pileup events, as shown in Fig. 4.3, trigger efficiency, and
 895 lepton reconstruction and identification efficiencies [41].

896 For the comparison of the measured unfolded spectrum with the theoretical predictions,
 897 two additional MC generators are used for simulating the SM Higgs boson production in
 898 the ggH process: HRES 2.3 [30, 59] and the second version of the POWHEG generator
 899 (POWHEG V2) [60]. HRES is a partonic level MC generator that computes the SM Higgs
 900 boson cross section at NNLO accuracy in pQCD and performs the NNLL resummation
 901 of soft-gluon effects at small p_T . The central predictions of HRES are obtained including
 902 the exact top and bottom quark mass contribution to the gluon fusion loop, fixing the
 903 renormalization and factorization scale central values at a Higgs boson mass of 125 GeV.
 904 The cross section normalization is scaled, to take into account electroweak corrections, by a
 905 factor of 1.05 and the effects of threshold resummation by a factor of 1.06 [61, 62]. The

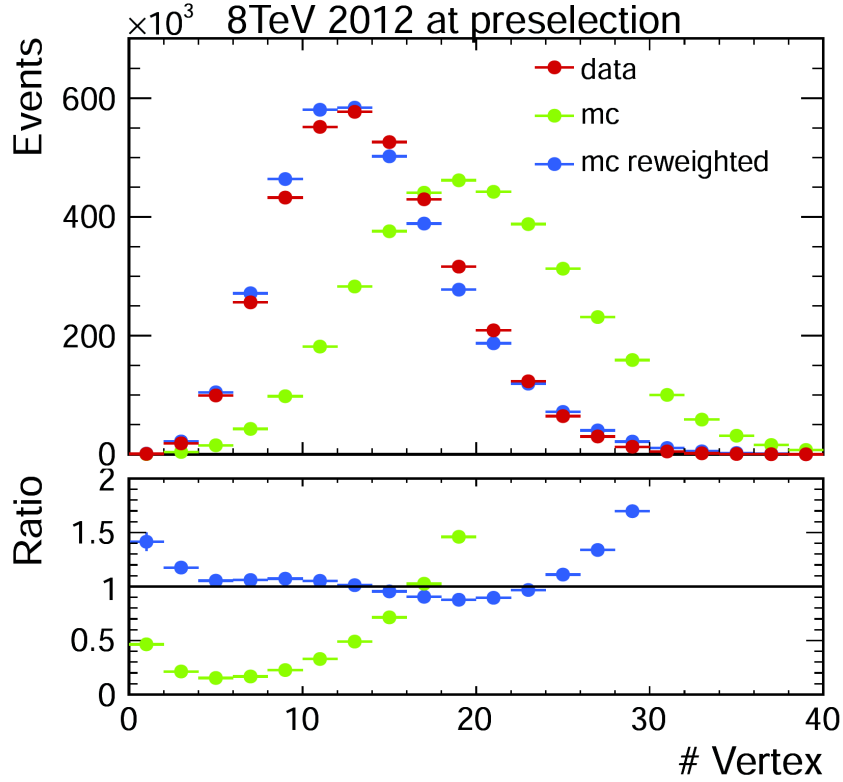


Figure 4.3.: Distribution of the number of vertices in data and in simulation, before and after applying the pile-up reweighting.

906 upper and lower bounds of the uncertainties are obtained by scaling up and down both the
 907 renormalization and the factorization scales by a factor of two. The POWHEG V2 generator
 908 is a matrix element based generator that provides a NLO description of the ggH process
 909 in association with zero jets, taking into account the finite mass of the bottom and top
 910 quarks. The POWHEG prediction is tuned using the POWHEG damping factor *hdump* of
 911 104.17 GeV, in order to match the p_T^H spectrum predicted by HRES in the full phase space.
 912 This factor reduces the emission of additional jets in the high p_T regime, and enhances the
 913 contribution from the Sudakov form factor in the limit of low p_T . The POWHEG generator
 914 is interfaced to the JHUGEN generator version 5.2.5 [63–65] for the decay of the Higgs
 915 boson to a W boson pair and interfaced with PYTHIA 8 [66] for the simulation of parton
 916 shower and hadronization effects.

917 4.3. Analysis Strategy

918 The analysis presented here is based on that used in the previously published $H \rightarrow WW \rightarrow 2\ell 2\nu$
 919 measurements by CMS [41], modified to be inclusive in the number of jets. This modifica-

tion significantly reduces the uncertainties related to the modelling of the number of jets produced in association with the Higgs boson.

4.3.1. Event reconstruction and selections

The electron selection is based on two multivariate discriminants, one specialised in identifying the electron object and the other for isolation. The cut value for each discriminant is optimised to provide a good fake electron rejection and to improve the signal acceptance.

Muons are reconstructed using the standard CMS selection and are required to be identified both in the tracker (*Tracker Muon*) and in the muon chambers (*Global Muon*). Additionally quality criteria on the muon track are required, such as to have at least 10 hits in the tracker (at least one of which in the pixel detector) and to have $\chi^2/ndf < 10$. Muon isolation is based on the Particle-Flow algorithm. An MVA approach is considered, based on the radial distributions of the Particle-Flow candidates inside a cone of radius 0.5 around the muon direction.

The efficiencies for the identification and isolation of the electrons and muons are measured in data and in simulation selecting a pure sample of leptons coming from the $Z \rightarrow \ell\ell$ decay, and using a Tag and Probe technique very similar to the one described in Sec. 4.2.1 for the trigger efficiency. In this case, the probe lepton is defined by loose isolation and identification requirements and the efficiency to pass the tight analysis selections is measured performing a simultaneous fit of signal plus background in two categories, corresponding to events in which the probe lepton pass or fail the analysis requirements. For the electrons, the resonant signal contribution in the fit is modelled as the convolution of a Breit-Wigner and a Crystal-Ball function. A polynomial function is added to take into account the tail in the low mass region. For muons the signal is fitted using the sum of two Voigtian functions. For both electrons and muons the background contribution is modelled as a third order Bernstein polynomial function. The efficiencies for data and simulation are extracted as parameters of the fit and are used as scale factors to correct the MC simulation to precisely model the data.

This part would probably end up in the Object Reconstruction chapter

Jets in this analysis are reconstructed by combining the energy measured in the calorimeters and tracks from charged particles on basis of the standard CMS particle flow algorithm and using the anti- k_T clustering algorithm with $R = 0.5$. Events will be classified into zero jet, one jet and VBF topologies by counting jets within $|\eta| < 4.7$ and for $p_T > 30$ GeV.

In addition to the standard CMS PF E_T^{miss} , in this analysis a *projected* E_T^{miss} variable is also used. The *projected* E_T^{miss} is defined as the component of \vec{p}_T^{miss} transverse to the nearest lepton if the lepton is situated within the azimuthal angular window of $\pm\pi/2$ from the \vec{p}_T^{miss} direction, or the E_T^{miss} itself otherwise. Since the E_T^{miss} resolution is degraded by pileup, the minimum of two projected E_T^{miss} variables is used: one constructed from all identified particles (full projected E_T^{miss}), and another constructed from the charged particles only (track projected E_T^{miss}).

Background events from $t\bar{t}$ and tW production are rejected applying a soft-muon veto and b-tagging veto. The former selection requires that in the event there are no muons from b-decays passing the following cuts:

- the muon is reconstructed as TrackerMuon;
- the number of hits of the muon in the Silicon Tracker is greater than 10;
- the transverse impact parameter of the muon is less than 0.2 cm;
- if $p_T > 20 \text{ GeV}$ then the muon is required to be non-isolated with $ISO/p_T > 0.1$.

The latter veto rejects events that contain jets tagged as b-jets using two different algorithms for high and low p_T jets. For jets with p_T between 10 and 30 GeV, the Track-Counting-High-Efficiency (TCHE) algorithm, with a cut at 2.1 on the discriminating variable, is applied. For jets above 30 GeV, a better performing algorithm, Jet-Probability (JP), is used. Jets are identified as b-jets by the JP algorithm if the discriminating variable has a value above 1.4. In the following a b-tagged jet is defined as a jet, within $|\eta| < 2.4$ (b-tagging requires the tracker information), with a value of the discriminating variable above the mentioned thresholds for the two algorithms.

The event selection consists of several steps. The first step is to select WW-like events applying a selection that consists of the following set of cuts:

1. Lepton preselection:

- at least two opposite-charge and opposite-flavour ($e\mu$) isolated leptons reconstructed in the event;
- $|\eta| < 2.5$ for electrons and $|\eta| < 2.4$ for muons;
- $p_T > 20 \text{ GeV}$ for the leading lepton. For the trailing lepton, the transverse momentum is required to be larger than 10 GeV.

2. Extra lepton veto:

the event is required to have two and only two opposite-sign leptons passing the lepton selection.

3. E_T^{miss} preselection:

particle flow E_T^{miss} is required to be greater than 20 GeV.

4. projected E_T^{miss} selection:

minimum projected E_T^{miss} required to be larger than 20 GeV.

5. Di-lepton mass cut:

$m_{\ell\ell} > 12 \text{ GeV}$ in order to reject low mass resonances and QCD backgrounds.

6. Di-lepton p_T cut:

$p_T^{\ell\ell} > 30 \text{ GeV}$.

7. Transverse mass:

$m_T > 60 \text{ GeV}$ to reject Drell-Yan to $\tau\tau$ events.

In addition to the WW-like preselection other cuts are applied in order to reduce the top quark background (both $t\bar{t}$ and tW), which is one of the main backgrounds in this final state. Two different selections are used depending on the number of jets with $p_T > 30 \text{ GeV}$ in the event. This is done to suppress the top quark background both in the low p_T^H region, where 0-jets events have the largest contribution, and for higher p_T^H values where also larger jet multiplicity events are important. The selection for 0-jets events relies on the

soft-muon veto and on a soft jets (with $p_T < 30$ GeV) anti b-tagging requirement. The latter requirement exploits the TCHE algorithm to reject soft jets that are likely to come from b quarks hadronization.

For events with a jet multiplicity greater or equal than one, a different selection is applied. In this case we exploit the good b-tagging performances of the JP tagger to reject all the jets with $p_T > 30$ GeV that are likely to come from a b quark hadronization. The analysis selection requires to have no events containing b-tagged jets with $p_T > 30$ GeV.

A cut-flow plot is reported in Fig. 4.4, showing the effect of each selection using signal and background simulations. In the first bin, labelled as “No cut”, no selection is applied and the bin content corresponds to the total expected number of events with a luminosity of 19.4 fb^{-1} . All the events in this bin have at least two leptons with a loose transverse momentum cut of 8 GeV. In the following bin the lepton cuts are applied, including the requirement to have two opposite-sign and opposite-flavour leptons and the extra lepton veto. Then all the other selections are progressively reported, showing the effect of each cut on the background and signal yields. For each selection the expected signal over background ratio is also shown, which, after the full selection requirements, reach a maximum value of about 3%.

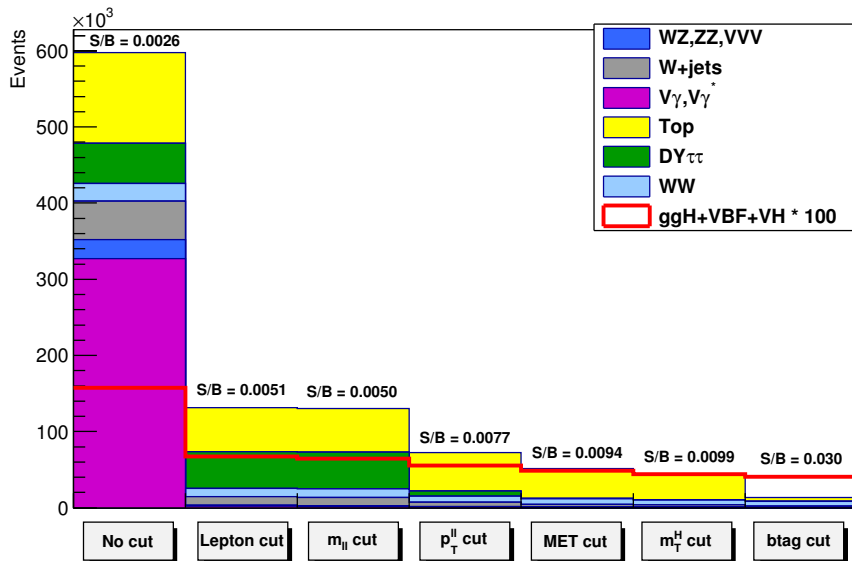


Figure 4.4.: Effect of single selections on MC samples. The signal (red line) is multiplied by 100 and superimposed on stacked backgrounds. In each bin, corresponding to a different selection, is reported the expected number of events in MC at a luminosity of 19.46 fb^{-1} .

1014 **4.3.2. Fiducial phase space**

1015 The Higgs boson transverse momentum is measured in a fiducial phase space, whose
1016 requirements are chosen in order to minimize the dependence of the measurements on the
1017 underlying model of the Higgs boson properties and its production mechanism.

1018 The exact requirements are determined by considering the two following correlated
1019 quantities: the reconstruction efficiency for signal events originating from within the fiducial
1020 phase space (fiducial signal efficiency ϵ_{fid}), and the ratio of the number of reconstructed
1021 signal events that are from outside the fiducial phase space (“out-of-fiducial” signal events)
1022 to the number from within the fiducial phase space. The requirement of having a small
1023 fraction of out-of-fiducial signal events, while at the same time preserving a high value of the
1024 fiducial signal efficiency ϵ_{fid} , leads to a loosening of the requirements on the low-resolution
1025 variables, $E_{\text{T}}^{\text{miss}}$ and m_{T} , with respect to the analysis selection.

1026 The fiducial phase space used for the cross section measurements is defined at the
1027 particle level by the requirements given in Table 4.2. The leptons are defined as Born-level
1028 leptons, i.e. before the emission of final-state radiation (FSR), and are required not to
1029 originate from leptonic τ decays. The effect of including FSR is evaluated to be of the
1030 order of 5% in each p_{T}^{H} bin. For the VH signal process, the two leptons are required to
1031 originate from the $H \rightarrow WW \rightarrow 2\ell 2\nu$ decays in order to avoid including leptons coming
1032 from the associated W or Z boson.

Table 4.2.: Summary of requirements used in the definition of the fiducial phase space.

Physics quantity	Requirement
Leading lepton p_{T}	$p_{\text{T}} > 20 \text{ GeV}$
Subleading lepton p_{T}	$p_{\text{T}} > 10 \text{ GeV}$
Pseudorapidity of electrons and muons	$ \eta < 2.5$
Invariant mass of the two charged leptons	$m_{\ell\ell} > 12 \text{ GeV}$
Charged lepton pair p_{T}	$p_{\text{T}}^{\ell\ell} > 30 \text{ GeV}$
Invariant mass of the leptonic system in the transverse plane	$m_{\text{T}}^{\ell\ell\nu\nu} > 50 \text{ GeV}$
$E_{\text{T}}^{\text{miss}}$	$E_{\text{T}}^{\text{miss}} > 0$

1033 A detailed description of the fiducial region definition and its optimization is given in
1034 appendix A.

1035 **4.3.3. Binning of the p_{T}^{H} distribution**

1036 Experimentally, the Higgs boson transverse momentum is reconstructed as the vector sum
1037 of the lepton momenta in the transverse plane and $E_{\text{T}}^{\text{miss}}$.

$$\vec{p}_{\text{T}}^{\text{H}} = \vec{p}_{\text{T}}^{\ell\ell} + \vec{p}_{\text{T}}^{\text{miss}} \quad (4.5)$$

1038 Compared to other differential analysis of the Higgs cross section, such as those in the ZZ
 1039 and $\gamma\gamma$ decay channels, this analysis has to cope with the limited resolution due to the E_T^{miss}
 1040 entering the transverse momentum measurement. The effect of the limited E_T^{miss} resolution
 1041 has two main implications on the analysis strategy. The first one is that the choice of
 1042 the binning in the p_T^H spectrum needs to take into account the detector resolution. The
 1043 second implication is that migrations of events across bins are significant and an unfolding
 1044 procedure needs to be applied to correct for selection efficiencies and bin migration effects.

1045 Given these aspects the criterion that was used to define the p_T^H bin size is devised to
 1046 keep under control the bin migrations due to the finite resolution. For any given bin i we
 1047 can define the purity P_i on a signal sample as the number events that are generated and
 1048 also reconstructed in that bin, $N_i^{\text{GEN|RECO}}$, divided by the number of events reconstructed
 1049 there, N_i^{RECO} :

$$P_i = \frac{N_i^{\text{GEN|RECO}}}{N_i^{\text{RECO}}} \quad . \quad (4.6)$$

1050 The bin width is chosen in such a way as to make the smallest bins able to ensure a purity
 1051 of about 60% on a ggH signal sample. Following this prescription we have divided the whole
 1052 p_T^H range in the following six bins: [0-15 GeV], [15-45 GeV], [45-85 GeV], [85-125 GeV],
 1053 [125-165 GeV], [165- ∞ GeV].

1054 The efficiency of the analysis selection with respect to the fiducial phase space is reported
 1055 in Fig. 4.5 (a) for each p_T^H bin. The efficiency denominator is the number of events that
 1056 are inside the fiducial phase space, while the numerator is the number of events that pass
 1057 both the analysis and the fiducial phase space selections. The fake rate, defined by the
 1058 ratio of signal events that pass the analysis selection but are not within the fiducial phase
 1059 space, divided by the total number of events passing both the analysis and the fiducial
 1060 phase space selections is shown in Fig. 4.5 (b). For both the selection efficiency and the
 1061 fake rate, all the signal production mechanisms are included. The overall efficiency and
 1062 fake rate are $\epsilon = 0.362 \pm 0.005$ and *fake rate* = 0.126 ± 0.004 respectively, where only
 1063 statistical uncertainties are taken into account.

1064 If a 4π acceptance is defined, requiring just that the Higgs decays to WW and then to
 1065 $2\ell 2\nu$, the efficiency becomes $\epsilon = 0.0396 \pm 0.0003$ and the fake rate is zero.

1066 4.4. Background estimation

1067 4.4.1. Top quark background

1068 In this analysis the top quark background is divided into two different categories depending
 1069 on the number of jets in the event. In the two categories different selections are applied,
 1070 especially concerning the b-tagging requirements.

1071 The general strategy for determining the residual top events in the signal region is to
 1072 first measure the top tagging efficiencies from an orthogonal region of phase space in data.

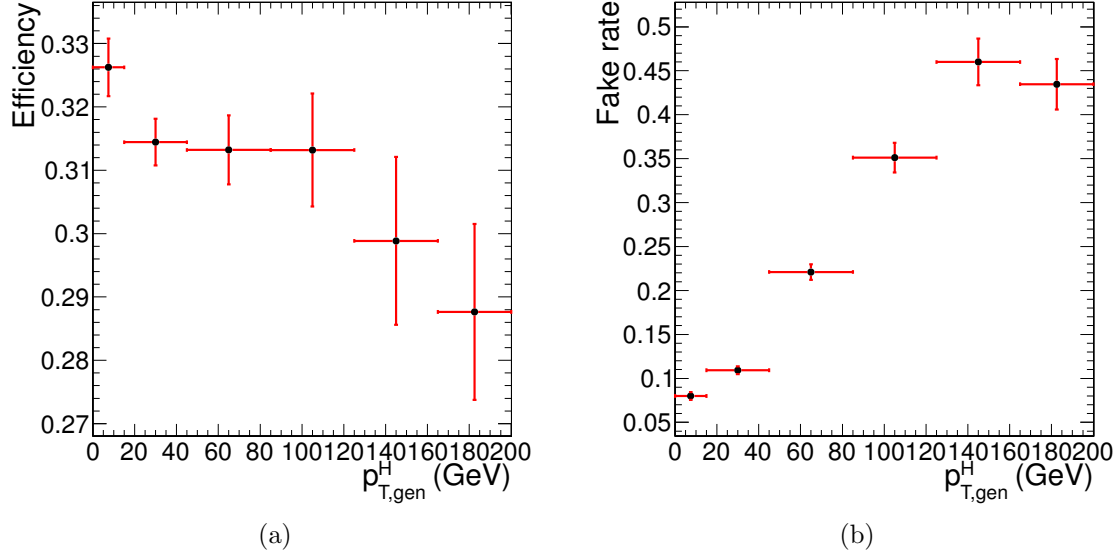


Figure 4.5.: Efficiency of the full selection (a) and fake rate (b) as a function of $p_{T,\text{gen}}^H$.

1073 The orthogonal phase space is defined inverting the b-veto requirement of the signal region,
 1074 in such a way to have a control region enriched in top quark events. Then, using this
 1075 efficiency, the number of events with the associated uncertainty is propagated from the
 1076 control region to the signal region. The number of surviving top events in the signal region
 1077 would then be:

$$N_{\text{bveto}}^{\text{signal}} = N_{\text{btag}}^{\text{control}} \cdot \frac{1 - \epsilon_{\text{top}}}{\epsilon_{\text{top}}} \quad (4.7)$$

1078 where $N_{\text{btag}}^{\text{control}}$ is the number of events in the control region and ϵ_{top} is the efficiency as
 1079 measured in data.

1080 The methods to estimate the top background contribution in the two jet categories are
 1081 different and are explained below.

1082 0-jets category

1083 Most of the top background, composed of $t\bar{t}$ and tW processes, is rejected in the 0-jet bin
 1084 by the jet veto. The top-tagging efficiency in the zero jet bin, $\epsilon_{\text{tag}}^{0\text{-jet}}$, is the probability for a
 1085 top event to fail one of either the b-tagging veto or the soft muon veto, and is defined as:

$$\epsilon_{\text{tag}} = \frac{N_{\text{tag}}^{\text{control}}}{N^{\text{control}}} \quad , \quad (4.8)$$

where N^{control} is the number of events in the top control phase space defined requiring one b-tagged jet with $p_T > 30$ GeV, and $N_{\text{tag}}^{\text{control}}$ is the subset of those events that pass either the soft muon tagging or the low- p_T b jet tagging. The purity of this control sample, as estimated from simulation, is about 97%. The remaining 3% background contribution is estimated from simulation and subtracted from the numerator and denominator of Eq. (4.9). The efficiency $\epsilon_{\text{top}}^{0-jet}$ can then be estimated using the following formula:

$$\epsilon_{\text{top}}^{0-jet} = f_{t\bar{t}} \cdot \epsilon_{2b} + f_{tW} \cdot (x \cdot \epsilon_{2b} + (1 - x) \cdot \epsilon_{\text{tag}}) , \quad (4.9)$$

$$\epsilon_{2b} = 1 - (1 - \epsilon_{\text{tag}})^2 , \quad (4.10)$$

where $f_{t\bar{t}}$ and f_{tW} are the $t\bar{t}$ and tW fractions respectively, x is the fraction of tW events containing 2 b jets, and ϵ_{2b} is the efficiency for a top event with 0 counted jets, i.e. two soft b jets, to pass the top veto. For the ratio of $t\bar{t}$ and tW cross-sections an uncertainty of 17% is assumed. The fraction $f_{t\bar{t}}$ is estimated using MC simulation of the $t\bar{t}$ and tW processes at NLO accuracy.

Using this procedure a data/simulation scale factor of 0.98 ± 0.17 is found, and is applied to correct the MC simulation in order to match the data.

Category with more than 0 jets

The strategy for the estimation of the top background in events with at least one jet with p_T greater than 30 GeV is the following. First of all the efficiency for tagging a b jet is measured both in data and simulation and the values are used to correct the simulation for different b-tagging efficiencies in data and simulation. This evaluation is performed in a control region, called CtrlTP, containing at least two jets, using a Tag&Probe technique. The procedure to extract these scale factors is presented in Sec. 4.4.1. Then a larger statistics control region, CtrlDD, is defined by requiring at least one b-tagged jet and we use the simulation, corrected for the previously computed b-tagging efficiency scale factor, to derive the factor that connects the number of events in CtrlDD to the number of events in the signal region. This second step is explained in detail in Sec. 4.4.1.

Tag&Probe

The Tag&Probe technique is a method to estimate the efficiency of a selection on data. It can be applied whenever one has two objects in one event, by using one of the two, the *tag*, to identify the process of interest, and using the second, the *probe*, to actually measure the efficiency of the selection being studied. In our case we want to measure the b-tagging efficiency, so what we need is a sample with two b-jets per event. The easiest way to construct such a sample is to select $t\bar{t}$ events.

The CrtlTP control region is defined selecting the events which pass the lepton preselection cuts listed in Sec. 4.3.1, and have at least two jets with p_T greater than 30 GeV. One of the two leading jets is required to have a *JetBProbability* score higher than 0.5. From events in this control region we built *tag-probe* pairs as follows. For each event the two leading jets are considered. If the leading jet passes the *JetBProbability* cut of 0.5, that is considered a *tag*, and the sub-leading jet is the *probe*. In order to avoid any bias that could arise from the probe being always the second jet, the pair is tested also in reverse order, meaning that the sub-leading jet is tested against the *tag* selection, and in case it passes, then the leading jet is used as *probe* in an independent *tag-probe* pair. This means that from each event passing the CrtlTP cuts one can build up to two *tag-probe* pairs.

If the *tag* selection were sufficient to suppress any non top events, one could estimate the efficiency by dividing the number of *tag-probe* pairs in which the *probe* passes the analysis cut $\text{JetBProbability} > 1.4$ (*tag-pass-probe*) by the total number of *tag-probe* pairs. However this is not the case. In order to estimate the efficiency in the presence of background a variable that discriminates between true b-jets and other jets in a $t\bar{t}$ sample is chosen. The variable is the p_T of the *probe* jet. For real b-jets this variable has a peak around 60 GeV, while it does not peak for other jets. The idea is to fit simultaneously the p_T spectrum for *probe* jets in *tag-pass-probe* and *tag-fail-probe* pairs, linking together the normalizations of the two samples as follows:

$$N_{TPP} = N_s \epsilon_s + N_b \epsilon_b \quad (4.11)$$

1136

$$N_{TFP} = N_s (1 - \epsilon_s) + N_b (1 - \epsilon_b) \quad (4.12)$$

where N_{TPP} is the number of *tag-pass-probe* pairs, N_{TFP} is the number of *tag-fail-probe* pairs, N_s is the number of *tag-probe* pairs in which the probe is a b-jet, N_b is the number of *tag-probe* pairs in which the probe is a not b-jet, ϵ_s is the b-tagging efficiency, ϵ_b is the probability of identifying as b-jet a non-b-jets, i.e. the mistag rate.

A χ^2 simultaneous fit of the *probe* p_T spectrum for *tag-pass-probe* and *tag-fail-probe* pairs is performed, deriving the shapes for true b-jets and non-b-jets from the simulation, and extracting N_s , N_b , ϵ_s and ϵ_b from the fit. The result of the fit on simulation is shown in Fig. 4.6. The relevant efficiencies are:

$$\epsilon_s^{MC} = 0.7663 \pm 0.0072 \quad (4.13)$$

1145

$$\epsilon_b^{MC} = 0.208 \pm 0.015 \quad (4.14)$$

We have checked that these values are consistent with the true value for the b-tagging efficiency. The true value is computed by selecting jets that are matched within a cone of $\Delta R < 0.5$ with a generator level b-quark, and counting the fraction of those that pass the *JetBProbability* cut of 1.4. This means that the *tag-probe* method does not introduce biases within the simulation statistic accuracy.

In order to assess the robustness of the fit, 5000 toy MC samples have been generated with a statistics equivalent to the one expected in data and the same fit is performed. All the 5000 fit succeeded, and the pull distributions for ϵ_s and ϵ_b parameters are shown in Fig. 4.7. The plots show the pull of the efficiencies measured in the fit, where the pull variable for each toy i is defined as:

$$pull(\epsilon_{s(b)}) = \frac{\epsilon_{s(b)}^{\text{true}} - \epsilon_{s(b)}^i}{\sigma(\epsilon_{s(b)}^i)} \quad (4.15)$$

The pulls are centered on 0 and have σ close to 1, as expected.

An example fit for one of the toys is shown in Fig. 4.8

Before running the fit on data, the shapes used in the fit have been validated. To do so, a purer top enriched phase space has been defined by requiring exactly two jets with *JetBProbability* score higher than 1.5 and no additional b-tagged jets, rejecting also jets with p_T smaller than 30 GeV. On this purer sample we have compared data against the shape used to fit the true b-jets in the *tag-pass-probe* distribution. The result is shown in Fig. 4.9 and shows good agreement.

Finally the fit has been performed on data, as shown in Fig. 4.10, providing the following efficiencies:

$$\epsilon_s^{Data} = 0.769 \pm 0.022 \quad (4.16)$$

1166

$$\epsilon_b^{Data} = 0.121 \pm 0.054 \quad (4.17)$$

1167 Further studies have been performed to assess the effect of the relative uncertainty on
1168 the $t\bar{t}$ and tW event fractions. The same procedure described above has been applied to

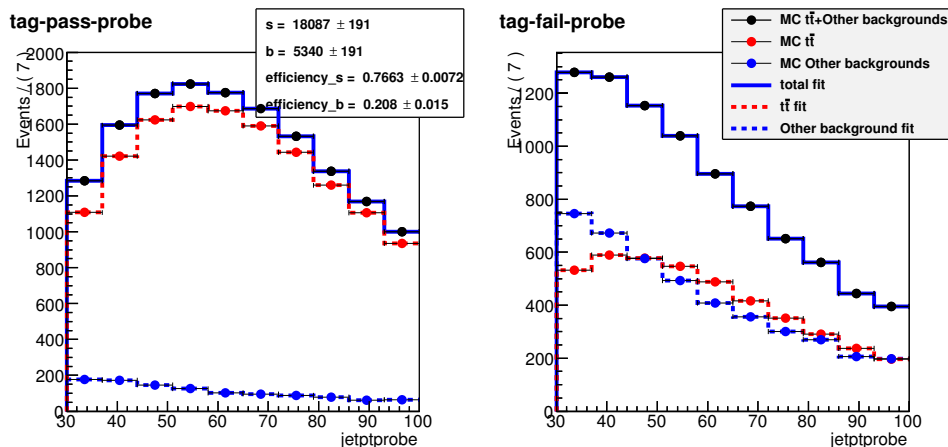


Figure 4.6.: Simultaneous fit of the *tag-pass-probe* and *tag-fail-probe* pairs in the MC.

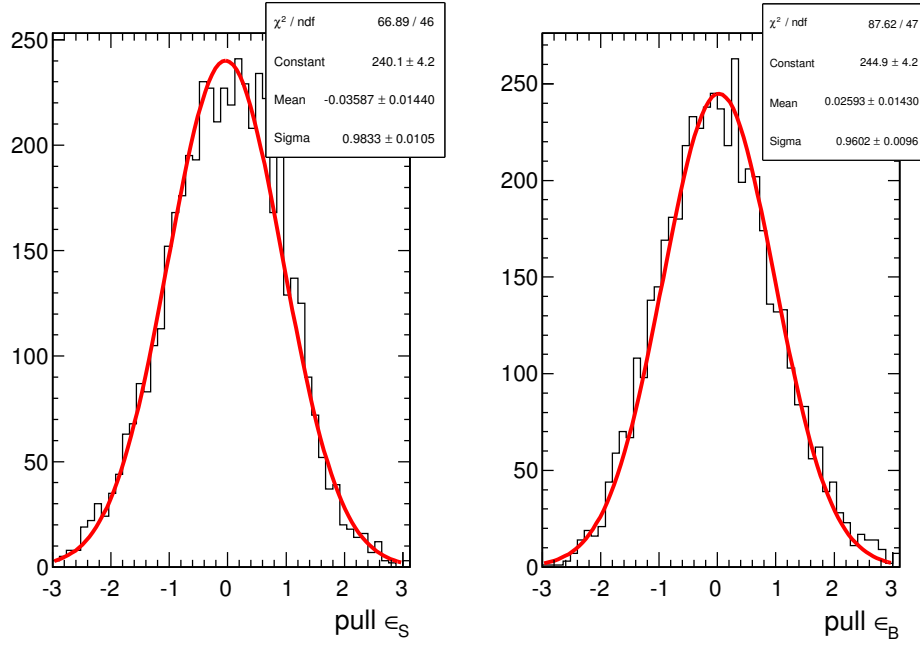


Figure 4.7.: Pulls of the ϵ_s and ϵ_b parameters in 5000 toy MC.

1169 different simulation templates obtained varying the $t\bar{t}$ and tW fractions within theoretical
 1170 uncertainties, and the effect on the parameters extracted with the fit procedure is found to
 1171 be well below the fit uncertainties.

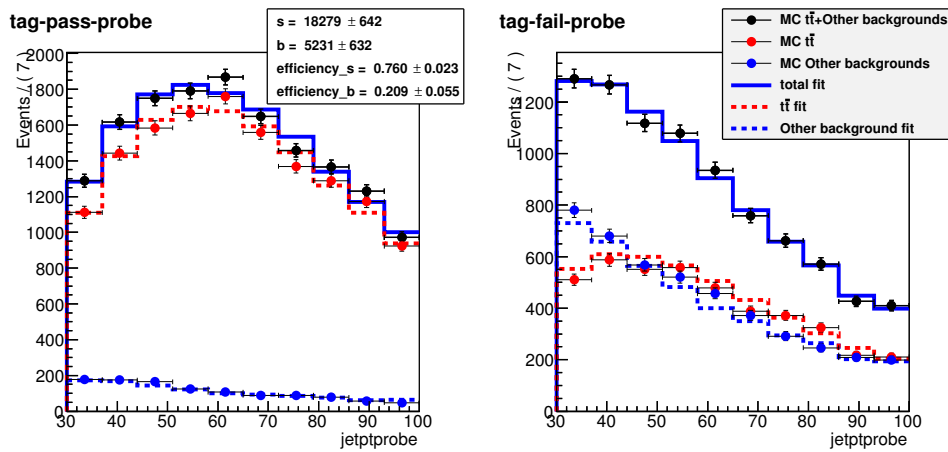


Figure 4.8.: Fit of a toy MC sample.

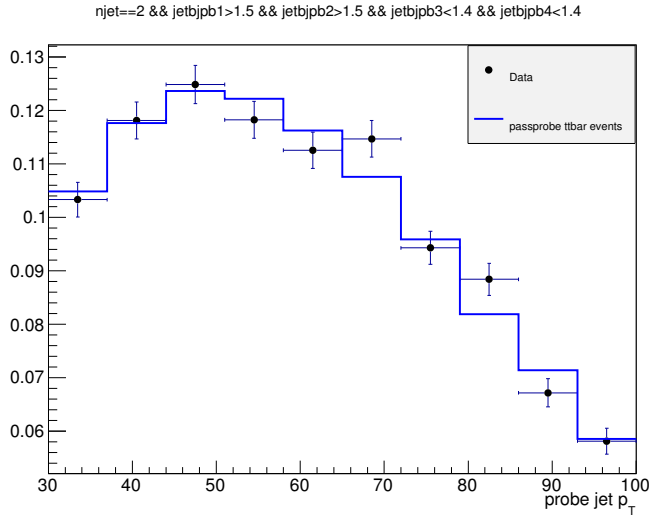


Figure 4.9.: Shape comparison for the *probe* p_T spectrum in data and in MC in a very pure $t\bar{t}$ sample.

1172 Data driven estimation

1173 In addition to the b-tagging efficiency, the other ingredient to estimate the $t\bar{t}$ background is
 1174 the process cross section. The idea is to measure the cross section in a $t\bar{t}$ enriched control
 1175 region, that is called CtrlDD. CtrlDD is defined according to the lepton preselection cuts
 1176 defined in Sec. 4.3.1, and requiring in addition at least one jet with *JetBProbability* score
 1177 higher than 1.4.

1178 From the simulation we derive the factor α that connects CtrlDD to the signal region,
 1179 calculating the ratio of $t\bar{t}$ events in the two regions:

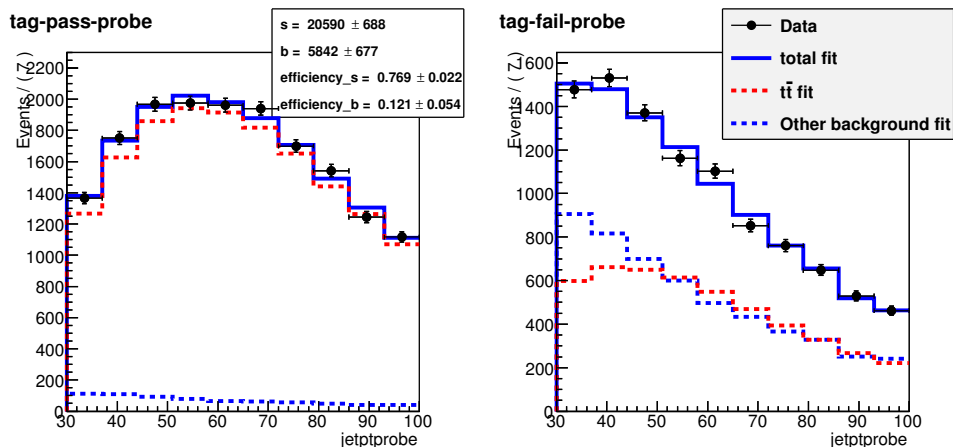


Figure 4.10.: Simultaneous fit of the *tag-pass-probe* and *tag-fail-probe* pairs in data.

$$\alpha = \frac{N_{\text{tt} MC}^{\text{SIG}}}{N_{\text{tt} MC}^{\text{CtrlDD}}} . \quad (4.18)$$

1180 The number of events in the CtrlDD region in data is counted, subtracting the expected
 1181 number of events from non- $t\bar{t}$ backgrounds, and obtaining $N_{\text{tt} Data}^{\text{CtrlDD}}$. Finally the number of
 1182 expected $t\bar{t}$ events in the signal region ($N_{\text{tt} Data}^{\text{SIG}}$) is obtained as:

$$N_{\text{tt} Data}^{\text{SIG}} = \alpha N_{\text{tt} Data}^{\text{CtrlDD}} . \quad (4.19)$$

1183 In evaluating α and its error the b-tagging efficiencies determined in Sec. 4.4.1 are
 1184 used. For each event an efficiency scale factor and a mistag rate scale factor are derived,
 1185 depending on whether the event falls in the signal or CtrlDD region.

$$SF_{\text{SIG}} = \left(\frac{1 - \epsilon_s^{\text{Data}}}{1 - \epsilon_s^{\text{MC}}} \right)^{\min(2, n_{b-jets})} \left(\frac{1 - \epsilon_b^{\text{Data}}}{1 - \epsilon_b^{\text{MC}}} \right)^{n_{\text{non}-b-\text{jets}}} \quad (4.20)$$

$$SF_{\text{CtrlDD}} = \left(\frac{\epsilon_s^{\text{Data}}}{\epsilon_s^{\text{MC}}} \right)^{(jet1 == b-jet)} \left(\frac{\epsilon_b^{\text{Data}}}{\epsilon_b^{\text{MC}}} \right)^{(jet1 == \text{non}-b-\text{jets})} \quad (4.21)$$

1186 where n_{b-jets} is the number of true b-jets in the event and $n_{\text{non}-b-\text{jets}}$ is the number of
 1187 non-b-jets in the event. The writing $jet1 == b-jet$ ($jet1 == \text{non}-b-\text{jets}$) is a boolean
 1188 flag that is true when the leading jet, the one used for the CtrlDD selection, is (not) a true
 1189 b-jet.

1190 Since the efficiency and mistag rate that have been measured on data are close to the
 1191 one in the simulation, it was decided to assume a scale factor of 1 for both b-tagging
 1192 efficiency and mis-tag rate. This means that the central values of the scale factors defined
 1193 in Eq. 4.20 and Eq. 4.21 is 1, but these numbers have an error that is derived assuming an
 1194 uncertainty on ϵ_s^{Data} and ϵ_b^{Data} that covers both the statistical error from the fit of the two
 1195 quantities and the difference with respect to the simulation. This results in an up and a
 1196 down variation of the scale factors in the signal and CtrlDD regions, that is used to derive
 1197 an error on α .

1198 A data driven estimation of the top quark background with the method described above
 1199 is performed in each of the p_T^H bins independently. The reason to make this estimation
 1200 in p_T^H bins, rather than inclusively is explained in Fig. 4.11, where the p_T^H distribution is
 1201 shown in the CtrlDD region normalized to the cross section measured by a specific CMS
 1202 analysis [67]. As shown in the ratio plot, an overall normalization factor would not be able
 1203 to accommodate for the variations of the data/simulation ratio from bin to bin.

1204 The α factors for each bin and the number of events in signal, CtrlDD regions in MC as
 1205 well as in data are listed in Tab. 4.3.

p_T^H [GeV]	N_{CTRL}^{DATA}	N_{CTRL}^{TOP}	N_{SIG}^{TOP}	α	$\Delta\alpha$
[0–15]	406.71	358.78	117.83	0.328	0.075
[15–45]	2930.14	2703.44	859.08	0.318	0.071
[45–85]	5481.02	5207.48	1506.05	0.289	0.065
[85–125]	4126.35	4032.56	861.22	0.214	0.052
[125–165]	1612.64	1654.27	304.69	0.184	0.055
[165– ∞]	647.50	760.37	201.70	0.265	0.147

Table 4.3.: Data driven scale factors related to the top quark background estimation.

₁₂₀₆ A comparison of the $m_{\ell\ell}$ distribution in the six p_T^H bins used in the analysis in CtrlDD
₁₂₀₇ after the data driven correction is shown in Fig. 4.12

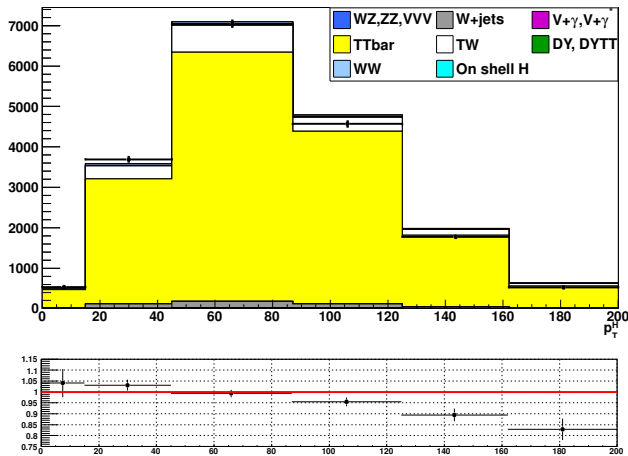


Figure 4.11.: p_T^H distribution in the CtrlDD control region.

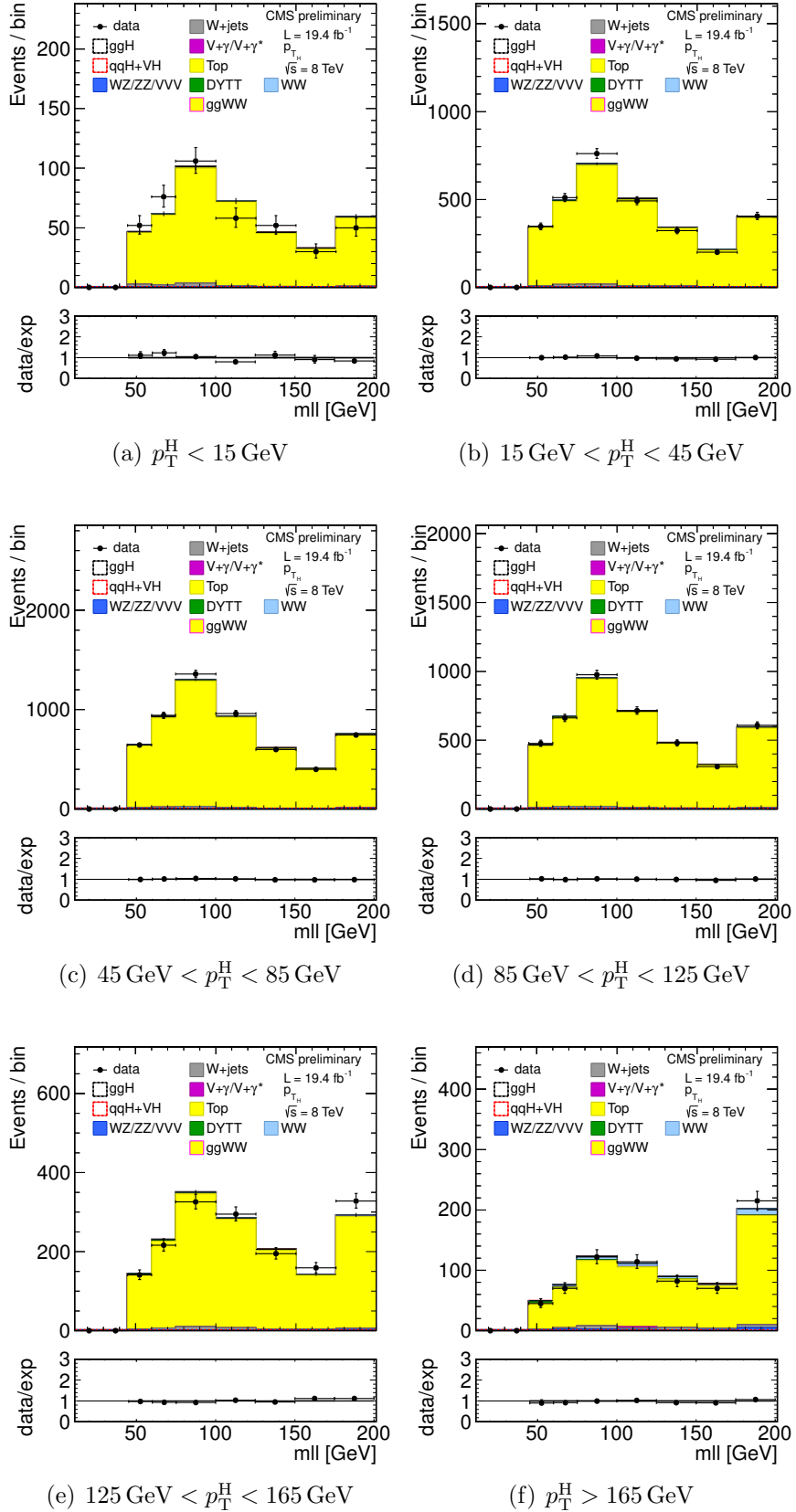


Figure 4.12.: $m_{\ell\ell}$ distributions in the CtrlDD region for the different p_T^H bins.

1208 **4.4.2. WW background**

1209 For what the $qq \rightarrow W^+W^-$ background shape is concerned, the prediction from the simula-
1210 tion is used. This background is divided into six different parts, corresponding to the six
1211 p_T^H bins defined in the analysis. The normalization of the $qq \rightarrow W^+W^-$ background is left
1212 free to float in each bin, in such a way to adjust it in order to match the data during the fit
1213 procedure. In this way the shape difference between the p_T^{WW} theory prediction and the
1214 distribution provided by the simulation, which is obtained with the MADGRAPH generator,
1215 is minimized.

1216 In figure 4.13 a comparison is shown between the p_T^{WW} spectra of two different $qq \rightarrow W^+W^-$
1217 samples: one obtained with the MADGRAPH generator and the other after applying to the
1218 same distribution a reweighting in order to match the theoretical prediction at NLO+NNLL
1219 precision.

1220 A shape discrepancy can be clearly observed and the effect becomes larger at high
1221 values of p_T^H . In order to assess the effect of this discrepancy on the shapes of the variables
1222 used for the signal extraction, $m_{\ell\ell}$ and m_T , the shapes have been checked in all p_T^H bins,
1223 comparing different MC samples. The MADGRAPH sample used for the nominal shape is
1224 compared to the MADGRAPH sample with NLO+NNLL reweighting, a POWHEG sample
1225 with NLO accuracy and an AMC@NLO sample. The results of this comparison are shown
1226 in figures 4.14 and 4.15. The shape discrepancy among the different models is included as
1227 an additional systematic uncertainty.

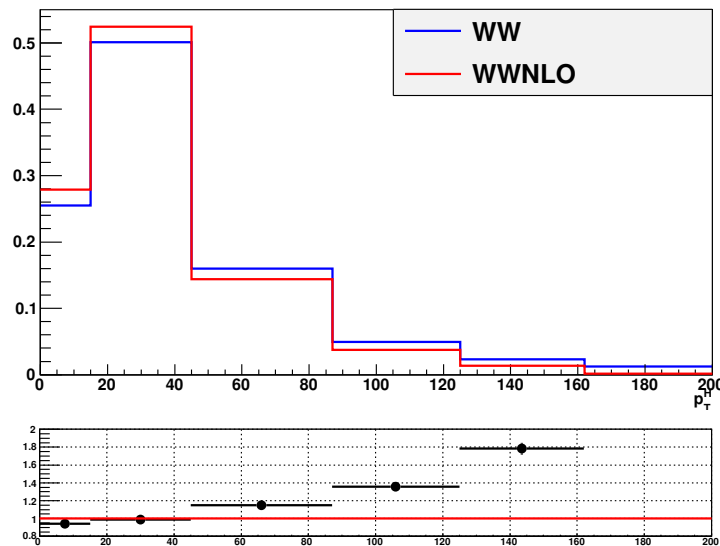


Figure 4.13.: Comparison between the p_T^{WW} distributions obtained with two different MC generators: the blue line corresponds to the MADGRAPH generator and the red line refers to the same sample in which a reweighting has been applied in order to match the theoretical prediction at NLO+NNLL precision.

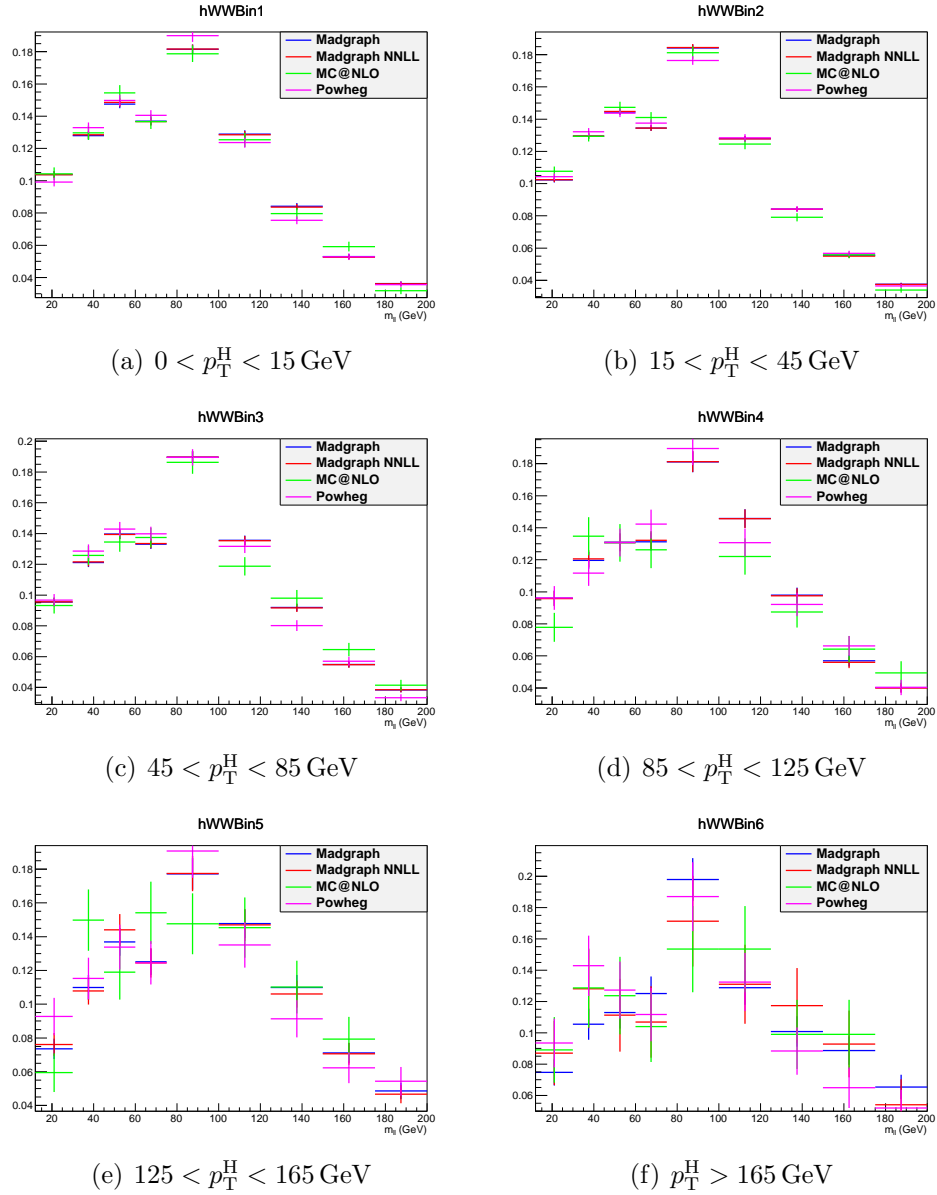


Figure 4.14.: Comparison between the default WW background sample and other theoretical models for the $m_{\ell\ell}$ distributions in every p_T^H bin.

The gluon-induced WW process, i.e. $gg \rightarrow W^+W^-$, has a sub-dominant contribution with respect to the quark-induced process, being the cross section ratio between the two of about 5%. The $m_{\ell\ell}$ and m_T shapes for this background are taken from simulation while the cross section is scaled to the approximate NLO calculation [51, 52].

The agreement of the $m_{\ell\ell}$ and m_T shapes between simulation and data for this background was checked in a signal-free control, defined selecting events with values of $m_{\ell\ell}$

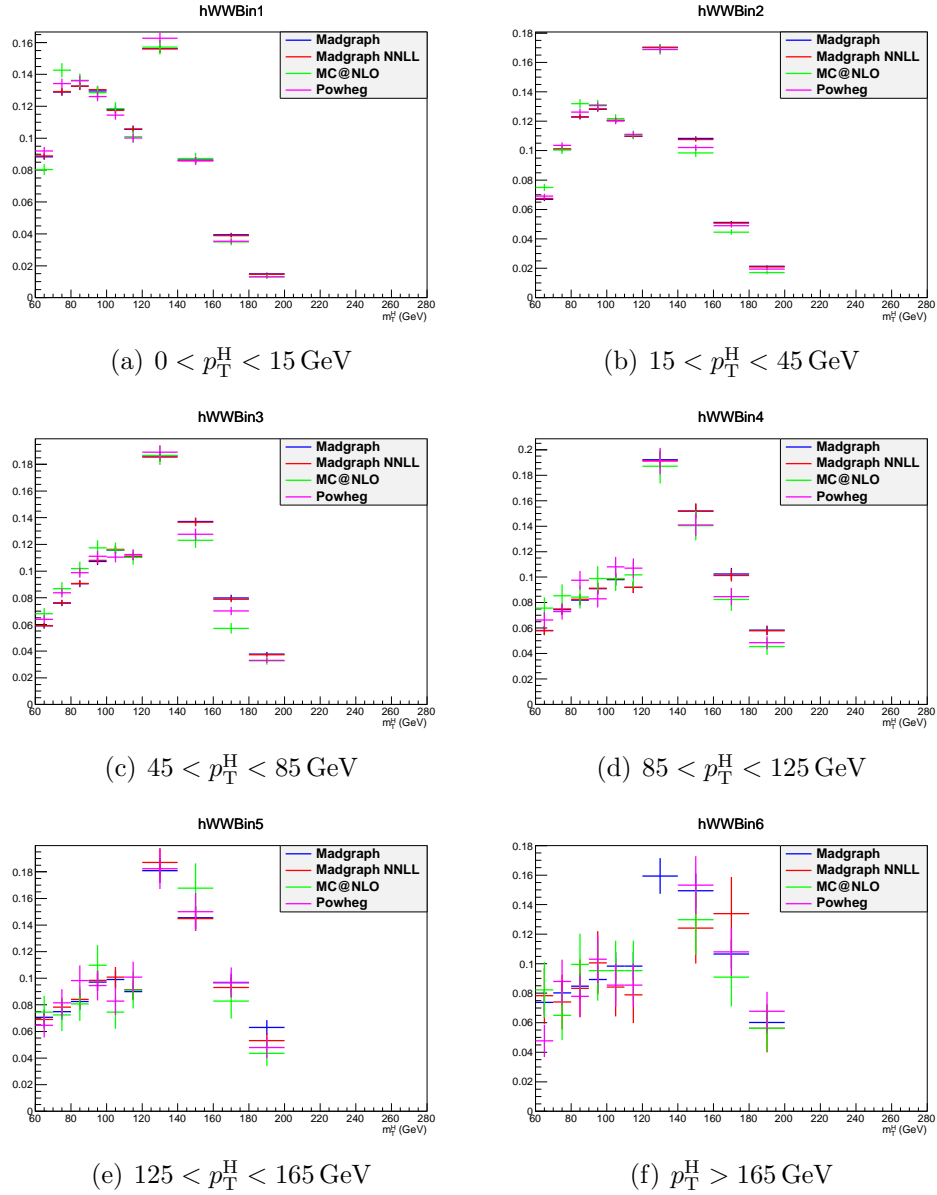


Figure 4.15.: Comparison between the default WW background sample and other theoretical models for the m_T distributions in every p_T^H bin.

1234 greater than 70 GeV. A comparison of the $m_{\ell\ell}$ and m_T shapes in data and simulation is
 1235 shown in Fig. 4.16 for events containing zero and one jets, inclusive in p_T^H .

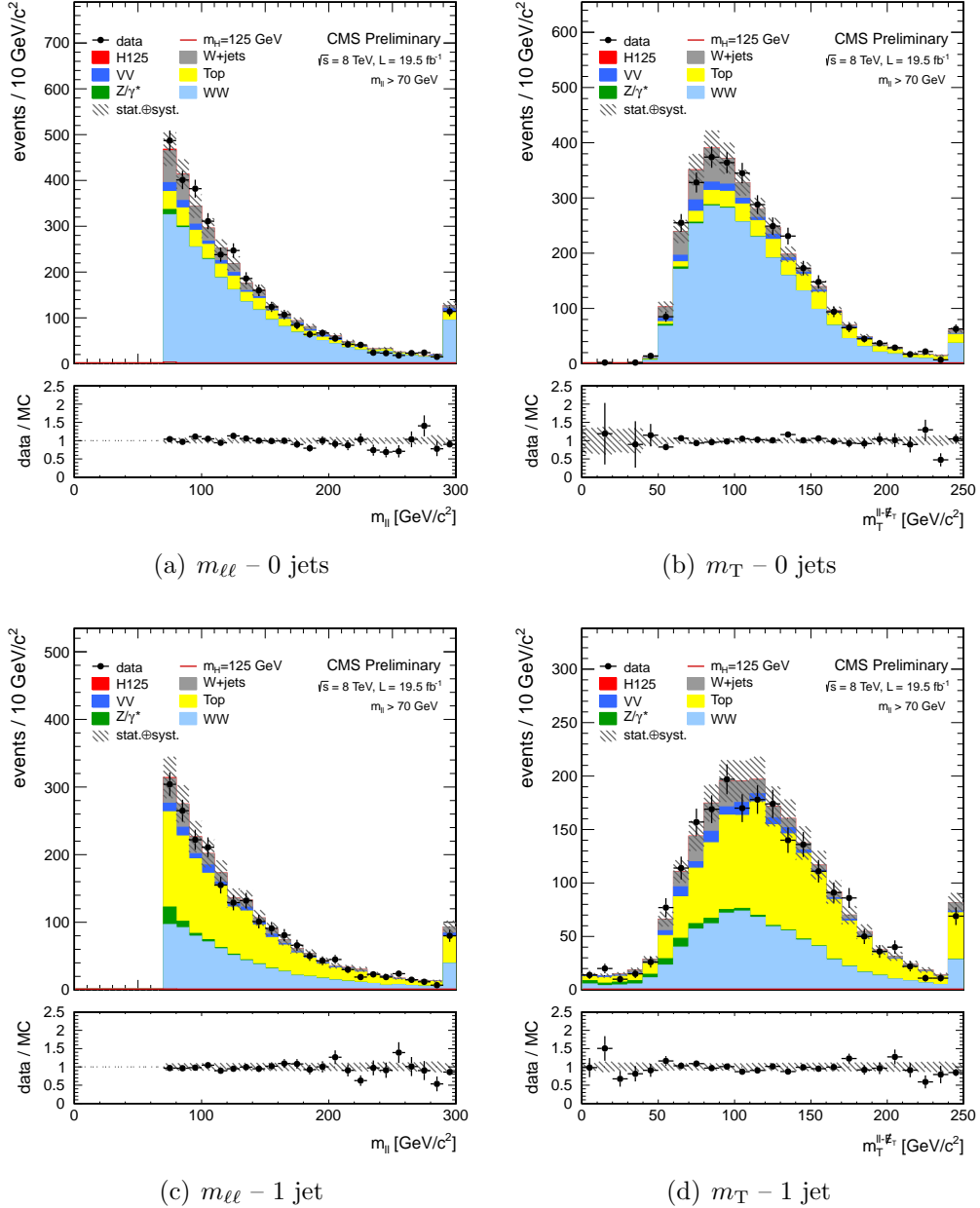


Figure 4.16.: Comparison of the $m_{\ell\ell}$ and m_T shapes in data and simulation for events with zero and 1 jets, inclusive in p_T^H . The events are required to pass the analysis requirements and, in order to define a signal-free control region, to have $m_{\ell\ell} > 70$ GeV.

1236 **4.4.3. Other backgrounds**

1237 **W+jets background**

1238 Events in which W bosons are produced in association with jets, as well as multi-jet events,
 1239 constitute a background for this analysis, because one or more jets can be misidentified as
 1240 leptons. The rate at which jets are misidentified as leptons may be not accurately described
 1241 in simulation, hence a data driven method is used to estimate this background.

1242 The idea is to estimate the background containing one or two fake leptons selecting
 1243 events with relaxed lepton quality criteria, i.e. looser with respect to the selections used at
 1244 the analysis level, and computing the efficiencies for real and fake leptons to pass the tight
 1245 lepton quality requirements of the analysis. A data-driven approach is pursued to estimate
 1246 this background. A set of loosely selected lepton-like objects, referred to as the “fakeable
 1247 object” or “denominator” from here on, is defined in a data set of events dominated by
 1248 dijet production. To measure the fake rate we count how many fakeable objects pass the
 1249 full lepton selection of the analysis, parameterized as a function of the phase space of the
 1250 fakeable lepton, therefore it is extracted in bins of η and p_T . The ratio of the fully identified
 1251 lepton, referred as “numerator”, to the fakeable objects is taken as the probability for a
 1252 fakeable object to fake a lepton:

$$\text{Fake Rate} = \frac{\#\text{of fully reconstructed leptons}}{\#\text{of fakeable objects}} \quad (4.22)$$

1253 It is then used to extrapolate from the loose leptons sample to a sample of leptons
 1254 satisfying the full selection.

1255 The definition of the denominator is of large impact in the systematic uncertainties
 1256 related to this method. For the 2012 data taking period a summary of the selections used
 1257 for the numerator and the denominator of Eq. (4.22) is shown below for electrons and
 1258 muons respectively. For electrons the denominator is defined by the following requirements:

- 1259 • $\sigma_{inj\eta} < 0.01(0.03)$ for barrel (endcap);
- 1260 • $|\Delta\phi_{in}| < 0.15(0.10)$ for barrel (endcap);
- 1261 • $|\Delta\eta_{in}| < 0.007(0.009)$ for barrel (endcap);
- 1262 • $H/E < 0.12(0.10)$ for barrel (endcap);
- 1263 • electron conversion rejection;
- 1264 • $|d_0| < 0.02$ cm;
- 1265 • $\frac{\sum_{\text{trk}} E_T}{p_T^{\text{ele}}} < 0.2$;
- 1266 • $\frac{\sum_{\text{ECAL}} E_T}{p_T^{\text{ele}}} < 0.2$;
- 1267 • $\frac{\sum_{\text{HCAL}} E_T}{p_T^{\text{ele}}} < 0.2$.

1268 For muons the selection are loosened with respect to the tight analysis selection requiring
 1269 that:

-
- 1270 • $|d_0| < 0.02 \text{ cm}$;
- 1271 • MVA isolation output > -0.6 .

1272 The dijet enriched data set used for the fake rate measurement, which is selected using
 1273 single lepton triggers with low p_T thresholds, it is not a pure sample containing just fake
 1274 leptons, but may still contain prompt leptons coming from the W and Z boson decays.
 1275 To reject muons from the W decay, the events are required to have $E_T^{\text{miss}} < 20 \text{ GeV}$ and
 1276 a W transverse mass below 20 GeV as well. Muons from the Z decay are instead remove
 1277 requiring $m_{\mu\mu} > 20 \text{ GeV}$ and $m_{\mu\mu} \notin [76, 106] \text{ GeV}$. For electrons the Z mass peak veto
 1278 is enlarged to $m_{ee} \notin [60, 120] \text{ GeV}$. Finally both electrons and muons are required to be
 1279 isolated from the leading jet in the event, i.e. $\Delta\phi(\ell, j) > 1$. The residual prompt lepton
 1280 contamination from EW processes such as W/Z+jets production, which can bias the fake
 1281 rate measurement, is estimated using simulation and subtracted from both the numerator
 1282 and denominator. The contamination from EW processes is different for the numerator
 1283 and denominator and is particularly important for relatively high lepton p_T values.

1284 In addition to the fake rate, also a prompt lepton rate is evaluated, defined as the
 1285 probability of a prompt lepton passing the loose requirements to also pass the tight analysis
 1286 selections. The prompt rate is also measured in data, defining a control region enriched in
 1287 $Z \rightarrow \ell\ell$ events, selecting dilepton events with an invariant mass of the two leptons in the Z
 1288 peak mass region.

1289 Both the fake and prompt rate are used to reweight the data samples used in the analysis
 1290 in order to obtain directly from data the contribution of the fake lepton background. The
 1291 method to apply those rates is explained below in the simple case of just one lepton in
 1292 the data sample, i.e. data selected by single lepton triggers, but can be straightforwardly
 1293 generalized to situations with more than one lepton. Suppose that the total number of
 1294 leptons passing the loose requirements, N_ℓ , is made up of N_p prompt and N_f fake leptons.
 1295 N_p and N_f cannot be directly measured but one can measure the number of events where
 1296 no leptons, N_{t0} , or one lepton, N_{t1} , pass the tight analysis requirement. These numbers are
 1297 related by the following equations:

$$\begin{aligned} N_\ell &= N_p + N_f = N_{t0} + N_{t1} \\ N_{t0} &= (1 - p)N_p + (1 - f)N_f \\ N_{t1} &= pN_p + fN_f \end{aligned} \tag{4.23}$$

1298 where p and f are the prompt and fake rates respectively. Equation (4.23) can be
 1299 inverted to obtain the number of prompt and fake leptons:

$$\begin{aligned} N_p &= \frac{1}{p - f} [(1 - f)N_{t1} - fN_{t0}] \\ N_f &= \frac{1}{p - f} [pN_{t0} - (1 - p)N_{t1}] \end{aligned} \tag{4.24}$$

The number of fake events passing the tight analysis requirement is $N_{\text{fake}} = fN_f$. The fake background contribution is estimated directly from data, applying the kinematics-dependent weights (f and p are estimated in bins of p_T and η) defined in Eq.(4.24).

The prompt and fake rate estimations after the removal of the EW contribution are shown in Tables 4.4 and 4.5 separately for electrons and muons.

Table 4.4.: Measured prompt rate for electrons and muons in bins of η , p_T . Only the statistical uncertainties are shown.

Electron prompt rate			
p_T range [GeV]	$0 < \eta \leq 1.4442$	$1.4442 < \eta \leq 1.566$	$1.566 < \eta$
$10 < p_T \leq 15$	0.5738 ± 0.0045	0.5366 ± 0.0204	0.2947 ± 0.0047
$15 < p_T \leq 20$	0.7091 ± 0.0020	0.5484 ± 0.0185	0.4477 ± 0.0034
$20 < p_T \leq 25$	0.7175 ± 0.0013	0.6297 ± 0.0067	0.6200 ± 0.0001
$25 < p_T \leq 50$	0.9219 ± 0.0002	0.8404 ± 0.0007	0.8509 ± 0.0001
$p_T > 50$	0.9693 ± 0.0002	0.9398 ± 0.0021	0.9385 ± 0.0005

Muon prompt rate		
p_T range [GeV]	$0 < \eta \leq 1.5$	$1.5 < \eta \leq 2.5$
$10 < p_T \leq 15$	0.7119 ± 0.0003	0.7582 ± 0.0006
$15 < p_T \leq 20$	0.8049 ± 0.0018	0.8495 ± 0.0001
$20 < p_T \leq 25$	0.9027 ± 0.0008	0.8948 ± 0.0012
$25 < p_T \leq 50$	0.9741 ± 0.0001	0.9627 ± 0.0002
$p_T > 50$	0.9900 ± 0.0001	0.9875 ± 0.0003

The region obtained by reversing the opposite sign lepton requirement in the analysis selection is enriched with W+jets events where one of the jets is misidentified as a lepton. The fake rate procedure can be applied to this same-sign control region to perform a closure test of the method. The results of the closure test on same-sign events gives good agreement with the expectations.

The systematic uncertainty on the prompt and fake rate estimation is evaluated by varying the jet thresholds in the dijet control sample, and an uncertainty on the background normalization is added according to the agreement with data in the same-sign control region. The systematic uncertainty amounts to about 36% of the fake background yield.

Drell-Yan to $\tau\tau$ background

The low E_T^{miss} threshold in the $e\mu$ final state requires the consideration of the contribution from $Z/\gamma^* \rightarrow \tau^+\tau^-$, that is estimated from data. This is accomplished by selecting $Z/\gamma^* \rightarrow$

Table 4.5.: Measured electrons and muons fake rates in bins of η and p_T , after the EWK correction. Only statistical uncertainties are shown.

electron fake rate				
p_T range [GeV]	$0 < \eta \leq 1$	$1 < \eta \leq 1.479$	$1.479 < \eta \leq 2$	$2 < \eta \leq 2.5$
$10 < p_T \leq 15$	0.045 ± 0.005	0.033 ± 0.004	0.008 ± 0.002	0.021 ± 0.005
$15 < p_T \leq 20$	0.044 ± 0.003	0.049 ± 0.003	0.017 ± 0.001	0.017 ± 0.002
$20 < p_T \leq 25$	0.041 ± 0.002	0.064 ± 0.003	0.025 ± 0.002	0.025 ± 0.002
$25 < p_T \leq 30$	0.059 ± 0.003	0.101 ± 0.005	0.041 ± 0.003	0.043 ± 0.003
$30 < p_T \leq 35$	0.084 ± 0.006	0.111 ± 0.009	0.058 ± 0.006	0.066 ± 0.005

muon fake rate				
p_T range [GeV]	$0 < \eta \leq 1$	$1 < \eta \leq 1.479$	$1.479 < \eta \leq 2$	$2 < \eta \leq 2.5$
$10 < p_T \leq 15$	0.131 ± 0.002	0.154 ± 0.004	0.194 ± 0.005	0.241 ± 0.009
$15 < p_T \leq 20$	0.143 ± 0.007	0.191 ± 0.012	0.235 ± 0.016	0.308 ± 0.027
$20 < p_T \leq 25$	0.198 ± 0.005	0.239 ± 0.009	0.221 ± 0.011	0.271 ± 0.021
$25 < p_T \leq 30$	0.182 ± 0.011	0.228 ± 0.018	0.195 ± 0.022	0.287 ± 0.045
$30 < p_T \leq 35$	0.170 ± 0.021	0.244 ± 0.036	0.195 ± 0.041	0.289 ± 0.111

¹³¹⁷ $\mu^+\mu^-$ events in data and replacing both muons with a simulated $\tau \rightarrow \ell\nu_\tau\bar{\nu}_\ell$ decay [41], thus
¹³¹⁸ obtaining a “hybrid” event. The Z boson four-momentum is reconstructed in data from
¹³¹⁹ the four-momenta of the daughter muons. Then a simulation step allows the replacement
¹³²⁰ of the muon objects with τ leptons, in such a way to preserve the Z boson momentum
¹³²¹ direction is preserved in its rest frame. The $Z/\gamma^* \rightarrow \tau^+\tau^-$ decay is simulated with the
¹³²² TAUOLA package [68] to correctly describe the τ -polarization effects.

¹³²³ After replacing muons from $Z/\gamma^* \rightarrow \mu^+\mu^-$ decays with simulated τ decays, the set
¹³²⁴ of pseudo-Z/ $\gamma^* \rightarrow \tau^+\tau^-$ events undergoes the reconstruction step. Good agreement in
¹³²⁵ kinematic distributions for this sample and a MC based $Z/\gamma^* \rightarrow \tau^+\tau^-$ sample is found. The
¹³²⁶ global normalization of pseudo-Z/ $\gamma^* \rightarrow \tau^+\tau^-$ events is checked in the low m_T spectrum
¹³²⁷ where a rather pure $Z/\gamma^* \rightarrow \tau^+\tau^-$ sample is expected.

¹³²⁸ This method allows to avoid the simulation of very large MC samples that would be
¹³²⁹ needed for an accurate description of this process.

¹³³⁰ ZZ, WZ and $W\gamma$ backgrounds

¹³³¹ The WZ and ZZ backgrounds are partially estimated from data when the two selected
¹³³² leptons come from the same Z boson. If the leptons come from different bosons the
¹³³³ contribution is expected to be small. The WZ component is largely rejected by requiring
¹³³⁴ only two high p_T isolated leptons in the event.

1335 The $W\gamma^{(*)}$ background, where the photon decays to an electron-positron pair, is expected
 1336 to be very small, thanks to the stringent photon conversion requirements. This background
 1337 also includes events where a real photon is produced in association with the W boson.
 1338 These events constitute a background for this analysis because the photon can interact with
 1339 the tracker material converting to an electron-positron pair.

1340 Since the WZ simulated sample has a generation level cut on the di-lepton invariant mass
 1341 ($m_{\ell\ell} > 12$ GeV) and the cross-section raises quickly with the lowering of this threshold, a
 1342 dedicated MADGRAPH sample has been produced with lower momentum cuts on two of
 1343 the three leptons ($p_T > 5$ GeV) and no cut on the third one. The surviving contribution
 1344 estimated with this sample is still very small, and since the uncertainty on the cross-section
 1345 for the covered phase space is large, a conservative 100% uncertainty has been given to it.
 1346 A k -factor for $W\gamma^*$ of 1.5 ± 0.5 based on a dedicated measurement of tri-lepton decays,
 1347 $W\gamma^* \rightarrow e\mu\mu$ and $W\gamma^* \rightarrow \mu\mu\mu$, is applied [41]. The contribution of $W\gamma^{(*)}$ is also constrained
 1348 by a closure test with same sign leptons on data, which reveals a good compatibility of the
 1349 data with the expected background.

1350 4.5. Systematic uncertainties

1351 Systematic uncertainties play an important role in this analysis where no strong mass peak
 1352 is expected due to the presence of undetected neutrinos in the final state. One of the most
 1353 important sources of systematic uncertainty is the normalization of the backgrounds that
 1354 are estimated on data control samples whenever is possible.

1355 A summary of the main sources of systematic uncertainty and the corresponding estimate
 1356 is reported in Table 4.6. A detailed description of each source of systematic uncertainty is
 1357 discussed in the following sections.

1358 4.5.1. Background normalization uncertainties

1359 The signal extraction is performed subtracting the estimated backgrounds to the event
 1360 counts in data. This uncertainty depends on the background:

- 1361 • **$t\bar{t}$ and tW backgrounds:** The efficiency on jets b-tagging is estimated using the
 1362 Tag&Probe technique in data and simulation control regions, as explained in 4.4.1. A
 1363 per-jet scale factor, which takes into account the possibly different efficiency of the
 1364 anti b-tagging selection in data and simulation, is computed by means of the efficiency
 1365 measured with the Tag&Probe method. The Tag&Probe method has been used also
 1366 to measure the mistag rates in data and simulation, which are the probability to b-tag
 1367 a jet that is not produced by the hadronization of a b quark. These factors are used
 1368 to reweigh the Top MC samples as explained in 4.4.1. The uncertainties provided by
 1369 the Tag&Probe fit are then propagated to the factor α that is used in the top data
 1370 driven estimation 4.4.1. These uncertainties are embedded in a systematic error that
 1371 affects the shape of the Top background in each p_T^H bin.

Table 4.6.: Main sources of systematic uncertainties and their estimate. The first category reports the uncertainties in the normalization of background contributions. The experimental and theoretical uncertainties refer to the effect on signal yields. A range is specified if the uncertainty varies across the p_T^H bins.

Uncertainties in backgrounds contributions	
Source	Uncertainty
t <bar>t>, tW</bar>	20–50%
W+ jets	40%
WZ, ZZ	4%
W γ (*)	30%

Effect of the experimental uncertainties on the signal and background yields	
Source	Uncertainty
Integrated luminosity	2.6%
Trigger efficiency	1–2%
Lepton reconstruction and identification	3–4%
Lepton energy scale	2–4%
E_T^{miss} modelling	2%
Jet energy scale	10%
Pileup multiplicity	2%
b mistag modelling	3%

Effect of the theoretical uncertainties on signal yield	
Source	Uncertainty
b jet veto scale factor	1–2%
PDF	1%
WW background shape	1%

Provided that the simulated samples include both tt> and tW processes, a systematic uncertainty related to the tW/tt> fraction has been included. In fact, a relative variation of the contribution of these two processes could modify the shape of the MC sample, and is thus included as a shape uncertainty affecting the top quark background shape in each p_T^H bin in a correlated way.

- **W+jets background:** It is estimated with data control sample as described in Sec.4.4.3. With 19.4 fb^{-1} at 8 TeV, the uncertainty receives similar contributions from statistics and systematic error (mainly jet composition differences between the fake rate estimation sample and the application sample), the total error being about 40%, dominated by the closure test of the method on a same-sign control region.

- **WZ, ZZ, $W\gamma^{(*)}$ backgrounds:** those backgrounds, which are expected to give a small contribution, are estimated from simulation. Uncertainties on the cross sections reported in [69, 70] are 4% for WZ and 2.5% for ZZ. A 30% uncertainty is assigned to the $W\gamma$ [71] yield and another 30% on $W\gamma^{(*)}$ contribution according to the uncertainty on the normalization study (see Sec. 4.4.3).

4.5.2. Experimental uncertainties

The following experimental systematic sources have been taken into account:

- **Luminosity:** Using the online luminosity monitoring CMS reached an uncertainty on the luminosity of 2.6% at 8 TeV.
- **Trigger efficiency.** The uncertainties for both electrons and muons are at 1-2% level, which is added together to the lepton efficiency uncertainty.
- **Lepton reconstruction and identification efficiency:** The lepton reconstruction and identification efficiencies are measured with the Tag&Probe method in data. To correct for the difference in the lepton identification efficiencies between data and MC, a scale factor is applied to MC. The uncertainties resulting from this procedure on the lepton efficiencies are 4% for electrons and 3% for muons.
- **Muon momentum and electron energy scale:** The momentum scale of leptons have relatively large uncertainties due to different detector effects. For electrons a scale uncertainty of 2% for the barrel, and 4% for the endcaps respectively, is assigned. For muons, a momentum scale uncertainty of 1.5%, independent of its pseudorapidity, is assigned.
- **E_T^{miss} modeling:** The E_T^{miss} measurement is affected by the possible mis-measurement of individual particles addressed above, as well as the additional contributions from the pile-up interactions. The effect of the missing transverse momentum resolution on the event selection is studied by applying a Gaussian smearing of 10% on the x - and y -components of the missing transverse momentum. All correlated variables, like the transverse mass, are recalculated.
- **Jet energy scale (JES) uncertainties:** It affects both the jet multiplicity and the jet kinematic variables, such as m_{jj} . We estimate this uncertainty applying variations of the official jet uncertainties on the JES (which depend on η and p_T of the jet [72]) and compute the variation of the selection efficiency.
- **b jets mistag modeling:** A fraction of signal events is rejected because erroneously identified as b jets by the b-tagging algorithms. The mistag rate, as measured with the Tag&Probe technique described in Sec. 4.4.1, comes with an uncertainty due to different modeling of the b-tagging performance in data and simulation.
- **Pileup multiplicity:** Some of the variables used in the analysis are affected by the average number of pileup interactions. The simulated events have been reweighted according the instantaneous luminosity measured on data. The error in the average

number of pileup interactions measured in data and the simulation of the modeling and physics aspects of the pileup simulation gives an uncertainty of 5% on the distribution used in the reweighting procedure. This uncertainty is propagated through all the analysis, and the estimated uncertainty on the efficiency is 2%.

4.5.3. Theoretical uncertainties

- **QCD scale uncertainties:** The uncertainties on the total cross sections due to the choice of the renormalization and factorization scale are assigned to MC-driven backgrounds. For the signal processes these uncertainties are separated in two categories: those affecting the selection efficiency and those affecting the jet bin fractions. The effect of renormalization and factorization scale on the selection efficiency is of the order of 2% for all processes. Although this analysis is inclusive in number of jets, the effect of the QCD scale variation on the jet bin migrations has to be taken into account because of the b-tagging veto efficiency. The efficiency of this selection depends on jet multiplicity and the effect of the QCD scale variation has been evaluated using the Stewart-Tackman method, as explained in 4.5.3.
- **PDFs uncertainties:** The utilization of different PDF sets can affect both the normalization and the shapes of the signal contributions. The uncertainty related due to the variations in the choice of PDFs is considered following the PDF4LHC [73, 74] prescription, using CT10, NNPDF2.1 [75] and MSTW2008 [76] PDF sets.
- **WW:** Due to the fact that the WW shape is entirely taken from simulation, the analysis is strongly relying on theoretical models and can thus be strongly affected by their uncertainties. Especially higher order QCD radiative effects have an influence on the generated WW shape. To study this impact, the shapes of the distributions produced with the MADGRAPH generator (which is the generator for the MC simulation used in the analysis) are compared to the ones produced with MC@NLO. The comparison is performed separately in each bin of p_T^H and the uncertainty includes shape differences originating from the renormalization and factorization scale choice. A comparison of the $m_{\ell\ell}$ and m_T shapes for the WW background using different MC generators is reported in section 4.4.2.

Jet multiplicity uncertainty

The jet bin uncertainty on the ggH production mode has been evaluated using the Stewart-Tackman method, following the recipe proposed in Refs. [40, 77]. Three independent nuisance parameters have to be associated with the inclusive ggH production cross sections $\sigma_{\geq 0}$, $\sigma_{\geq 1}$ and $\sigma_{\geq 2}$, which corresponds to the cross sections with ≥ 0 jets, ≥ 1 jet and ≥ 2 jets respectively. According to the agreement on the treatment of uncertainties in the combination of ATLAS and CMS results [78], these nuisance parameters are labelled as $QCDscale_{ggH}$, $QCDscale_{ggH1in}$ and $QCDscale_{ggH2in}$. However, in case the analysis is split in exclusive jet multiplicity bins, the jet bin uncertainties can be evaluated taking into

account the correct correlations among the three nuisances following the Stewart-Tackman prescription. Even though this analysis is inclusive in number of jets, the jet binning uncertainties must be included due to the presence of the b-jet veto, that introduces a dependency of the selection efficiency on the number of jets in the event. The veto efficiency has been evaluated in all the p_T^H bins defined in the analysis and as a function of jets multiplicity. The results are shown in Figs. 4.17(a) and 4.17(b). The drop of the veto efficiency at high values of p_T^H is due to the correlation with jets multiplicity.

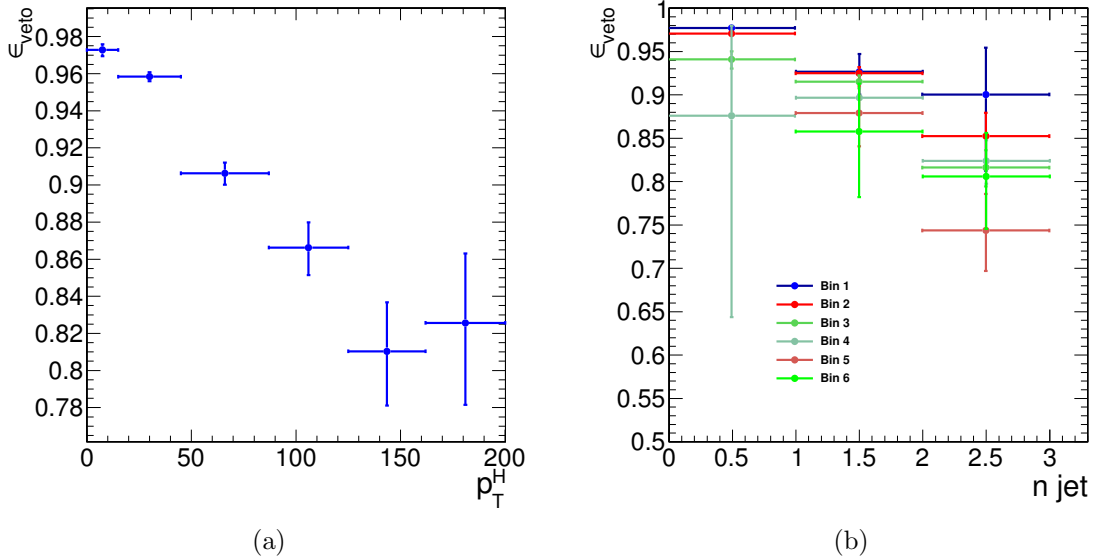


Figure 4.17.: (a) Efficiency of the b-tagging veto in different bins of p_T^H . (b) Efficiency of the b-tagging veto in different bins of p_T^H , as a function of number of jets.

The first step of this procedure is to take the inclusive ggH cross section, σ_{ggH} , and to convert the relative QCD up/down scale uncertainties, ϵ_+ and ϵ_- , to a log-normal uncertainty, i.e. $\kappa = \sqrt{\exp(\epsilon_+) \cdot \exp(\epsilon_-)}$. The exclusive cross sections, σ_0 , σ_1 and σ_2 , can be calculated starting from σ_{ggH} and using the selection efficiencies for the three jet bins. For every exclusive cross section the corresponding relative uncertainty is computed varying the renormalization (μ_R) and factorization (μ_F) scales independently of a factor 2 and 1/2, and taking the cross section value corresponding to half of the maximum variation. The inclusive cross sections are then obtained summing the exclusive cross sections and propagating the uncertainties, i.e. $\sigma_{\geq 0} = \sigma_0 + \sigma_1 + \sigma_2$, $\sigma_{\geq 1} = \sigma_1 + \sigma_2$, $\sigma_{\geq 2} = \sigma_2$.

The three nuisance parameters, including all the proper correlations among the jet bins, are defined according to Table 4.7, where the f_n constants represent the exclusive theoretical n jet bin fractions, i.e. $f_0 = \sigma_0/\sigma_{\geq 0}$, $f_1 = \sigma_1/\sigma_{\geq 0}$, $f_2 = \sigma_2/\sigma_{\geq 0}$.

Table 4.7.: Numerical calculation for the systematic uncertainties of jet binning.

Nuisance parameter	0-jet bin	1-jet bin	2-jet bin
QCDscale_ggH	$\Delta_{\geq 0}^0 = (\kappa_{\geq 0})^{\frac{1}{f_0}}$		
QCDscale_ggH1in	$\Delta_{\geq 1}^0 = (\kappa_{\geq 1})^{-\frac{f_1+f_2}{f_0}}$	$\Delta_{\geq 1}^1 = (\kappa_{\geq 1})^{\frac{f_1+f_2}{f_1}}$	
QCDscale_ggH2in		$\Delta_{\geq 2}^1 = (\kappa_{\geq 2})^{-\frac{f_2}{f_1}}$	$\Delta_{\geq 2}^2 = (\kappa_{\geq 2})$

The nuisance parameters reported in table 4.7 have then been calculated for each p_T^H bin embedding the b-jet veto efficiency and using the following formulas:

$$QCDscale_ggH = \frac{\Delta_{\geq 0}^0 \cdot f_0 \cdot \varepsilon_0 + \Delta_{\geq 1}^0 \cdot f_1 \cdot \varepsilon_1}{\Delta_{\geq 0}^0 \cdot f_0 \cdot \varepsilon_0 + \Delta_{\geq 1}^0 \cdot f_1 \cdot \varepsilon_0} , \quad (4.25)$$

$$QCDscale_ggH1in = \frac{\Delta_{\geq 1}^1 \cdot f_1 \cdot \varepsilon_1 + \Delta_{\geq 2}^1 \cdot f_2 \cdot \varepsilon_2}{\Delta_{\geq 1}^1 \cdot f_1 \cdot \varepsilon_1 + \Delta_{\geq 2}^1 \cdot f_2 \cdot \varepsilon_1} , \quad (4.26)$$

$$QCDscale_ggH2in = 1 , \quad (4.27)$$

where ε_0 , ε_1 and ε_2 are the selection efficiencies for the three jet categories. These nuisance parameters are expected to be equal to one in case the efficiency is independent on the number of jets, i.e if $\varepsilon_0 = \varepsilon_1 = \varepsilon_2$.

The numerical values obtained following this procedure are reported in Table 4.8 for each p_T^H bin.

4.5.4. Statistics uncertainty of the simulated samples

Due to the large range of weights used to correct the simulated distributions in order to match those in data, the effective size of the MC samples are sometimes smaller than the actual number of events in the sample. The statistical uncertainties of the event yields estimated from MC samples are included as nuisance parameters in the fit and have a small impact on the final result.

Table 4.8.: Values of the jet binning nuisance parameters for different p_T^H bins.

Nuisance parameter	p_T^H bin [GeV]					
	[0-15]	[15-45]	[45-85]	[85-125]	[125-165]	[165-∞]
QCDscale_ggH	0.998	0.993	0.989	1.000	1.000	1.000
QCDscale_ggH1in	0.997	0.993	0.984	0.975	0.946	0.974

1492 4.5.5. Treatment of systematic uncertainties in the shape 1493 analysis

1494 One can distinguish between normalization uncertainties, where a systematic effect is
1495 changing the normalization of a given process assuming the shape is not affected, and shape
1496 uncertainties where the actual change in the shape of the distribution is taken into account.
1497 The normalization uncertainties enter the shape analysis as a constant normalization factor,
1498 whereas for shape uncertainties the nominal and the $+1\sigma$ and -1σ shapes enter the analysis
1499 in form of three histograms with the same normalization.

1500 For the W+jets background, the shape differences for different jet p_T thresholds in the
1501 di-jet control sample are considered separately for electron and muon fakes, while the other
1502 sources of systematics are taken as normalization uncertainties as in the cut-based analysis.

1503 Effects from experimental uncertainties are studied by applying a scaling and smearing
1504 of certain variables of the physics objects, followed by a subsequent recalculation of all the
1505 correlated variables. This is done for simulation, to account for possible systematic mis-
1506 measurements of the data. All experimental sources from Section 4.5.2 but luminosity are
1507 treated both as normalization and shape uncertainties. For background with a data-driven
1508 normalization estimation, only the shape uncertainty is considered.

1509 To account for statistical uncertainties, for each distribution going into the shape analysis,
1510 the $+1\sigma$ and -1σ shapes were obtained by adding/subtracting the statistical error in each
1511 bin and renormalizing it to the nominal distribution. In addition to this procedure a
1512 constant normalization uncertainty due to the finite statistics of the MC sample used to
1513 extract the shape is assigned.

1514 4.6. Signal extraction

1515 According to the “blinding” policy of the CMS Collaboration, the strategy of the analysis
1516 has been scrutinized and approved by a selected committee of internal reviewers before
1517 looking at the data in the signal region. This approach prevents the analysts from being
1518 biased by the data in the developing phase of the analysis. Below are shown the results
1519 after having looked at the data.

1520 4.6.1. Fitting procedure

1521 The signal, including ggH, VBF, and VH production mechanisms, is extracted in each bin
 1522 of p_T^H by performing a binned maximum likelihood fit simultaneously in all p_T^H bins to a
 1523 two-dimensional template for signals and backgrounds in the $m_{\ell\ell}$ – m_T plane. The variables
 1524 used for the two-dimensional template are chosen for their power to discriminate signal
 1525 and background contributions. This is shown in Fig. 4.18, where the two-dimensional MC
 1526 distributions are shown for the signal and background processes in the 0-jets category.

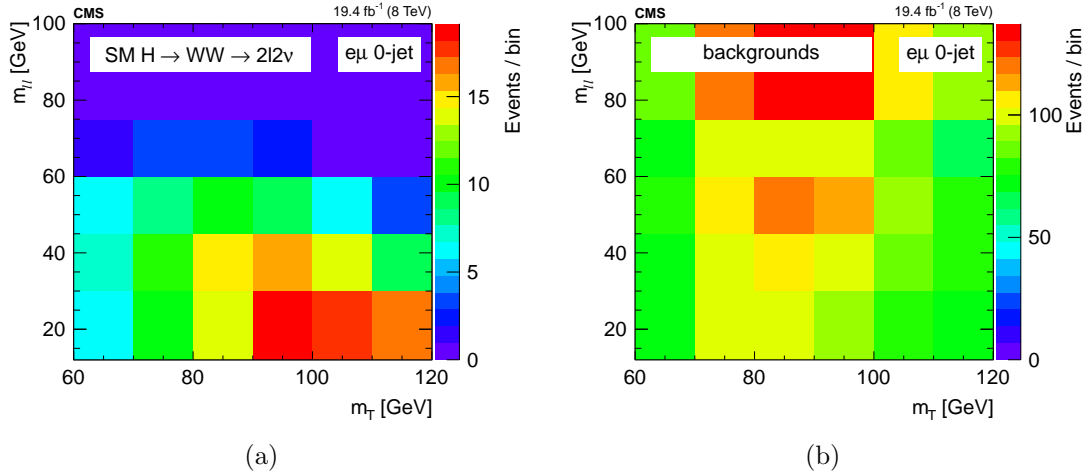


Figure 4.18.: Two-dimensional $m_{\ell\ell}$ – m_T distribution for signal (a) and background (b) processes in the 0-jets category.

1527 Six different signal strength parameters are extracted from the fit, one for each p_T^H bin.
 1528 The relative contributions of the different Higgs production mechanisms in the signal
 1529 template are taken to be the same as in the SM. The systematic uncertainty sources are
 1530 considered as nuisance parameters in the fit.

1531 The binning of the $m_{\ell\ell}$ and m_T templates is chosen to be:

- 1532 • $m_{\ell\ell}$: [12, 30, 45, 60, 75, 100, 125, 150, 175, 200]
- 1533 • m_T : [60, 70, 80, 90, 100, 110, 120, 140, 160, 180, 200, 220, 240, 280]

1534 To avoid a dependence of the results on the variables used for the template fit, $m_{\ell\ell}$ and
 1535 m_T need to be uncorrelated with respect to p_T^H . This has been verified and the correlation
 1536 between the discriminating variables and p_T^H is shown in Fig. 4.19 and Fig. 4.20 for ggH
 1537 and VBF production modes respectively.

1538 The relative contribution for different production mechanisms in the input signal template
 1539 is taken to be the same as the SM. The signal strength μ in each bin, i.e. the ratio between
 1540 the measured cross section and the SM one, $\mu = \sigma/\sigma_{SM}$, is allowed to float between -10 and
 1541 +10, thus allowing negative values. This is mainly intended to allow the error bars to float
 1542 below 0.

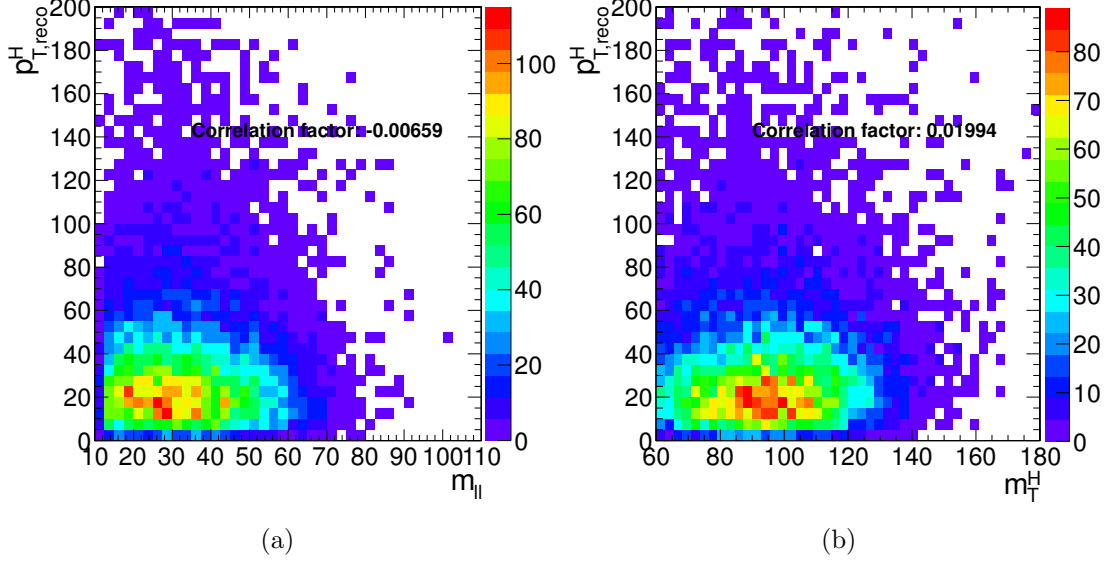


Figure 4.19.: Correlation between p_T^H and $m_{\ell\ell}$ (a) and between p_T^H and m_T (b) after the full selection for the ggH production mode.

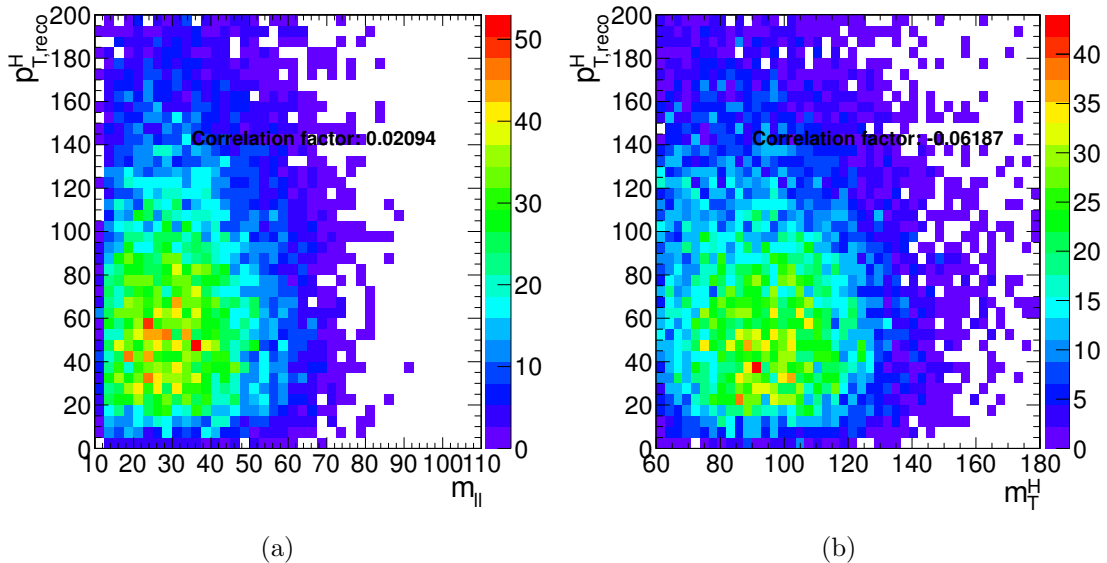


Figure 4.20.: Correlation between p_T^H and $m_{\ell\ell}$ (a) and between p_T^H and m_T (b) after the full selection for the VBF production mode.

Because of detector resolution effects, some of the reconstructed $H \rightarrow WW$ signal events might originate from outside the fiducial phase space. These out-of-fiducial signal events cannot be precisely handled by the unfolding procedure and must be subtracted from the measured spectrum. The p_T^H distribution of the out-of-fiducial signal events is taken from

1547 simulation, and each bin is multiplied by the corresponding measured signal strength before
1548 performing the subtraction.

1549 At the end, the number of events in each bin i of the measured spectrum is:

$$N_i = \mu_i(s_i - f_i) , \quad (4.28)$$

1550 where s_i and f_i are respectively the number of signal and fake events expected from
1551 simulation and μ_i is the measured signal strength.

1552 The fit makes use of the binned maximum likelihood approach. The likelihood function,
1553 \mathcal{L} , restricted to the p_T^H bin j , can be written as: **CHECK!!**

$$\mathcal{L}(data|\mu_j, \theta) = \prod_{i=0}^{N_{\text{bins}}} \frac{(\mu_j s_i(\theta) + b_i(\theta))^{n_i}}{n_i!} e^{-\mu_j s_i(\theta) - b_i(\theta)} \cdot p(\tilde{\theta}|\theta) , \quad (4.29)$$

1554 where $data$ corresponds to the experimental observation and μ_j is the signal strength in
1555 the bin j , i.e. the parameter of interest of the fit, which multiplies the signal yield. The
1556 index i runs over the bins of the $m_{\ell\ell}-m_T$ two-dimensional histogram corresponding the p_T^H
1557 bin j , s_i and b_i are the expected number of signal and background events respectively in bin
1558 i , and n_i is the total number of observed events in bin i . The set of parameters θ represents
1559 the full suite of nuisance parameters used to incorporate the systematic uncertainties. Each
1560 nuisance parameter is constrained in the fit including the prior distributions functions $p(\tilde{\theta}|\theta)$
1561 in the likelihood, where $\tilde{\theta}$ is the set of default values for the θ parameters. For the major part
1562 of the nuisance parameters a log-normal prior distribution is used, with a standard deviation
1563 corresponding to the given systematic uncertainty. For some nuisance parameters, as the
1564 ones related to the statistical uncertainty coming from the background measurement in data
1565 control regions, a Gamma distribution is instead recommended. A log-uniform distribution
1566 is used for the uncertainty related to the normalization of background contributions that
1567 are left unconstrained in the fit, such as the WW background process. Finally, some of
1568 the experimental uncertainties, related to the shape of signal and background processes,
1569 are modelled by means of additional histograms as explained in Sec. 4.5.5. The nuisance
1570 parameters correlations across different p_T^H bins are taken into account. Moreover the
1571 nuisance parameters can also be correlated (or anti-correlated) between signal and different
1572 background processes. As an example, the uncertainty related to the integrated luminosity
1573 measurement is fully correlated for all the signal and background processes.

1574 Before running the fit on the data, the same procedure has been applied to the so called
1575 *Asimov data set*¹, which provides a simple method to estimate the signal sensitivity before
1576 looking at the data [79].

¹In a parallel reality imagined by the science fiction writer I. Asimov, politics was run in a peculiar way: instead of mobilizing millions of people to cast their vote to deliberate on something, an algorithm was used to select an individual “average” person, and then this person was asked to take the decision on that matter.

1577 4.6.2. Signal and background yields

1578 A comparison of data and background prediction is shown in Fig. 4.21, where the $m_{\ell\ell}$
 1579 distribution is shown for the six p_T^H bins. Distributions correspond to the m_T window of
 1580 [60, 110] GeV, in order to emphasize the signal contribution [41]. The m_T distributions are
 1581 shown in Fig. 4.22 and correspond to the $m_{\ell\ell}$ window of [12, 75] GeV.

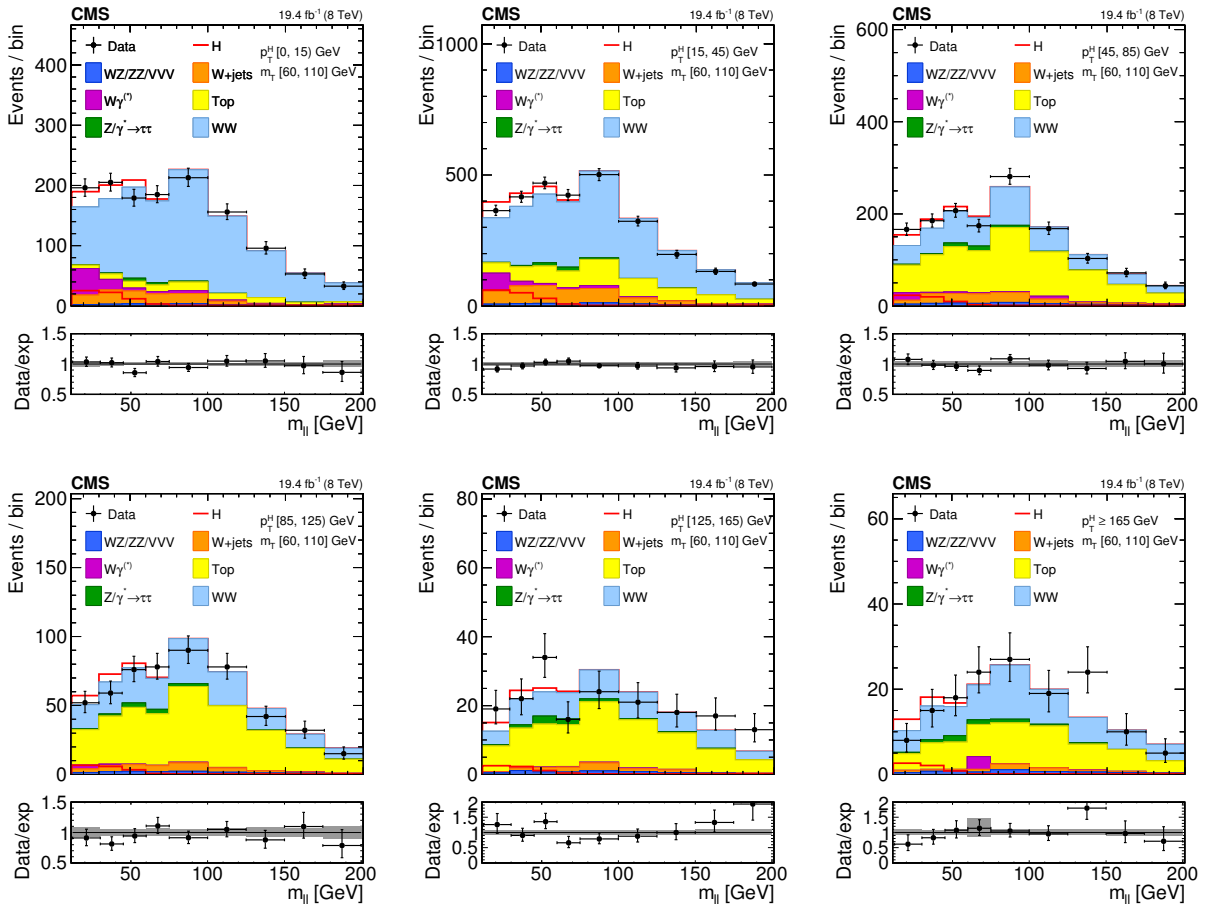


Figure 4.21.: Distributions of the $m_{\ell\ell}$ variable in each of the six p_T^H bins. Background normalizations correspond to the values obtained from the fit. Signal normalization is fixed to the SM expectation. The distributions are shown in an m_T window of [60,110] GeV in order to emphasize the Higgs boson (H) signal. The signal contribution is shown both stacked on top of the background and superimposed to it. Ratios of the expected and observed event yields in individual bins are shown in the panels below the plots. The uncertainty band shown in the ratio plot corresponds to the envelope of systematic uncertainties after performing the fit to the data.

1582 The signal and background yields after the analysis selection are reported in Table 4.9.

1583 The spectrum shown in Fig. 4.23 is obtained after having performed the fit and after
 1584 the subtraction of the out-of-fiducial signal events, but before undergoing the unfolding pro-

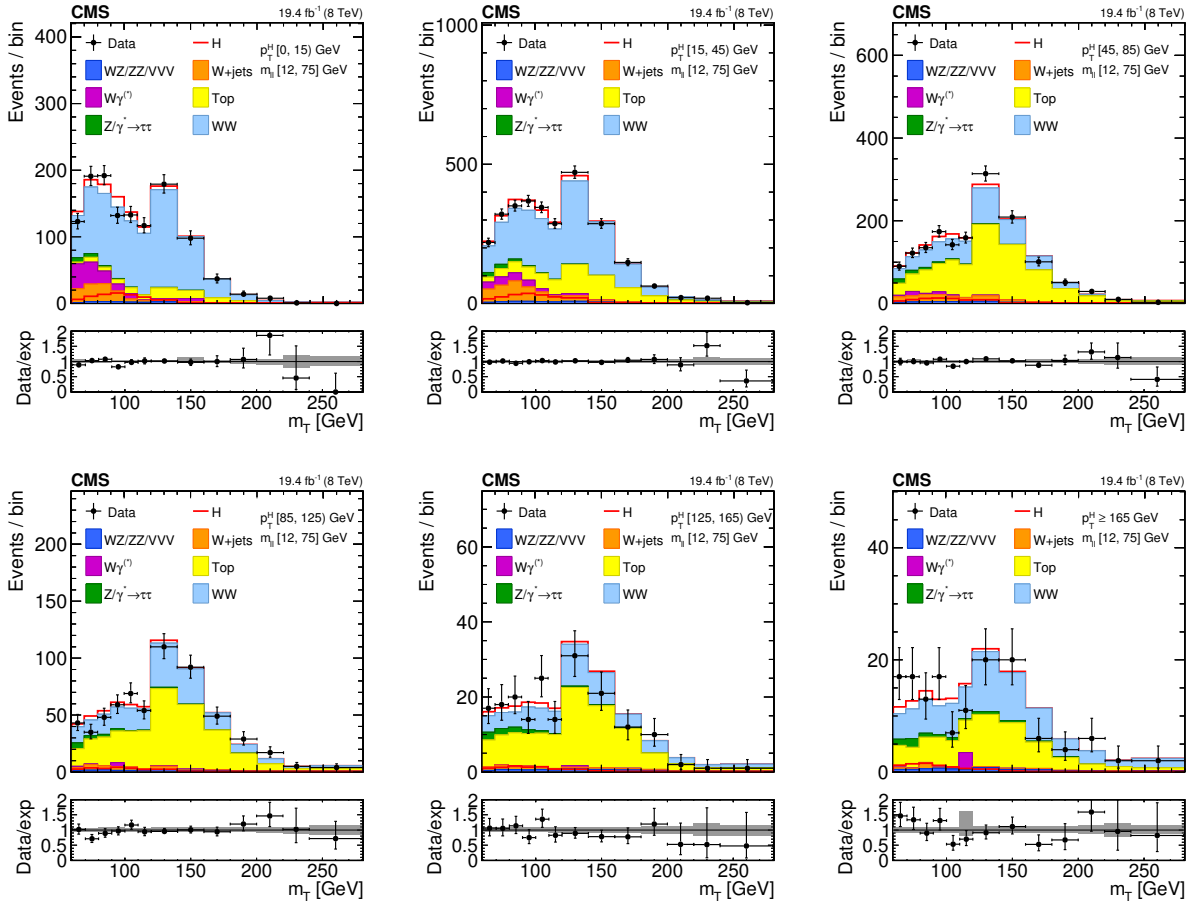


Figure 4.22.: Distributions of the m_T variable in each of the six p_T^H bins. Background normalizations correspond to the values obtained from the fit. Signal normalization is fixed to the SM expectation. The distributions are shown in an $m_{\ell\ell}$ window of $[12, 75]$ GeV in order to emphasize the Higgs boson (H) signal. The signal contribution is shown both stacked on top of the background and superimposed to it. Ratios of the expected and observed event yields in individual bins are shown in the panels below the plots. The uncertainty band shown in the ratio plot corresponds to the envelope of systematic uncertainties after performing the fit to the data.

Table 4.9.: Signal prediction, background estimates and observed number of events in data are shown in each p_T^H bin for the signal after applying the analysis selection requirements. The total uncertainty on the number of events is reported. For signal processes, the yield related to the ggH are shown, separated with respect to the contribution of the other production mechanisms (XH=VBF+VH). The WW process includes both quark and gluon induced contribution, while the Top process takes into account both $t\bar{t}$ and tW .

p_T^H [GeV]	0-15	15-45	45-85	85-125	125-165	165- ∞
ggH	73 ± 3	175 ± 5	59 ± 3	15 ± 2	5.1 ± 1.5	4.9 ± 1.4
XH=VBF+VH	4 ± 2	15 ± 4	16 ± 4	8 ± 2	3.8 ± 1.1	3.0 ± 0.8
Out-of-fiducial	9.2 ± 0.5	19.9 ± 0.7	11.4 ± 0.6	4.4 ± 0.3	1.6 ± 0.2	2.4 ± 0.2
Data	2182	5305	3042	1263	431	343
Total background	2124 ± 128	5170 ± 321	2947 ± 293	1266 ± 175	420 ± 80	336 ± 74
WW	1616 ± 107	3172 ± 249	865 ± 217	421 ± 120	125 ± 60	161 ± 54
Top	184 ± 38	1199 ± 165	1741 ± 192	735 ± 125	243 ± 51	139 ± 49
W+jets	134 ± 5	455 ± 10	174 ± 6	48 ± 4	14 ± 3	9 ± 3
WZ+ZZ+VVV	34 ± 4	107 ± 10	71 ± 7	29 ± 5	14 ± 3	13 ± 4
$Z/\gamma^* \rightarrow \tau^+\tau^-$	23 ± 3	67 ± 5	47 ± 4	22 ± 3	12 ± 2	10 ± 2
$W\gamma^{(*)}$	132 ± 49	170 ± 58	48 ± 30	12 ± 9	3 ± 3	5 ± 10

1585 cedure. The theoretical distribution after the detector simulation and event reconstruction
 1586 is also shown for comparison.

1587 In order to assess the robustness of the fit, several toy MC samples have been produced,
 1588 with a statistical accuracy corresponding to the one expected in data. The distribution
 1589 of the signal strengths extracted in each bin using the toy MC samples and the their pull
 1590 distributions are shown in Fig. 4.24.

1591 4.7. Unfolding

1592 To facilitate comparisons with theoretical predictions or other experimental results, the
 1593 signal extracted performing the fit has to be corrected for detector resolution and efficiency
 1594 effects and for the efficiency of the selection defined in the analysis. An unfolding procedure
 1595 is used relying on the ROOUNFOLD package [80], which provides the tools to run various
 1596 unfolding algorithms.

1597 The basic principle behind the unfolding procedure in this analysis is to use MC signal
 1598 samples to make the “true” distribution of the variable of interest, which is obtained using
 1599 simulated events before particle interaction with the detector, and the same distribution
 1600 obtained using events reconstructed after the full GEANT4 simulation of the CMS detector
 1601 and event reconstruction. These two distributions are used to calculate the detector response
 1602 matrix M :

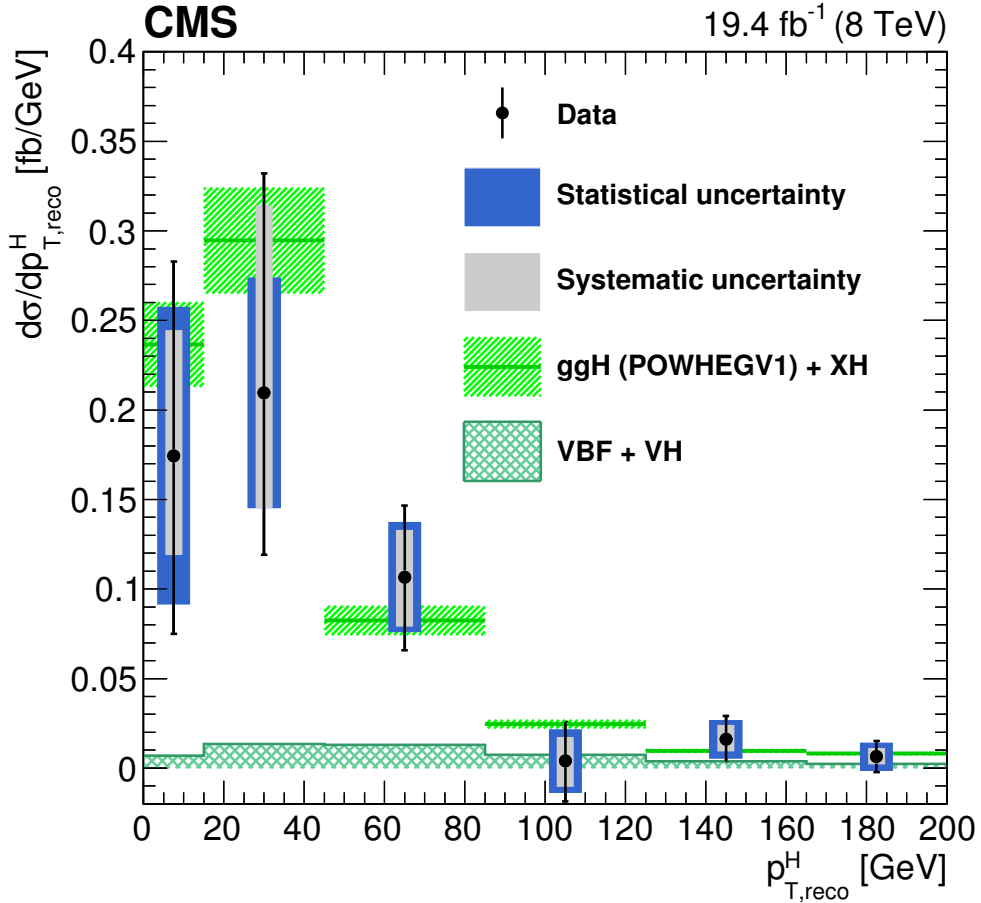


Figure 4.23.: Differential Higgs boson production cross section as a function of the reconstructed p_{T}^H , before applying the unfolding procedure. Data values after the background subtraction are shown together with the statistical and the systematic uncertainties, determined propagating the sources of uncertainty through the fit procedure. The line and dashed area represent the SM theoretical estimates in which the acceptance of the dominant ggH contribution is modelled by POWHEG V1. The sub-dominant component of the signal is denoted as XH=VBF+VH, and is shown with the cross filled area separately.

$$R_i^{\text{MC}} = \sum_{j=1}^n M_{ij} T_j^{\text{MC}} \quad , \quad (4.30)$$

where R^{MC} and T^{MC} are two n -dimensional vectors representing the distribution before and after event processing through CMS simulation and reconstruction. The dimension n of the two vectors corresponds to the number of bins in the distributions, equal to six in this analysis. The response matrix M includes all the effects related to the detector and

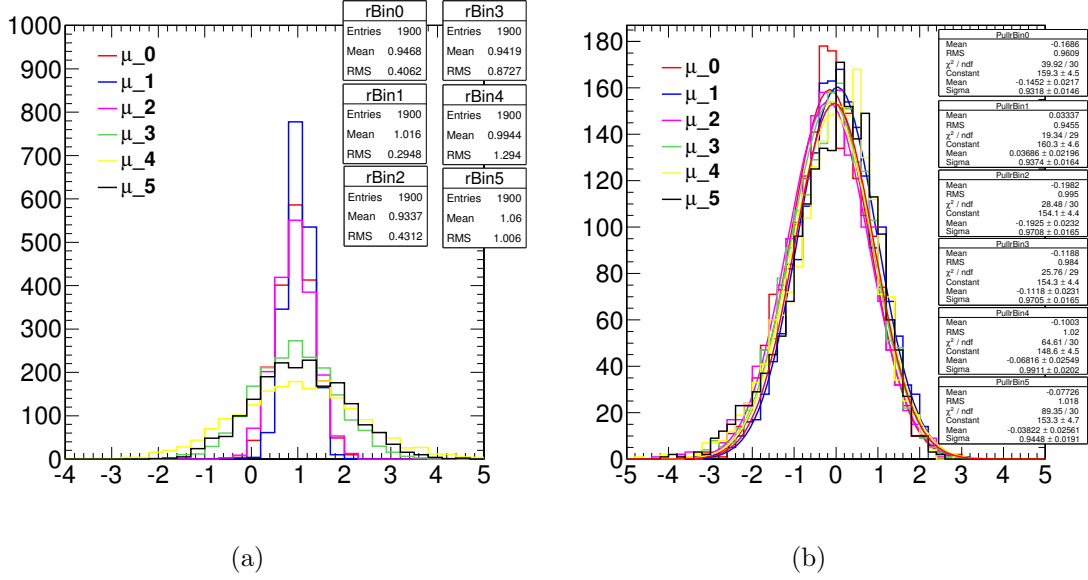


Figure 4.24.: Signal strength distribution as extracted from the fit of toy MC samples (a). Distribution of the pull of the signal strength parameters (b).

analysis selection that affect the R^{MC} distribution. The goal of the unfolding procedure is to obtain the T^{truth} distribution starting from the measured R^{observed} distribution by inverting the matrix M . To avoid the large variance and strong negative correlation between the neighbouring bins [42], the unfolding procedure in this analysis relies on the singular value decomposition [81] method based on the Tikhonov regularization function. Since the response matrix is in general limited by the statistical uncertainties of simulated samples and given the finite data statistical accuracy, a simple inversion could lead to large fluctuations between bins in the unfolded result. In particular, if the off-diagonal elements of the response matrix are sizeable, the unfolded distribution has large variance and strong negative correlations between the neighbouring bins [42]. Several unfolding methods with regularization are available in literature, such as a method based on the Bayes' theorem, which overcome the unfolding instability using an iterative procedure [82]. One possible solution is the utilization of regularization methods. Such methods introduce a regularization function that controls the smoothness of the distribution and depends generally on one regularization parameter, which can be controlled to achieve the desired degree of smoothness. The choice of the regularization parameter is particularly critical, and it should represent an optimal trade-off between taming the fluctuations in the unfolded result, and biasing the unfolded distribution towards the one used to build the response matrix. The main feature of this method is the use of the singular value decomposition of the response matrix, including an additional term to suppress the oscillatory component of the solution, i.e. the regularization term, which represents some *a priori* knowledge of the final solution. The regularization parameter is chosen to obtain results that are robust against numerical instabilities and statistical fluctuations, following the prescription

described in Ref. [81]. **Maybe I should add an appendix describing the SVD method in details**

The response matrix is built as a two-dimensional histogram, with the generator-level p_T^H on the y axis and the same variable after the reconstruction on the x axis, using the same binning for both distributions. The resulting detector response matrix, including all signal sources and normalized by row, is shown in Fig. 4.25(a). The value of the diagonal bins corresponds to the stability S . The same matrix, normalized by column, is shown in Fig. 4.25(b). In this case the diagonal bins correspond to the purity P . The S and P parameters, defined in Sec. 4.3, provide an estimate of the p_T^H resolution and migration effects. The main source of bin migrations effects in the response matrix is the limited resolution in the measurement of E_T^{miss} .

The resulting detector response matrix, which includes the effects of all signal sources and is represented by normalizing each row to unity is shown in Fig. 4.25(a). This representation shows the stability S in the diagonal bins, where S is defined as the ratio of the number of events generated and reconstructed in a given bin, and the number of events generated in that bin. In addition, a deconvolution matrix is constructed by normalizing each column to unity and is shown in Fig. 4.25(b). This latter representation shows the purity P in the diagonal bins, where P is defined as the ratio of the number of events generated and reconstructed in a given bin, and the number of events reconstructed in that bin. The S and P parameters provide an estimate of the p_T^H resolution and of migration effects. The response matrix built including all signal sources is shown in Fig. 4.25. In order to point out either the purity or the stability in diagonal bins, each column or row of the matrix was respectively normalized to unity. The matrix obtained in the first case is what is actually called detector response matrix, while in the other case the matrix is usually referred to as detector deconvolution matrix.

Several closure tests are performed in order to validate the unfolding procedure. To estimate the uncertainty in the unfolding procedure due to the particular model adopted for building the response matrix, two independent gluon fusion samples are used, corresponding to two different generators: POWHEG V1 and JHUGEN generators, both interfaced to PYTHIA 6.4. The JHUGEN generator sample is used to build the response matrix while the POWHEG V1 sample is used for the measured and the MC distributions at generator level. The result of this test shows good agreement between the unfolded and the distribution from MC simulation.

In order to further prove the choice of the regularization parameter, a large number of simulated pseudo-experiments has been generated to verify that the coverage of the unfolded uncertainties obtained with this procedure is as expected. From each pseudo-experiment the reconstructed p_T^H spectrum is obtained and then unfolded using the procedure described above, including only the statistical uncertainties. The coverage is calculated for each p_T^H bin, counting the number of pseudo-experiments for which the statistical uncertainty covers the true value. The confidence intervals are calculated using the Clopper-Pearson approach, and the results are shown in Table 4.10 for different values of the regularization parameter: starting from $k_{\text{reg}} = 2$ (stronger regularization) up to $k_{\text{reg}} = 5$ (weaker regularization). The criterion for choosing the best k_{reg} value is to increase the regularization as much as possible

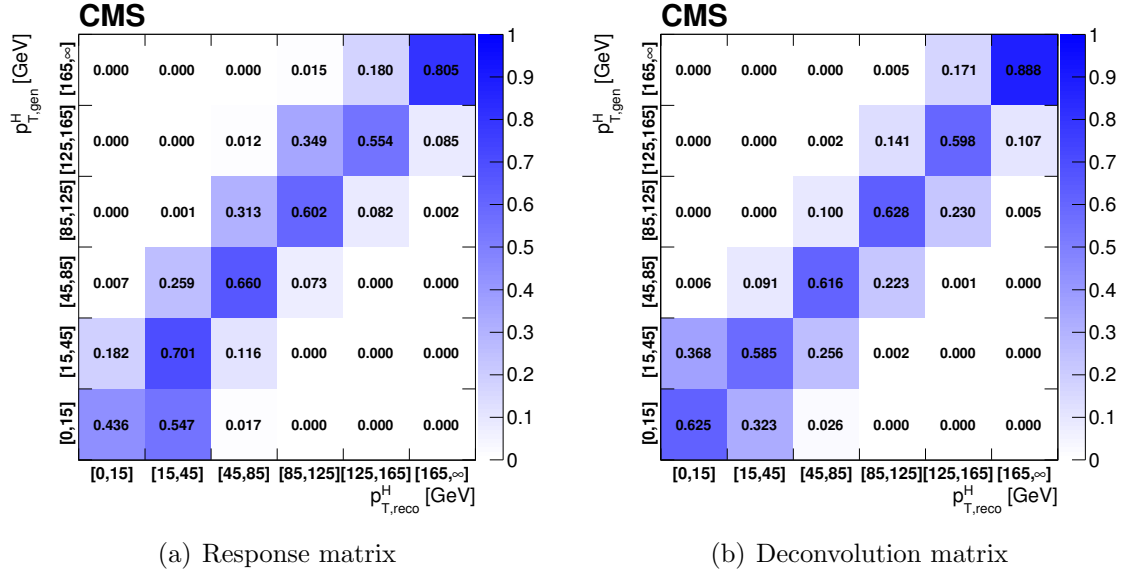


Figure 4.25.: Response matrix (a) and deconvolution matrix (b) including all signal processes. The matrices are normalized either by row (a) or by column (b) in order to show the purity or stability respectively in diagonal bins.

Table 4.10.: Coverage interval for each bin and for different values of the regularization parameter, obtained using pseudo-experiments.

p_T^H bin [GeV]	Coverage			
	$k_{\text{reg}} = 2$	$k_{\text{reg}} = 3$	$k_{\text{reg}} = 4$	$k_{\text{reg}} = 5$
0–15	$0.654^{+0.015}_{-0.016}$	$0.704^{+0.015}_{-0.015}$	$0.727^{+0.014}_{-0.015}$	$0.755^{+0.014}_{-0.014}$
15–45	$0.701^{+0.015}_{-0.015}$	$0.665^{+0.015}_{-0.016}$	$0.683^{+0.015}_{-0.015}$	$0.733^{+0.014}_{-0.015}$
45–85	$0.717^{+0.014}_{-0.015}$	$0.706^{+0.015}_{-0.015}$	$0.709^{+0.015}_{-0.015}$	$0.716^{+0.014}_{-0.015}$
85–125	$0.634^{+0.016}_{-0.016}$	$0.681^{+0.015}_{-0.015}$	$0.714^{+0.015}_{-0.015}$	$0.739^{+0.014}_{-0.015}$
125–165	$0.599^{+0.015}_{-0.016}$	$0.650^{+0.015}_{-0.016}$	$0.700^{+0.015}_{-0.015}$	$0.751^{+0.014}_{-0.014}$
165–∞	$0.632^{+0.016}_{-0.016}$	$0.674^{+0.015}_{-0.015}$	$0.701^{+0.015}_{-0.015}$	$0.722^{+0.014}_{-0.015}$

¹⁶⁷³ without introducing a bias, i.e. until a 68% coverage is fulfilled. This criterion leads to the
¹⁶⁷⁴ same result as the prescription described in Ref. [81], strengthening the choice of $k_{\text{reg}} = 3$.

¹⁶⁷⁵ 4.7.1. Treatment of systematic uncertainties

¹⁶⁷⁶ An important aspect of this analysis is the treatment of the systematic uncertainties and
¹⁶⁷⁷ the error propagation through the unfolding procedure. The sources of uncertainty are

1678 divided into three categories, depending on whether the uncertainty affects only the signal
1679 yield (type A), both the signal yield and the response matrix (type B), or only the response
1680 matrix (type C). These three classes propagate differently through the unfolding procedure.

1681 Type A uncertainties are extracted directly from the fit in the form of a covariance
1682 matrix, which is passed to the unfolding tool as the covariance matrix of the measured
1683 distribution. The nuisance parameters belonging to this category are the background shape
1684 and normalization uncertainties. To extract the effect of type A uncertainties a dedicated
1685 fit is performed, fixing to constant all the nuisance parameters in the model, but type A
1686 nuisance parameters. The correlation matrix among the six signal strengths corresponding
1687 to the six p_T^H bins, including all type A uncertainties, is shown in Fig. 4.26. The correlation
1688 $\text{cor}(i,j)$ of bins i and j is defined as:

$$\text{cor}(i,j) = \frac{\text{cov}(i,j)}{s_i s_j} \quad , \quad (4.31)$$

1689 where $\text{cov}(i,j)$ is the covariance of bins i and j , and (s_i, s_j) are the standard deviations
1690 of bins i and j , respectively.

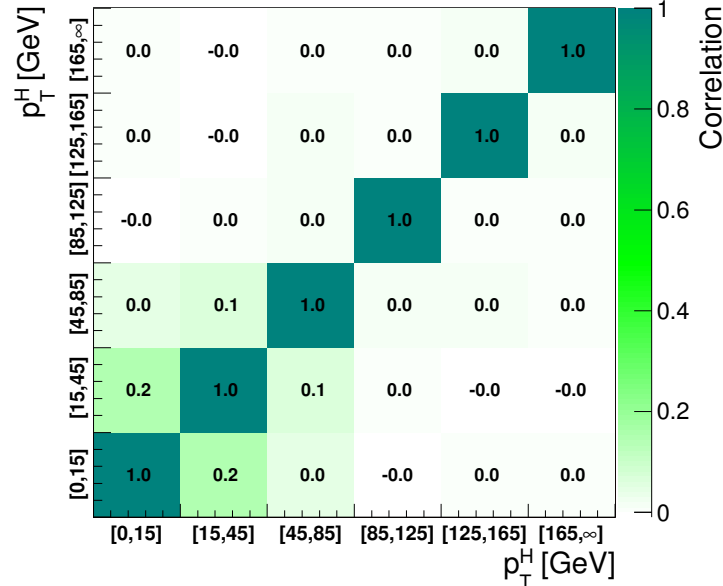


Figure 4.26.: Correlations among the signal strengths corresponding to the six p_T^H bins including all type A uncertainties.

1691 The nuisance parameters falling in the type B class are:

- 1692 • the b veto scale factor. It affects the signal and background templates by varying the
1693 number of events with jets that enter the selection. It also affects the response matrix

because the reconstructed spectrum is harder or softer depending on the number of jets, which in turn depends on the veto.

- the lepton efficiency scale factor. It affects the signal and background template shape and normalization. It affects the response matrix by varying the reconstructed spectrum;
- the E_T^{miss} scale and resolution, which have an effect similar to the above;
- lepton scale and resolution. The effect is similar to the above;
- jet energy scale. It affects the signal and background template shape and normalization. It also affects the response matrix because, by varying the fraction of events with jets, the b veto can reject more or fewer events, thus making the reconstructed spectrum harder or softer.

The effect of each type B uncertainty is evaluated separately, since each one changes the response matrix in a different way. In order to evaluate their effect on the signal strengths parameters, two additional fits are performed, each time fixing the nuisance parameter value to ± 1 standard deviation with respect to its nominal value. The results of the fits are then compared to the results of the full fit obtained by floating all the nuisance parameters, thus determining the relative uncertainty on the signal strengths due to each nuisance parameter, as shown in Tab. 4.11. Using these uncertainties, the measured spectra for each type B source are built. The effects are propagated through the unfolding by building the corresponding variations of the response matrix and unfolding the measured spectra with the appropriate matrix.

Type C uncertainties are related to the underlying assumption on the Higgs boson production mechanism used to extract the fiducial cross sections. These are evaluated using alternative response matrices that are obtained by varying the relative fraction of the VBF and ggH components within the experimental uncertainty, as given by the CMS combined measurement [83]. Three different response matrices are built, corresponding to the nominal, scaled up, and scaled down VBF/ggH ratio. The nominal matrix assumes the SM VBF/ggH ratio, while up- and down-scaled matrices are constructed by varying the SM signal strengths within the experimental constraints for VBF and ggH in such a way as to obtain the maximal variation of the VBF/ggH ratio allowed by the experimental constraints. These three matrices are used to unfold the reconstructed spectrum with the nominal VBF/ggH fraction, and obtain an uncertainty on the unfolded spectrum.

4.8. Results

In order to unfold the spectrum, the procedure described in section 4.7 has been pursued. The statistical plus type A systematic uncertainties are propagated by the unfolding procedure into the final spectrum, taking into account the signal strengths covariance matrix. The type B systematic uncertainty has been propagated using the following procedure: for each p_T^H bin, we compute the upper bound of the systematic band computing

Table 4.11.: Effect of all the Type B uncertainties on the signal strengths of each bin. In the table are reported the signal strength variations corresponding to an up or down scaling of each nuisance.

Type B uncertainty	Effect on signal strength ($+1\sigma/-1\sigma$ [%])					
	[0–15]	[15–45]	[45–85]	[85–125]	[125–165]	[165– ∞]
b veto	-10.1/-8.8	7.3/12.2	-6.3/3.1	-14.4/-4.8	-5.4/14.5	-7.9/17.8
lepton efficiency	-14.7/-3.9	4.5/15.1	-5.7/2.5	-13.2/-5.3	-0.2/7.6	-0.1/6.8
E_T^{miss} resolution	-12.5/0.0	15.4/-0.0	-12.8/-0.0	8.7/0.0	-20.9/-0.0	10.5/0.0
E_T^{miss} scale	-14.4/-6.8	-0.0/17.7	-6.1/-7.1	9.6/-20.9	2.3/32.4	2.5/2.6
lepton resolution	-12.5/-0.0	11.2/0.0	-2.4/0.0	-13.4/-0.0	9.9/0.0	-4.6/-0.0
electron momentum scale	-2.7/-13.1	15.9/9.9	10.8/-16.8	16.2/-33.1	30.9/-14.4	12.6/-10.9
muon momentum scale	-7.0/-10.7	11.8/8.9	1.1/-8.7	-0.7/-14.4	14.5/-4.6	8.0/-1.6
jet energy scale	-10.9/-10.1	9.0/9.0	-3.0/-2.9	-10.3/-8.9	0.3/3.4	5.2/3.1

Table 4.12.: Differential cross section in each p_T^H bin, together with the total uncertainty and the separate components of the various sources of uncertainty.

p_T^H [GeV]	$d\sigma/dp_T^H$ [fb/GeV]	Total uncertainty [fb/GeV]	Statistical uncertainty [fb/GeV]	Type A uncertainty [fb/GeV]	Type B uncertainty [fb/GeV]	Type C uncertainty [fb/GeV]
0–15	0.615	+0.370/-0.307	± 0.246	± 0.179	+0.211/-0.038	+0.0782/-0.0608
15–45	0.561	+0.210/-0.157	± 0.120	± 0.093	+0.146/-0.041	+0.0395/-0.0327
45–85	0.215	+0.084/-0.078	± 0.059	± 0.037	+0.047/-0.034	+0.0089/-0.0084
85–125	0.071	+0.038/-0.038	± 0.029	± 0.017	+0.018/-0.017	+0.0018/-0.0022
125–165	0.027	+0.020/-0.019	± 0.016	± 0.009	+0.007/-0.007	+0.0003/-0.0006
165– ∞	0.028	+0.027/-0.027	± 0.023	± 0.012	+0.008/-0.007	+0.0002/-0.0006

the square sum of all the signal strength variations that deviate in the up direction with respect to the bin central value, whether or not this variation corresponds to the up or down shift of the systematic uncertainty. The same is done for the lower bound of the systematic band. If both the up and down shifts of a given nuisance parameter lead to a same direction variation of the signal strength, only the larger variation is considered.

The unfolded p_T^H spectrum is shown in Fig. 4.27. Statistical, systematic, and theoretical uncertainties are shown as separate error bands in the plot. The unfolded spectrum is compared with the SM-based theoretical predictions where the ggH contribution is modelled using the HRES and POWHEG V2 programs. The comparison shows good agreement between data and theoretical predictions within the uncertainties. The measured values for the differential cross section in each bin of p_T^H are reported together with the total uncertainty in Table 4.12.

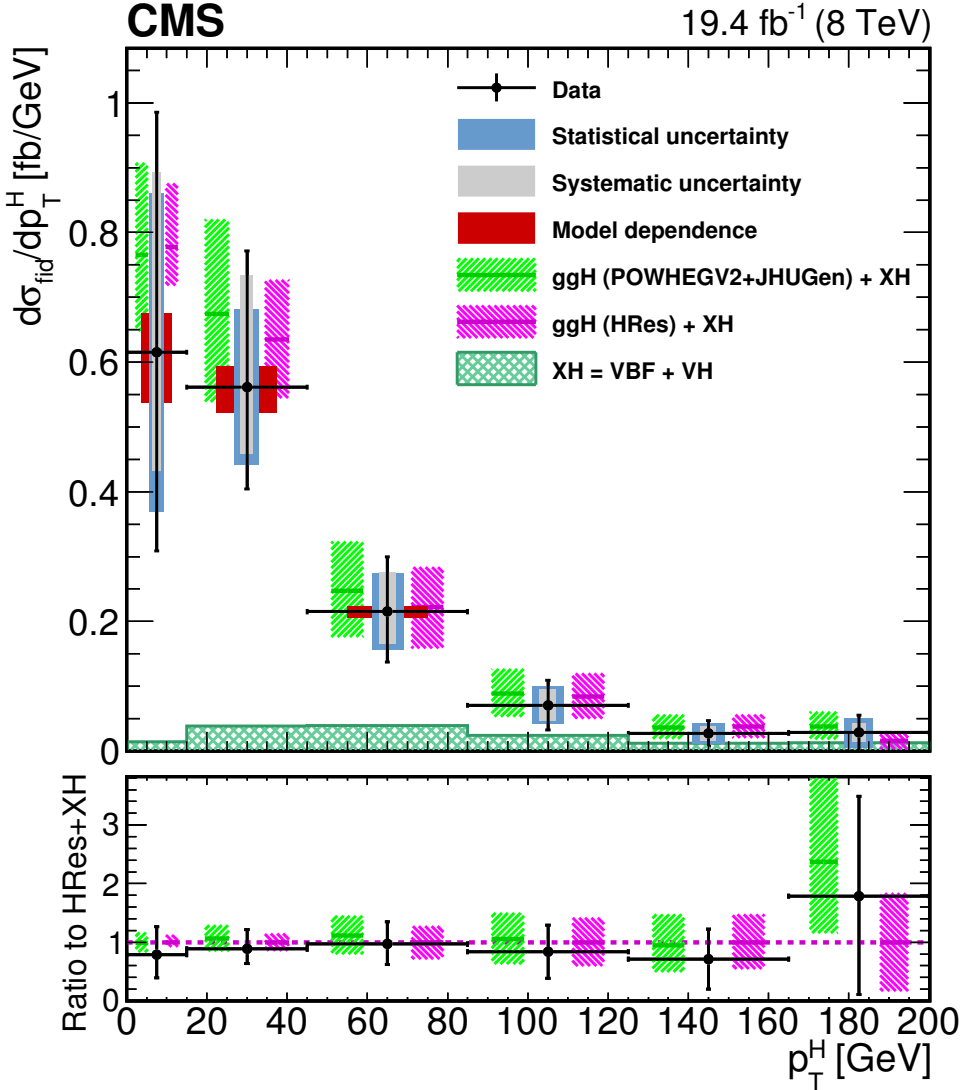


Figure 4.27.: Higgs boson production cross section as a function of p_T^H , after applying the unfolding procedure. Data points are shown, together with statistical and systematic uncertainties. The vertical bars on the data points correspond to the sum in quadrature of the statistical and systematic uncertainties. The model dependence uncertainty is also shown. The pink (and back-sashed filling) and green (and slashed filling) lines and areas represent the SM theoretical estimates in which the acceptance of the dominant ggH contribution is modelled by HRes and POWHEG V2, respectively. The subdominant component of the signal is denoted as $\text{XH}=\text{VBF}+\text{VH}$ and it is shown with the cross filled area separately. The bottom panel shows the ratio of data and POWHEG V2 theoretical estimate to the HRes theoretical prediction.

1744 Figure 4.28 shows the correlation matrix for the six bins of the differential spectrum.
 1745 The correlation of of bins is defined as in Eq. (4.31).

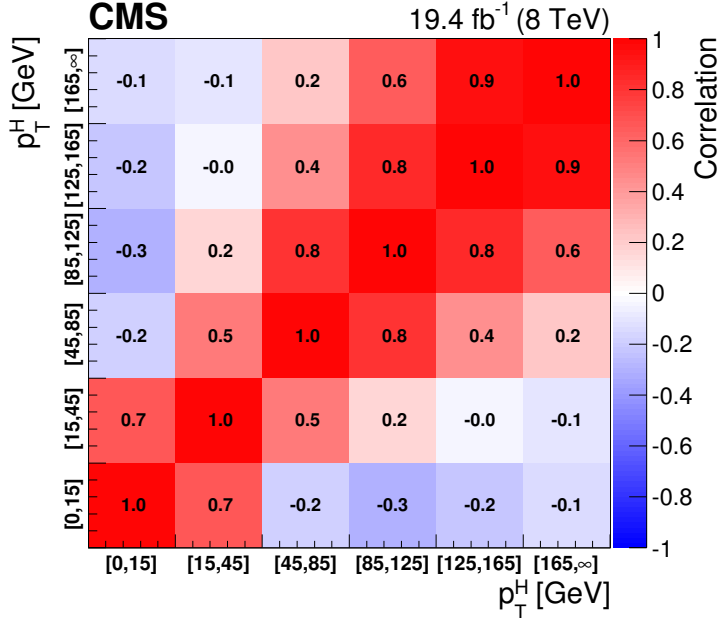


Figure 4.28.: Correlation matrix among the p_T^H bins of the differential spectrum.

To measure the inclusive cross section in the fiducial phase space, the differential measured spectrum is integrated over p_T^H . In order to compute the contributions of the bin uncertainties of the differential spectrum to the inclusive uncertainty, error propagation is performed taking into account the covariance matrix of the six signal strengths. For the extrapolation of this result to the fiducial phase space, the unfolding procedure is not needed, and the inclusive measurement has only to be corrected for the fiducial phase space selection efficiency ϵ_{fid} . Dividing the measured number of events by the integrated luminosity and correcting for the overall selection efficiency, which is estimated in simulation to be $\epsilon_{\text{fid}} = 36.2\%$, the inclusive fiducial $\sigma \times \mathcal{B}$, σ_{fid} , is computed to be:

$$\sigma_{\text{fid}} = 39 \pm 8 \text{ (stat)} \pm 9 \text{ (syst)} \text{ fb} \quad , \quad (4.32)$$

in agreement within the uncertainties with the theoretical estimate of 48 ± 8 fb, computed integrating the spectrum obtained with the POWHEG V2 program for the ggH process and including the XH contribution.

Chapter 5.

1758 **Search for the SM Higgs boson in the 1759 **H → WW channel with the first 1760 **13 TeV LHC data******

1761 **5.1. Introduction**

1762 In this chapter, the first search for the SM Higgs boson decaying to a W boson pair at
1763 13 TeV is presented, using a total integrated luminosity of 2.3 fb^{-1} , collected during the
1764 2015 proton proton data taking period of the LHC.

1765 Final states in which the two W bosons decay leptonically are studied. Therefore,
1766 events with a pair of oppositely-charged leptons, exactly one electron and one muon, a
1767 substantial amount of missing transverse energy, E_T^{miss} , due to the presence of neutrinos in
1768 the final state, and either zero or one jet are selected. This signature is common to other
1769 processes, which enter the analysis as backgrounds. The main background comes from
1770 WW production, irreducible background that shares the same final states and can only be
1771 separated by the use of certain kinematic properties. Another important background is
1772 W+jets, where a jet can mimick a leptonic signature. Background coming from top quark
1773 events, i.e. $t\bar{t}$ and single top production, is also important, followed by other processes such
1774 as Drell-Yan, WZ, and other EWK production. The analysis strategy follows the one used
1775 during Run 1 in the same channel, described in Chapter 4, with a few different aspects that
1776 are described in the next sections.

1777 With respect to 8 TeV, the ggH production cross section at 13 TeV is expected to
1778 increase of a factor of 2, thus raising the number of expected signal events. In addition, the
1779 cross section for the background processes is increasing as well. The WW production cross
1780 section increases of a factor of 1.8 and the $t\bar{t}$ cross section of a factor of 3.5, due to the
1781 enhancement of the gluon PDFs at higher center of mass energies.

1782 **5.2. Data and simulated samples**

1783 Data recorded in proton proton collisions at 13 TeV during 2015 was used in the analysis,
1784 with a total integrated luminosity of 2.3 fb^{-1} . Single and double lepton triggers are used

1785 similarly to the same analysis at 8 TeV. The HLT paths and descriptions of the triggers used
1786 in this analysis are described in Tables 5.1 and 5.2 for electrons and muons respectively.

Table 5.1.: HLT paths related to Electrons

HLT Path	Description
HLT_Ele23_WPLoose_Gsf_v*	Single Electron trigger. Best trigger to be used for 2015 data. In WW , we are using “Trigger safe” Id. Turn on is at around $\text{Ele } p_T = 30 \text{ GeV}$
HLT_Ele17_Ele12_CaloIdL_TrackIdL_IsoVL_DZ_v*	Double Electron Trigger. Best trigger to cover the turn on region from single electron trigger. “DZ” filter is also present. Its efficiency is also calculated separately.
HLT_Ele12_CaloIdL_TrackIdL_IsoVL_v*	This electron leg of HLT_Mu17_TrkIsoVVL_Ele12_CaloIdL_TrackIdL_IsoVL_v* same as Ele12 leg of double electron trigger.
HLT_Ele17_CaloIdL_TrackIdL_IsoVL_v*	This electron leg of HLT_Mu8_TrkIsoVVL_Ele17_CaloIdL_TrackIdL_IsoVL_v* same as Ele17 leg of double electron trigger.

1787 The trigger efficiencies are measured in data and applied on simulated events as described
1788 in Sec. 4.2.1.

1789 Concerning the simulated samples, several different Monte Carlo (MC) generators were
1790 used. In the simulation, ‘lepton’ includes also τ . Higgs signal samples have been simulated
1791 in all channels with POWHEG v2 [44, 57, 84], designed to describe the full NLO properties
1792 of these processes. In particular, for Higgs produced via gluon fusion [46], and vector-boson-
1793 fusion (VBF) [47], the decay of the Higgs boson into two W boson and subsequently into
1794 leptons was done using JHUGEN v5.2.5 [85]. For associated production with a vector boson
1795 (W^+H , W^-H , ZH) [86], including gluon fusion produced ZH ($ggZH$), the Higgs decay was
1796 done via PYTHIA 8.1 [66]. Alternative signal samples were produced with AMC@NLO [49],
1797 or with POWHEG v2 but decayed via PYTHIA 8.1 for gluon fusion and VBF assuming a
1798 Higgs boson mass of 125 GeV. In the following, the mass of the SM Higgs boson is assumed
1799 to be 125 GeV.

1800 The WW production, irreducible background for the analysis, was simulated in different
1801 ways. POWHEG v2 [87] was used for $q\bar{q}$ produced WW in different decays. The cross
1802 section used for normalizing WW processes produced via $q\bar{q}$ was computed at next-to-next-
1803 to-leading order (NNLO) [88]. In order to control the top quark background processes, the
1804 analysis is performed with events that have no more than one high- p_T jet. The veto on
1805 high- p_T jets enhances the importance of logarithms of the jet p_T , spoiling the convergence
1806 of fixed-order calculations of the $q\bar{q} \rightarrow WW$ process and requiring the use of dedicated
1807 resummation techniques for an accurate prediction of differential distributions [89, 90]. The
1808 p_T of the jets produced in association with the WW system is strongly correlated with its
1809 transverse momentum, p_T^{WW} , especially in the case where only one jet is produced. The

Table 5.2.: Muon trigger's elements description

HLT path	
HLT_IsoMu18_v*	single muon trigger
HLT_IsoTrMu20_v*	single muon trigger with tracker isolation
HLT_Mu17_TrkIsoVVL	leg for the HLT_Mu17_TrkIsoVVL_Mu8_TrkIsoVVL_DZ_v*, HLT_Mu17_TrkIsoVVL_TkMu8_TrkIsoVVL_DZ_v* and HLT_Mu17_TrkIsoVVL_Ele12_CaloIdL_TrackIdL_IsoVL_v* double lepton triggers
HLT_Mu8_TrkIsoVVL	leg for the HLT_Mu17_TrkIsoVVL_Mu8_TrkIsoVVL_DZ_v* and HLT_Mu8_TrkIsoVVL_Ele17_CaloIdL_TrackIdL_IsoVL_v* double lepton triggers
HLT_TkMu8_TrkIsoVVL	leg for the HLT_Mu17_TrkIsoVVL_TkMu8_TrkIsoVVL_DZ_v* double muon trigger
$DZ_{\mu\mu}$	efficiency of DZ cut in the HLT_Mu17_TrkIsoVVL_Mu8_TrkIsoVVL_DZ_v* and HLT_Mu17_TrkIsoVVL_TkMu8_TrkIsoVVL_DZ_v* double muon triggers, it is around 95%

- 1810 simulated $q\bar{q} \rightarrow WW$ events are reweighted to reproduce the p_T^{WW} distribution from the
 1811 p_T -resummed calculation.
 1812 Gluon fusion produced WW was generated, with and without Higgs diagrams, using
 1813 MCFM v7.0 [91]. A $t\bar{t}$ sample dilepton sample was also generated using POWHEG v2. The
 1814 WW and $t\bar{t}$ samples produced specifically for this analysis are presented in Table 5.3. Other
 1815 background samples are used, a list of the most relevant ones is presented in Table 5.4.

Table 5.3.: Simulated samples for $t\bar{t}$ and WW production. The $gg \rightarrow WW \rightarrow 2\ell 2\nu$ (H diagr.) sample includes both ggH production, the $ggWW$ component and the interference.

Process	$\sigma \times \mathcal{B}$ [pb]
$t\bar{t} \rightarrow WW b\bar{b} \rightarrow 2\ell 2\nu b\bar{b}$	87.31
$q\bar{q} \rightarrow WW \rightarrow 2\ell 2\nu$	12.178
$gg \rightarrow WW \rightarrow 2\ell 2\nu$	0.5905
$gg \rightarrow WW \rightarrow 2\ell 2\nu$ (H diagr.)	0.9544

- 1816 All processes are generated using the NNPDF2.3 [92, 93] parton distribution functions
 1817 (PDF) for NLO generators, while the LO version of the same PDF is used for LO generators.
 1818 All the event generators are interfaced to PYTHIA 8.1 [66] for the showering of partons

Table 5.4.: Simulated samples for other backgrounds used in the analysis.

Process	$\sigma \times \mathcal{B}$ [pb]
Single top	71.7
Drell-Yan ($10 \text{ GeV} < m_{\ell\ell} < 50 \text{ GeV}$)	20471.0
Drell-Yan ($m_{\ell\ell} > 50 \text{ GeV}$)	6025.26
$WZ \rightarrow 2\ell 2q$	5.5950
$ZZ \rightarrow 2\ell 2q$	3.2210
WWZ	0.1651
WZZ	0.05565
ZZZ	0.01398

and hadronization, as well as including a simulation of the underlying event (UE) and multiple interaction (MPI) based on the CUET8PM1 tune [94]. To estimate the systematic uncertainties related to the choice of UE and MPI tune, the signal processes and the WW events are also generated with two alternative tunes which are representative of the errors on the tuning parameters. The showering and hadronization systematic uncertainty is estimated by interfacing the same MC samples with the HERWIG ++ 2.7 parton shower [95, 96]. For all processes, the detector response is simulated using a detailed description of the CMS detector, based on the GEANT4 package [58].

The simulated samples are generated with distributions for the number of pileup interactions that are meant to roughly cover, though not exactly match, the conditions expected for the different data-taking periods. In order to factorize these effects, the number of true pileup interactions from the simulation truth is reweighted to match the data. The re-weighting is propagated automatically to both the in-time pile up and the out-of-time one. In Fig. 5.1, the effect of this reweighting on a sample enriched in Drell-Yan events is shown. Before the reweighting the simulation is presented in the open red histogram; after the reweighting, it is represented by the solid green histogram that matched well the data. In order to select this sample, events with two leptons with $p_T > 20 \text{ GeV}$, opposite sign, and same flavour, are selected only if $|m_{\ell\ell} - m_Z| < 15 \text{ GeV}$.

The average number of pileup is approximately 11.5.

Different sources and calculations are used to obtain the cross sections for the different processes at 13 TeV. For Higgs signal, the cross sections used are the ones reported by the LHC Higgs Cross Section Working Group [97], computed at NNLO and NNLL QCD and NLO EW for gluon fusion, and at NNLO QCD and NLO EW for the rest of the production modes. The branching fractions are the ones reported in Ref. [40].

The cross section used for normalizing $q\bar{q}$ produced WW processes was computed at next-to-next-to-leading order (NNLO) [88]. The leading-order (LO) cross section for $ggWW$ is obtained directly from MCFM. For gluon fusion, the difference between LO and NNLO cross sections is significantly big. A scale factor of 1.4 is theoretically calculated [98]. For

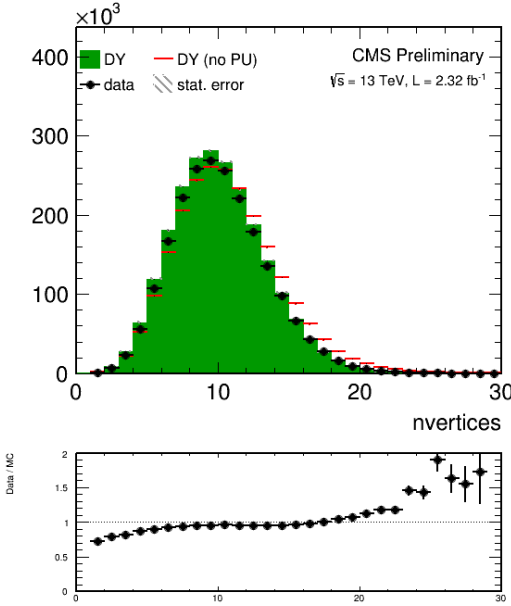


Figure 5.1.: Distributions of the number of vertices in a Drell-Yan enriched sample in data, together with the simulation before (red) and after (solid green) the pileup reweighting.

the LO simulation of the interference between $gg \rightarrow WW$ and gluon fusion produced $H \rightarrow WW$ a k-factor of 1.87 is applied. This k-factor is obtained as the average between LO to NNLO ggH scale factor and LO to NLO $ggWW$ scale factor.

The cross sections of the different single top processes are estimated by the LHC Top Working group [99] at NLO. The $t\bar{t}$ cross section is also provided by the LHC Top Working group [100], and it is computed at NNLO, with NNLL soft gluon resummation.

Drell-Yan (DY) production of Z/γ^* is generated using AMC@NLO [49]. Other multi-boson processes, such as WZ, ZZ , and VVV ($V=W/Z$), are generated with AMC@NLO and normalized to the cross section obtained at NLO in generation.

All processes are generated using the NNPDF2.3 [92, 93] parton distribution functions (PDF) for NLO generators, while the LO version of the same PDF is used for LO generators. All the event generators are interfaced to PYTHIA 8.1 for the showering of partons and hadronization, as well as including a simulation of the underlying event (UE) and multiple interaction (MPI) based on the CUET8PM1 tune [94].

1861 5.3. Analysis strategy

1862 5.3.1. Event reconstruction

1863 Regarding the electrons, muons, jets and E_T^{miss} definition and reconstruction, the standard
 1864 CMS recommendations described in Chapter 2 are used. The specific selections used in
 1865 this analysis are briefly summarised below.

1866 Muons are identified according to the CMS recommendations for the medium working
 1867 point, with the addition of some extra cuts, as defined by the following selections:

- 1868 • identified by the standard medium muon selection described in Sec. 2.4; **Not yet**
 1869 **defined :)**
- 1870 • $p_T > 10 \text{ GeV}$;
- 1871 • $|\eta| < 2.4$;
- 1872 • $|d_{xy}| < 0.01 \text{ cm}$ for $p_T < 20 \text{ GeV}$ and $|d_{xy}| < 0.02 \text{ cm}$ for $p_T > 20 \text{ GeV}$, d_{xy} being the
 1873 transverse impact parameter with respect to the primary vertex;
- 1874 • $|d_z| < 0.1 \text{ cm}$, where d_z is the longitudinal distance of the muon track in the tracker
 1875 extrapolated along the beam direction.

1876 For the muon isolation, the CMS recommended particle flow isolation based on the
 1877 tight working point is used, corresponding to a requirement on the isolation variable of
 1878 $ISO_{\text{tight}} < 0.15$. In addition a tracker relative isolation is also applied.

1879 For the electron identification, the tight working point is used. In addition some
 1880 additional cuts to make the selection “trigger-safe” are included. This is done because the
 1881 electron triggers already include some identification and isolation requirements that are
 1882 based on the raw detector information, while the offline selections make use of particle flow
 1883 requirements. The “trigger-safe” selections are defined to make the the offline identification
 1884 and isolation requirements tighter with respect to the online triggers.

1885 The simulated events are corrected for the lepton trigger, identification and isolation
 1886 efficiencies measured in data using the same techniques described in Sec. 4.3.1.

1887 Jets are defined clustering the particle flow objects using the anti- k_t algorithm with a
 1888 distance parameter of 0.4. The CHS pileup mitigation technique is used. The L1, L2, L3
 1889 and L2L3 jet energy correction described in Sec. 2.4 are applied. The reject jets coming from
 1890 calorimeter or readout electronics noise, the loose working point for PF jet identification is
 1891 used.

1892 The b-tagging algorithm for this analysis is chosen comparing the performances of
 1893 different algorithms using simulations for signal and background contributions in the phase
 1894 space defined by the analysis kinematic requirements. More precisely, two MC samples are
 1895 used, one corresponding the the $H \rightarrow WW \rightarrow 2\ell 2\nu$ signal produced via the ggH production
 1896 mode and another corresponding to the $t\bar{t}$ process. In fact, the first sample is enriched
 1897 in light jets, i.e. originating by the hadronization of light quarks like u,d,c and s quarks,
 1898 while the second sample is enriched in b jets, coming from the top quark decay. The b-veto
 1899 efficiency, ϵ_{bveto} , is computed separately for the two samples and for the various b tagging

algorithms. To compare the b tagging performance $\epsilon_{b\text{veto}}$ is computed for different working points, i.e. different selections on the specific b tagging discriminator, and the results are reported in the form of a ROC curve. The ROC curves corresponding to events with 0, 1 and ≥ 2 jets are shown in Fig. 5.2. Events considered for this study are the ones passing the WW baseline selection.

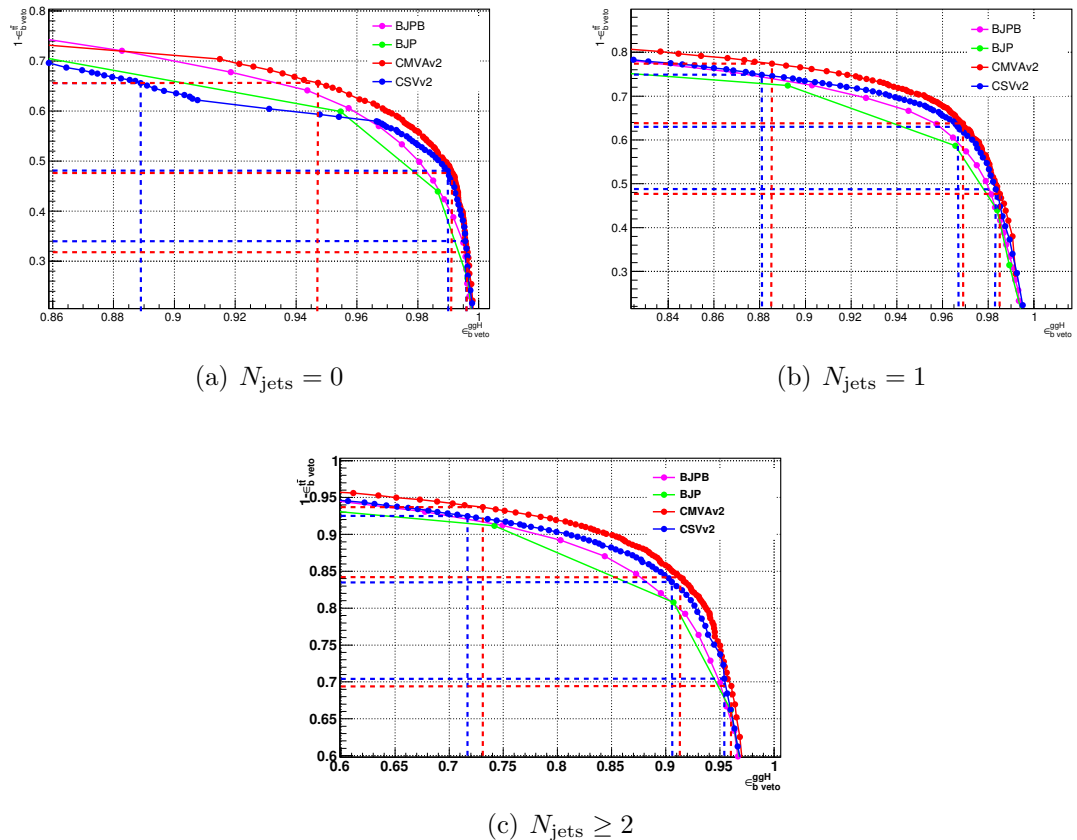


Figure 5.2.: ROC curve for the b veto efficiency on signal and background events. The blue and red lines point out the signal efficiency and the background rejection corresponding to the three working points considered for the CSVv2 and the cMVAv2 algorithms respectively.

The ROC curves show that the cMVAv2 algorithm has the best performance for the analysis phase space among the algorithms taken into account. For both the CSVv2 and cMVAv2 algorithms, three working points are defined corresponding to the mistag rates¹ of 10% for the loose, 1% for the medium and 0.1% for the tight working point. The distribution of the cMVAv2 discriminator associated to the leading jet both for the ggH and the t̄t MC sample is shown in figure 5.3.

¹The mistag rate is defined as the probability for a light jet to be identified as a b-jet by the b tagging algorithms.

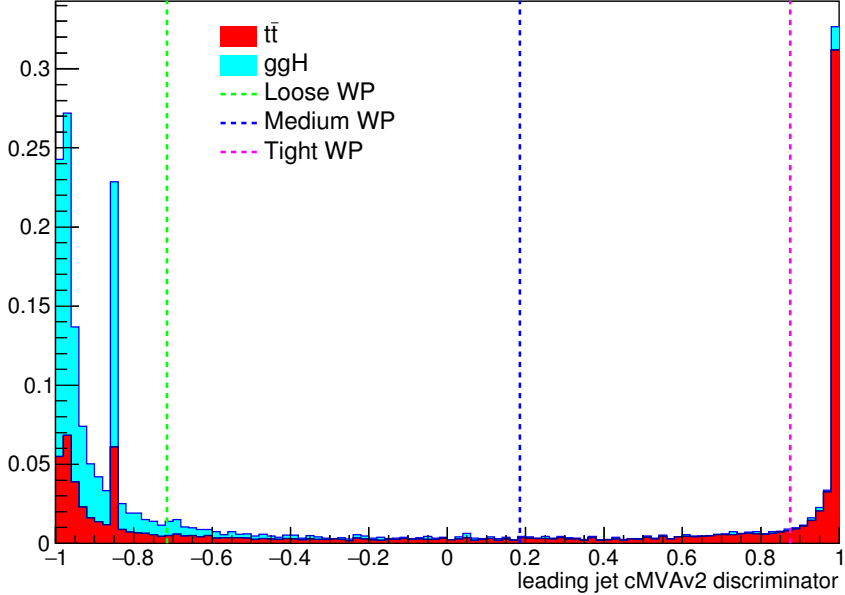


Figure 5.3.: cMVAv2 discriminator associated to the leading jet (with $p_T > 30$ GeV) both for the ggH and the $t\bar{t}$ processes. The two processes are normalized to unity and stacked. The vertical dashed lines show the discriminator value corresponding to the three working points.

In order to determine the best working point for this analysis a preliminary significance assessment is performed, using a complete analysis procedure in which only statistical effects are taken into account (no systematics are included). The significance assessment was performed using a two dimensional discriminating variable consisting of the dilepton invariant mass versus the transverse mass. The assessment was performed with the following leptonic selection:

- two leptons, an electron and a muon with opposite charge, with leading lepton p_T greater than 20 GeV and sub-leading lepton p_T greater than 13 GeV;
- no other lepton (electron or muon) with p_T greater than 10 GeV;
- $m_{\ell\ell}$ greater than 12 GeV;
- PF type 1 corrected MET greater than 20 GeV;
- $p_T^{\ell\ell}$ greater than 30 GeV.

In addition to this global selection, two categories were identified:

- 0 jets: no jets above 30 GeV, jets between 20 GeV and 30 GeV are b-vetoed with the cMVAv2 WP under study;
- 1 jet: exactly 1 jet above 30 GeV, no b-tagged jets above 30 GeV according to the cMVAv2 WP under study.

Table 5.5.: Significance corresponding to the three working points and for different jet categories using a shape analysis.

Jet category	Loose WP (-0.715)	Medium WP (0.185)	Tight WP (0.875)
0 jets	2.022	2.043	2.036
1 jet	1.439	1.404	1.305
0 + 1 jets	2.481	2.479	2.420

1928 The two categories were eventually combined together and the significance assessment was
 1929 repeated for the three working points. With these selection we find the significance values
 1930 listed in Table 5.5 for the three working points.

1931 The working point providing the best significance in the combined 0 + 1 jets category is
 1932 found to be the loose one.

1933 To correct for a possible different b tagging efficiency in data and simulation, the
 1934 simulated events are reweighted using scale factors computed in bins of the jet η and p_T .
 1935 These scale factors and the corresponding uncertainties are centrally calculated for each
 1936 working point, in such a way to be employable by all the CMS analyses. The prescription
 1937 to reweight the simulated events is the following. First of all one has to compute the b
 1938 tagging efficiency using the MC samples, $\varepsilon_{\text{MC}}(p_T, \eta, f)$, for the chosen working point in bins
 1939 of jet p_T and η . The efficiency has to be computed for different flavours f of the jets, b,
 1940 c and light (u,d,s), using the jet matching information² which is available in all the MC
 1941 samples. An MC-based event weight is then calculated computing the probability P_{MC} of a
 1942 given b tagging configuration to occur, e.g.:

$$P_{\text{MC}} = \prod_{i \in \text{b-tagged-jets}} \varepsilon_{\text{MC}_i} \prod_{j \in \text{non-b-tagged-jets}} (1 - \varepsilon_{\text{MC}_j}) \quad (5.1)$$

1943 Afterwards, a similar probability is computed using data:

$$P_{\text{DATA}} = \prod_{i \in \text{b-tagged-jets}} SF_i \varepsilon_{\text{MC}_i} \prod_{j \in \text{non-b-tagged-jets}} (1 - SF_j \varepsilon_{\text{MC}_j}) , \quad (5.2)$$

1944 where SF_i is the provided scale factor value for the relevant jet flavour, p_T and η . Products
 1945 in Eqs. 5.1 and 5.2 run over all jets. The event weight is finally given by the ration
 1946 $P_{\text{DATA}}/P_{\text{MC}}$.

1947 The b tagging efficiencies to be fed into Eq. 5.1 and Eq. 5.2 are derived using $t\bar{t}$ simulated
 1948 events and applying basic leptonic selections. These efficiencies are shown in Fig. 5.4 for

²There are a couple of techniques developed by the CMS Collaboration to assess the flavour of a reconstructed jet in simulation. The technique used here makes use of the flavour of the hadrons clustered into a jet.

1949 light (a), c-jets (b) and b-jets (c), in bins of η and p_T . The uncertainties associated to the
 1950 efficiencies are representative of the statistics of the simulated $t\bar{t}$ sample, and are computed according to a binomial distribution.

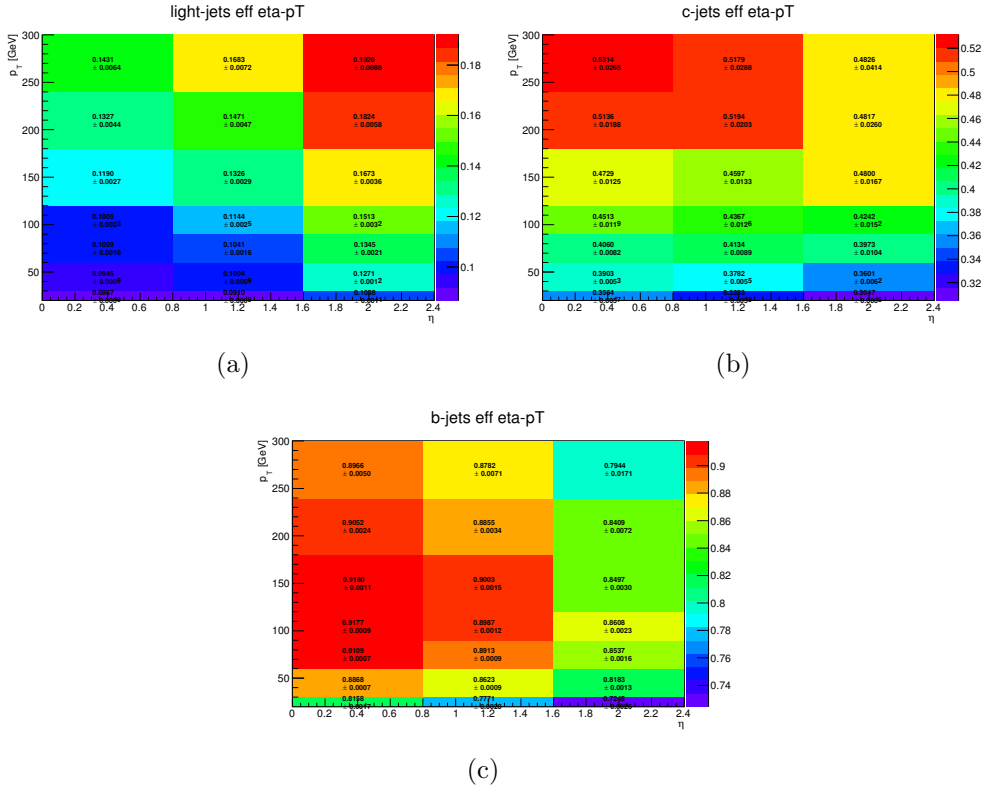


Figure 5.4.: B tagging efficiencies for light jets (a), c-jets (b) and b jets (c), as a function of η and p_T .

1951
 1952 The effect of the event reweighting is to correct the shape of the b tagging discriminator
 1953 in simulation, moving events from the b tag region (discriminator greater than > -0.715)
 1954 to the b veto region (discriminator < -0.715) and viceversa. A data/simulation comparison
 1955 of the b tagging discriminator for the leading and subleading jets is performed to check the
 1956 agreement after the application of the event weights. In order to evaluate the data/simulation
 1957 agreement for b-jets, the data and simulation are compared in a top enriched control region,
 1958 defined by the following requirements:

- 1959 • two leptons, an electron and a muon with opposite charge, with leading lepton p_T
 1960 greater than 20 GeV and sub-leading lepton p_T greater than 15 GeV;
- 1961 • no other lepton (electron or muon) with p_T greater than 10 GeV;
- 1962 • lepton invariant mass greater than 50 GeV;
- 1963 • at least two jets with p_T greater than 30 GeV;

- at least one of the two leading jets with cMVAv2 btagging score greater than -0.715 (i.e. the loose working point).

In order to evaluate the agreement for light jets, a second control region is defined, populated by Z+light jet events, defined as follows:

- two leptons, two electrons or two muons with opposite charge, with leading lepton p_T greater than 20 GeV and sub-leading lepton p_T greater than 15 GeV.
- no other lepton (electron or muon) with p_T greater than 10 GeV.
- lepton invariant mass greater between 80 GeV and 110 GeV.
- at least two jets with p_T greater than 30 GeV.
- at least one jet above 30 GeV.
- no jets above 20 GeV with a TCHE score above 2.1.

Although a Z+jets sample is dominated by light flavor jets, a b-veto on an alternative algorithm (TCHE) is applied to reduce the contamination from b-jets, especially above the cMVAv2 cut. This helps mitigating possible data/simulation discrepancies in the modeling of the heavy/light flavour ratio. The comparison between data and simulation after the event reweighting is shown in Figs. 5.5 and 5.6 for the b-jets and light jets enriched control regions, respectively.

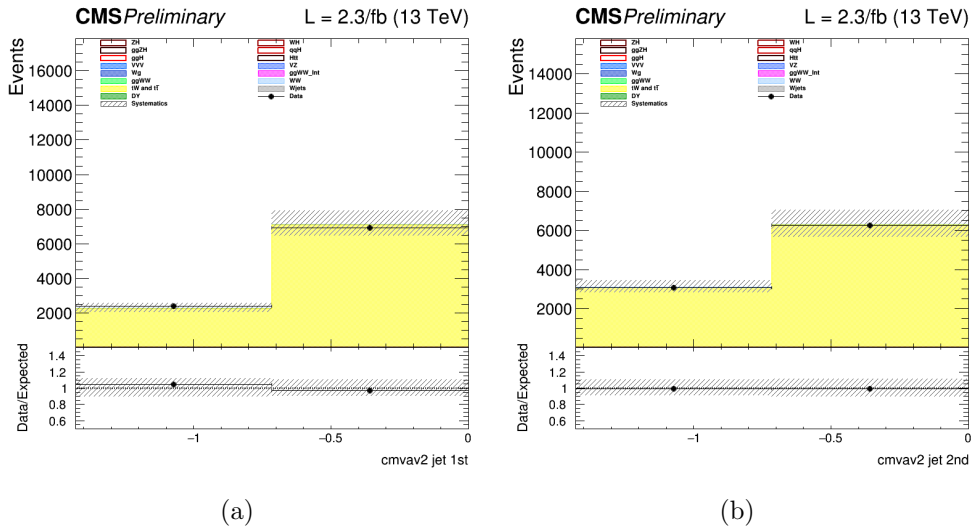


Figure 5.5.: B tagging cMVAv2 discriminator for the leading (a) and the subleading (b) jet in the b-jets enriched control region.

5.3.2. Event selection and background rejection

Since the ggH production mechanism, which is the main production mode for a Higgs mass of around 125 GeV, is characterized by the emission of few jets arising from initial

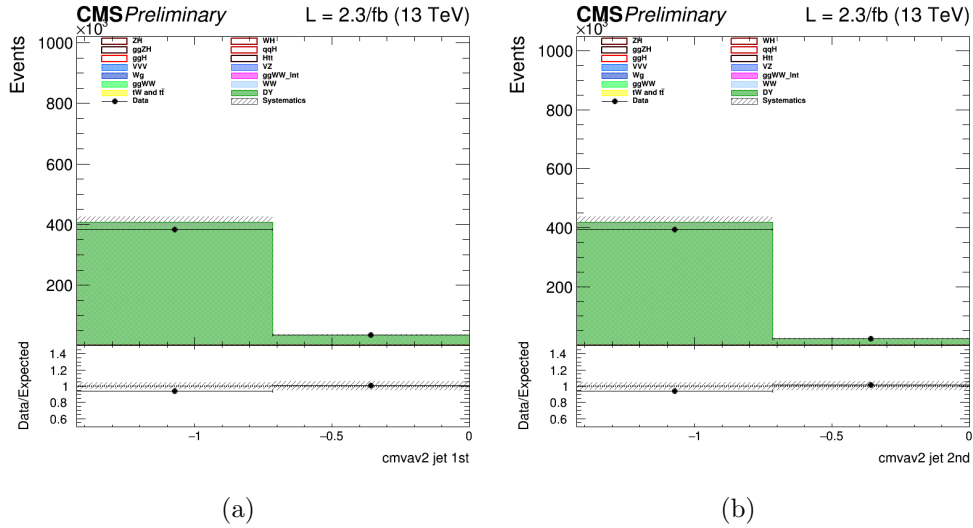


Figure 5.6.: B tagging cMVAv2 discriminator for the leading (a) and the subleading (b) jet in the light jets enriched control region.

or final state radiation, this analysis is limited to events with no jets or one jet. Due to the large DY background in di-electrons and di-muons events, only the $e\mu$ final state is studied in this early Run 2 data analysis, including the indirect contribution from τ leptons decaying to electron or muons. Exactly one electron and one muon are required to be reconstructed in the event with opposite charges and a minimum p_T of 10 (13) GeV for the muon (electron). One of the two leptons should also have a p_T greater than 20 GeV and both leptons are required to be well identified and isolated to reject fake leptons and leptons coming from QCD sources. To suppress background processes with three or more leptons in the final state, such as ZZ, WZ, $Z\gamma$, $W\gamma$, or tri-boson production, no additional identified and isolated lepton with $p_T > 10$ GeV should be reconstructed. The low $m_{\ell\ell}$ region dominated by QCD production of leptons is not considered in the analysis and $m_{\ell\ell}$ is requested to be higher than 12 GeV. To suppress the background arising from DY events decaying to a τ lepton pair which subsequently decays to an $e\mu$ final state and suppress processes without genuine E_T^{miss} , a minimal E_T^{miss} of 20 GeV is required. The DY background is further reduced by requesting $p_T^{\ell\ell} > 30$ GeV. Finally the contribution from leptonic decays of single top and $t\bar{t}$ production is reduced by requesting that no jets with $p_T > 20$ GeV are identified by the b tagging algorithm as originating from a b quark in the event.

The requirements described above define the WW baseline selection. After those requirements the data sample is dominated by events arising from the non-resonant WW production and $t\bar{t}$ production. To further reduce the effect of these backgrounds on the signal sensitivity, the events are categorized depending on the jet multiplicity, counting jets with $p_T > 30$ GeV. Events with zero associated jets mainly arise from the WW production, while WW and $t\bar{t}$ productions have a similar contribution in the category with one jet.

2008 Higher jet multiplicity categories, which are sensitive to other Higgs production mechanisms,
 2009 such as VBF, are not included in this analysis, given the very low expected yield for other
 2010 production modes with the analysed integrated luminosity.

2011 Distributions of some variables of interest for the 0 and 1 jet categories separately,
 2012 but merging the $e\mu$ and μe final states together, are shown in Figs. 5.7, 5.8 and 5.9 after
 2013 applying the WW baseline selections, with the addition of a cut on $m_{\ell\ell}$ to remove the Higgs
 2014 signal contribution ($m_{\ell\ell} > 80$ GeV), and a cut on m_T to be orthogonal to the $Z\gamma^* \rightarrow \tau\tau$
 2015 background control region ($m_T > 60$ GeV).

2016 The $W+jets$ background, where one jet can be misidentified as a lepton, is a sub-
 2017 dominant background in the phase space defined by the analysis kinematic requirements.
 2018 The 0 ad 1 jets categories are further split according to the lepton flavour to $e\mu$ and μe ,
 2019 where the first lepton refers to the leading one. In this way an improvement of about 10% in
 2020 terms of the signal significance can be achieved, exploiting the different $W+jets$ background
 2021 contribution in the two categories. Indeed the probability for a jet to be misidentified as an
 2022 electron or a muon is not the same.

2023 5.3.3. Signal extraction

2024 To extract the Higgs boson signal contribution in the four previously mentioned categories,
 2025 a similar approach to the one used in the Run 1 analysis [41] is pursued. The analysis is
 2026 based on two-dimensional templates of $m_{\ell\ell}$ versus m_T to discriminate signal and background
 2027 contributions. The $m_{\ell\ell}$ template is defined using 5 bins from $m_{\ell\ell} = 10$ GeV up to $m_{\ell\ell} =$
 2028 110 GeV, while for the m_T template 7 bins are defined in the range 60 GeV $< m_T < 200$ GeV.
 2029 The phase space with $m_T < 60$ GeV is used as an orthogonal control region to extract the
 2030 normalization of the DY background. A binned maximum likelihood fit to the signal and
 2031 background two-dimensional templates is performed to extract the signal strength in the
 2032 four categories.

2033 Distributions of the $m_{\ell\ell}$ and m_T variables after the WW level selection are shown in
 2034 Fig. 5.10 for the 0 and 1 jet categories separately, but merging the $e\mu$ and μe final states
 2035 together.

2036 The statistical methodology used to interpret the data and to combine the results from
 2037 the independent 0-jet and 1-jet categories in the $e\mu$ and μe final states has been developed
 2038 by the ATLAS and CMS collaborations in the context of the LHC Higgs Combination
 2039 Group [83, 101]. The number of events in each category and in each bin of two-dimensional
 2040 template is modelled as a Poisson random variable, with a mean value given by the sum
 2041 of the contributions from all the processes under consideration. Systematic uncertainties
 2042 are represented by individual nuisance parameters with log-normal distributions. The
 2043 uncertainties affect the overall normalization of the signal and backgrounds as well as the
 2044 shape of the predictions across the distribution of the observables. Correlation between
 2045 systematic uncertainties in different categories are taken into account.

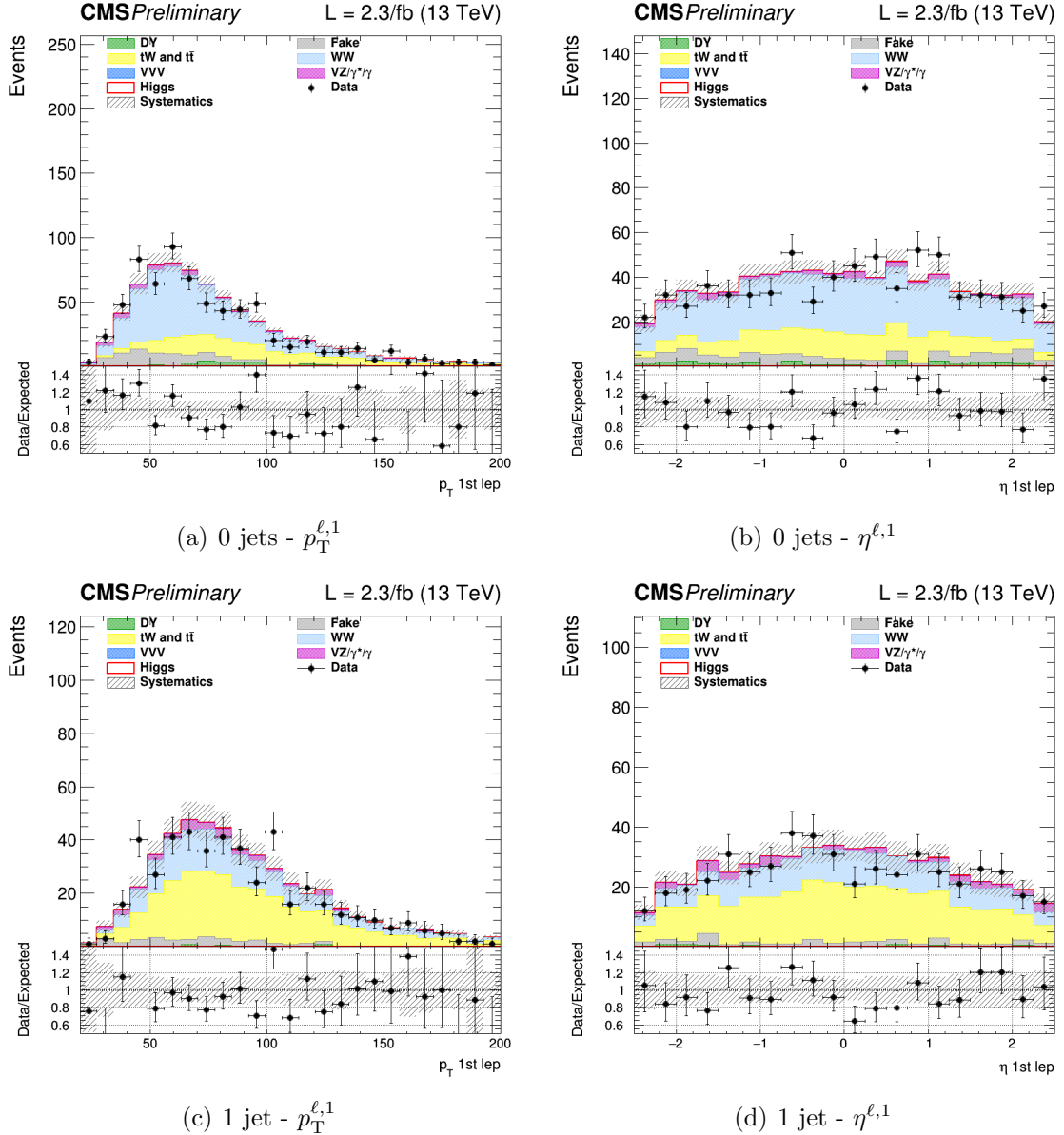


Figure 5.7.: Distributions of p_T (left) and η (right) of the leading lepton for events with 0 jet (upper row) and 1 jet (lower row), for the main backgrounds (stacked histograms), and for a SM Higgs boson signal with $m_H = 125$ GeV (superimposed and stacked red histogram) at the WW selection level. The last bin of the histograms includes overflows. The simulation of the WW background is normalized to data.

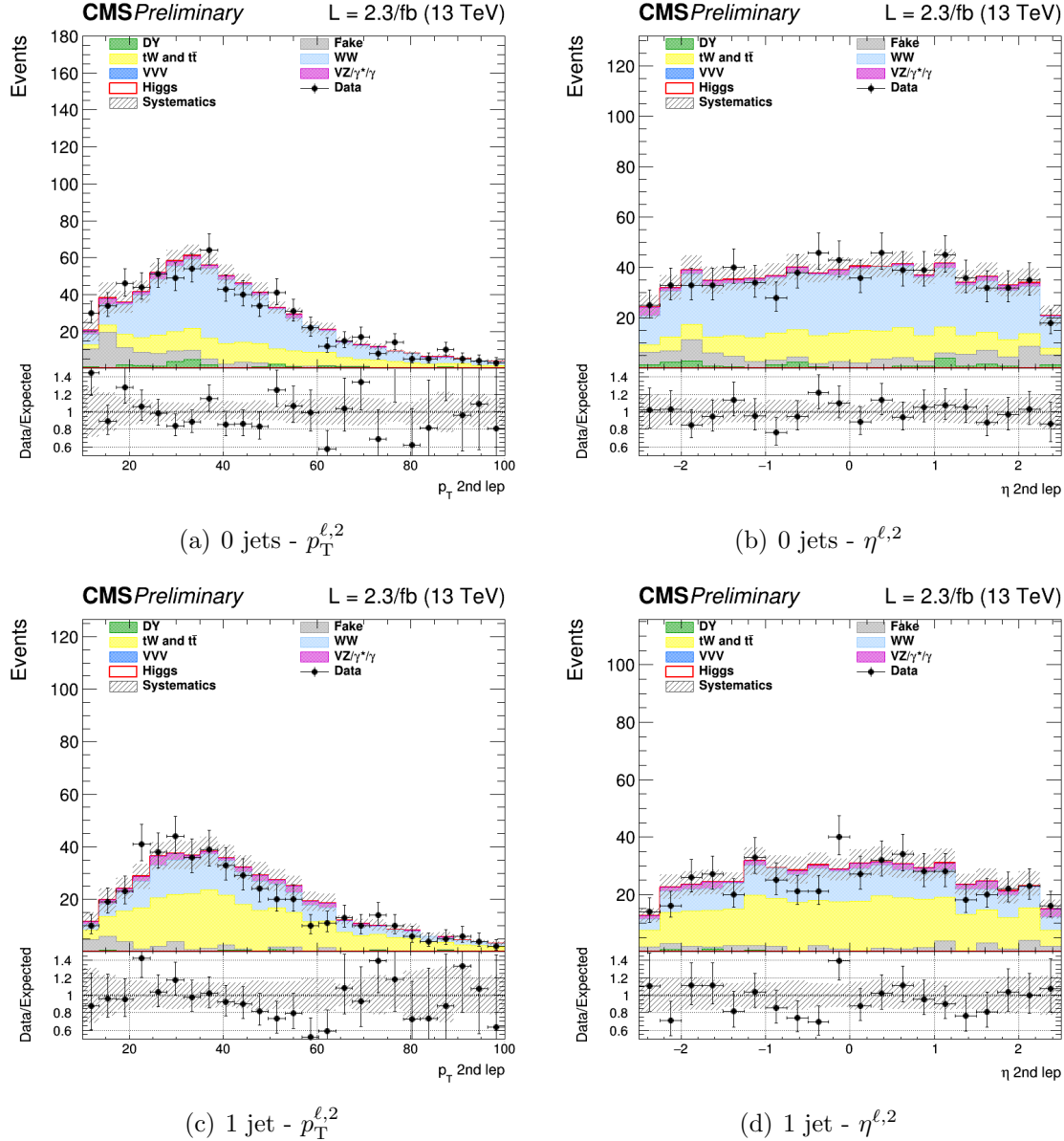


Figure 5.8.: Distributions of p_T (left) and η (right) of the subleading lepton for events with 0 jets (upper row) and 1 jet (lower row), for the main backgrounds (stacked histograms), and for a SM Higgs boson signal with $m_H = 125$ GeV (superimposed and stacked red histogram) at the WW selection level. The last bin of the histograms includes overflows. The simulation of the WW background is normalized to data.

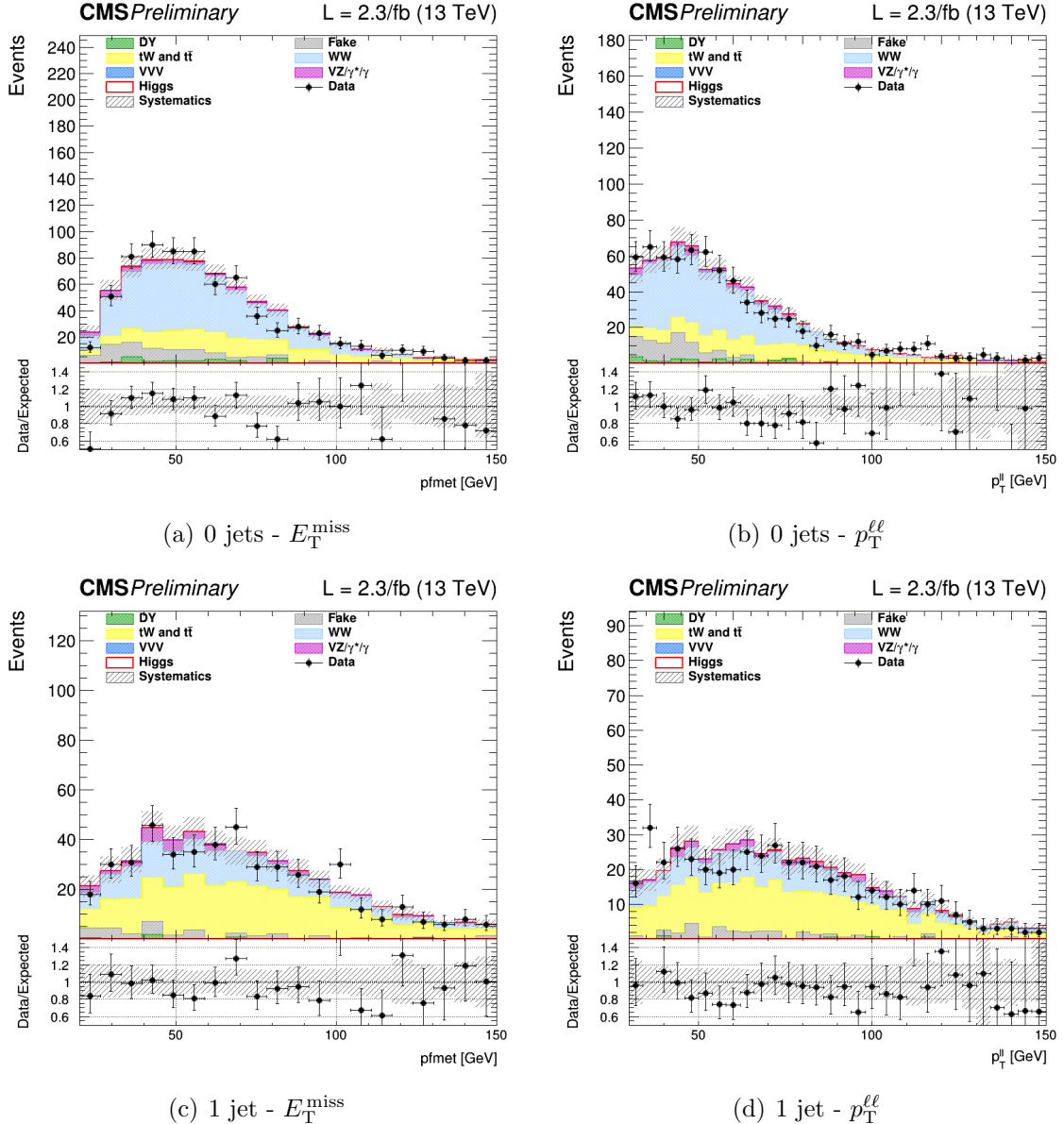


Figure 5.9.: Distributions of E_T^{miss} (left) and $p_T^{\ell\ell}$ (right) for events with 0 jets (upper row) and 1 jet (lower row), for the main backgrounds (stacked histograms), and for a SM Higgs boson signal with $m_H = 125$ GeV (superimposed and stacked red histogram) at the WW selection level. The last bin of the histograms includes overflows. The simulation of the WW background is normalized to data.

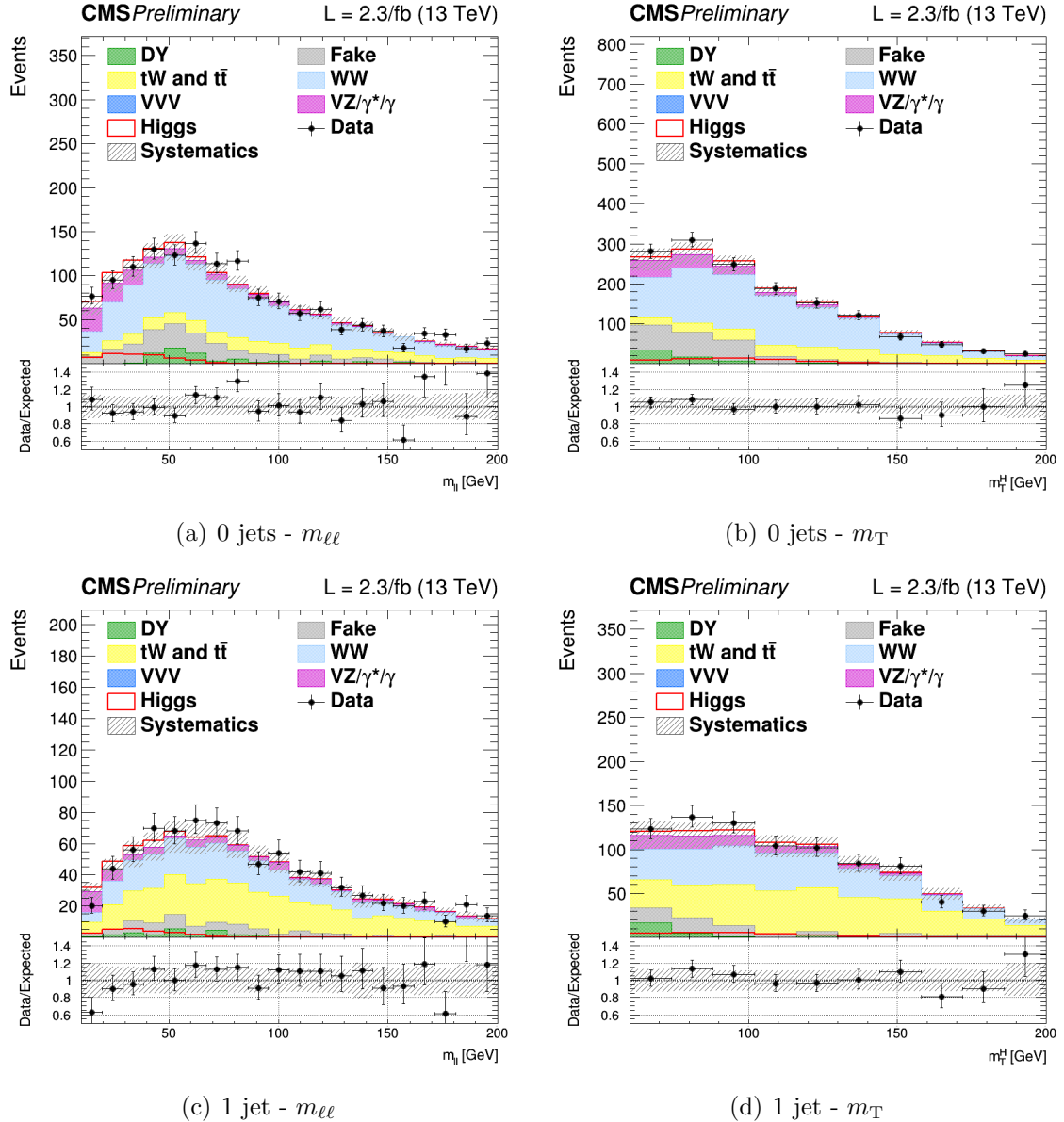


Figure 5.10.: Distributions of $m_{\ell\ell}$ (left) and m_T (right) for events with 0 jets (upper row) and 1 jet (lower row), for the main backgrounds (stacked histograms), and for a SM Higgs boson signal with $m_H = 125$ GeV (superimposed and stacked red histogram) at the WW selection level. The last bin of the histograms includes overflows. The simulation of the WW background is normalized to data.

2046 5.4. Background estimation

2047 The main background processes affecting the analysis signature, non-resonant WW pro-
 2048 duction and top quark processes, are estimated using data. Backgrounds arising from an
 2049 experimental misidentification of the objects, such as W+jets (also called “Fake”), are
 2050 estimated using data as well. The other minor backgrounds are generally estimated directly
 2051 from simulation as described in the following subsections.

2052 5.4.1. WW background

2053 The quark-induced WW background is simulated with NLO accuracy in perturbative
 2054 QCD, and the transverse momentum of the diboson system is reweighted to match the
 2055 NNLO+NNLL accuracy from theoretical calculations [89, 90]. However, given the large
 2056 uncertainties on the jet multiplicity distribution associated to this process, the normalization
 2057 of this background is measured from data separately for the 0 and 1 jet categories. The
 2058 normalization k-factors are extracted directly from the fit together with the signal strengths,
 2059 leaving the WW normalization free to float separately in the two jet multiplicity categories.
 2060 An orthogonal control region for the WW background normalization estimation is not
 2061 needed in this case, owing to the different $m_{\ell\ell}$ - m_T shape for signal and background.

2062 The gluon-induced WW production is sub-dominant with respect to the quark-induced
 2063 production, and its shape and normalization is fully taken from simulation, scaling the
 2064 cross section to the theoretical prediction with NLO accuracy [98].

2065 5.4.2. Top quark background

2066 As explained in Sec. 5.3, the production of top quark pairs represents one of the dominant
 2067 backgrounds in this analysis given its large cross section and a similar final state compared
 2068 to the signal. A b-jet veto, based on the *cMVAv2* b tagging algorithm, is used to suppress
 2069 this background and a reweighting procedure is applied on top of the simulated events to
 2070 correct for different b tagging efficiency in data and simulation.

2071 The top quark background normalization is measured using data, defining a b-jets
 2072 enriched control region by inverting the b-jet veto. More precisely, the b-jets enriched
 2073 control region for the 0-jet category is defined with the same WW baseline selection but
 2074 requiring at least one jet with $20 < p_T < 30$ GeV to be identified as a b jet and no other
 2075 jets with $p_T > 30$ GeV. For the 1-jet category, the b-jets enriched region is defined requiring
 2076 exactly one jet with $p_T > 30$ GeV identified as a b-jet. To reduce other backgrounds in
 2077 these two regions, the dilepton mass has to be greater than 50 GeV. Distributions of the
 2078 $m_{\ell\ell}$ and m_T variables in the b-jets enriched control regions after applying the data driven
 2079 estimation are shown in Figure 6.5, for the 0 and 1 jet categories separately.

2080 The top quark background normalization is constrained during the fit procedure sepa-
 2081 rately in the two jet categories, by means of the control regions defined above, which are
 2082 treated in the fit as two additional categories.

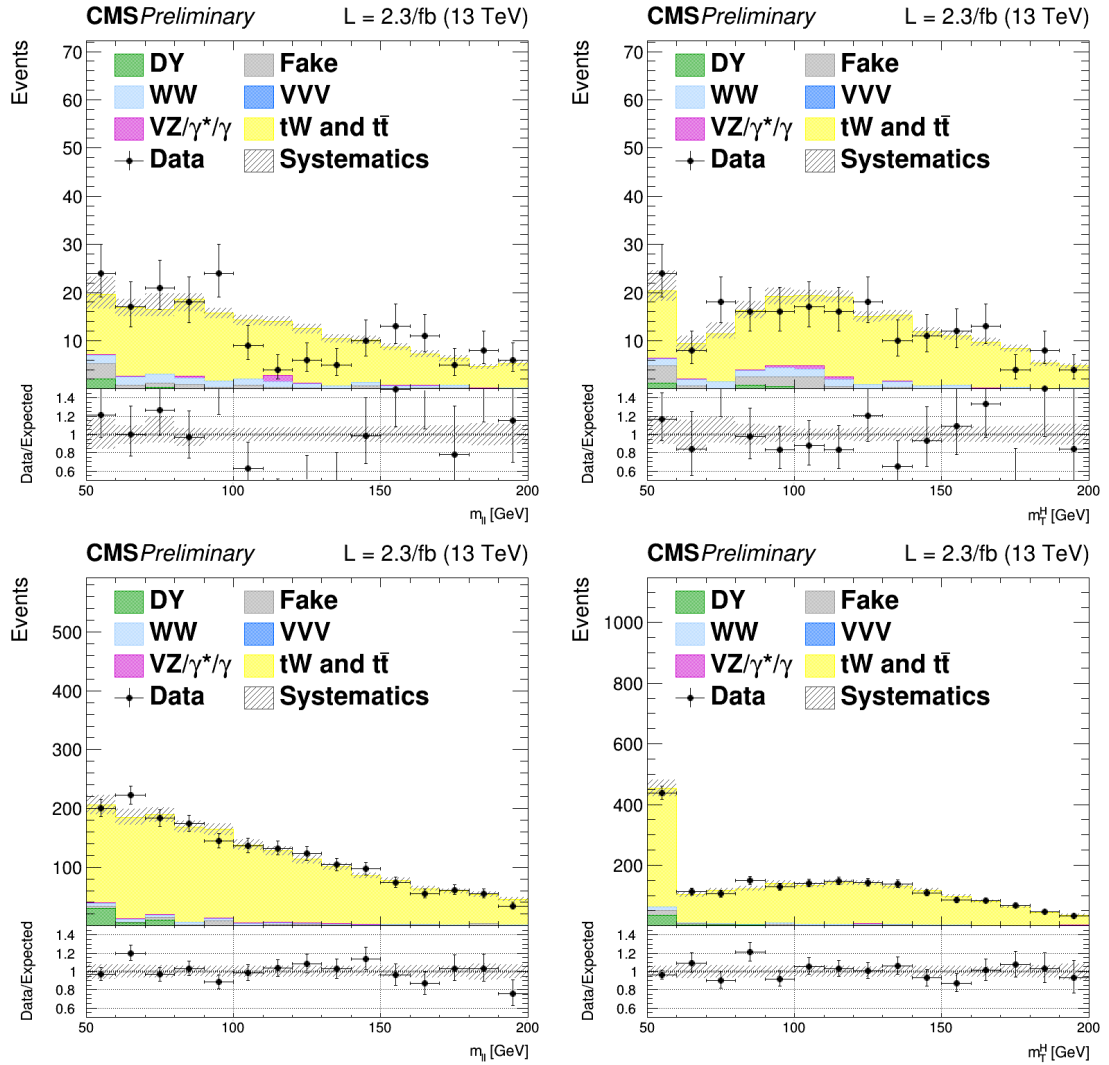


Figure 5.11.: Distributions of $m_{\ell\ell}$ (left) and m_T (right) for events with 0 jet (top) and 1 jet (bottom) in top enriched phase space. Scale factors estimated from data are applied. The first (last) bin includes underflows (overflows).

2083 5.4.3. Jet-induced (or Fake) background

2084 One of the primary source belonging to this category arises from the misidentification of
 2085 leptons in $W+jets$ processes in the 0 jet category. Also, semileptonic $t\bar{t}$ decays contribute
 2086 especially for higher jet multiplicities. Multijet production and hadronic $t\bar{t}$ decays are also
 2087 taken into account, but have a much smaller contribution.

2088 This background is fully estimated using data, with the technique described in Sec. 4.4.3.
 2089 To check the agreement of the background estimated in this way with data, a control sample
 2090 enriched in jet-induced events is defined. The events in the control sample are selected
 2091 applying the WW baseline requirements but requesting an $e\mu$ pair with same charge, which
 2092 significantly suppresses the WW and $t\bar{t}$ processes. The $m_{\ell\ell}$ distributions in this control
 2093 region for the 0 and 1 jet categories are shown in Fig. 5.12. From the crosscheck in this
 2094 control region, a global normalization factor of 0.8 is derived and applied to the jet-induced
 2095 background.

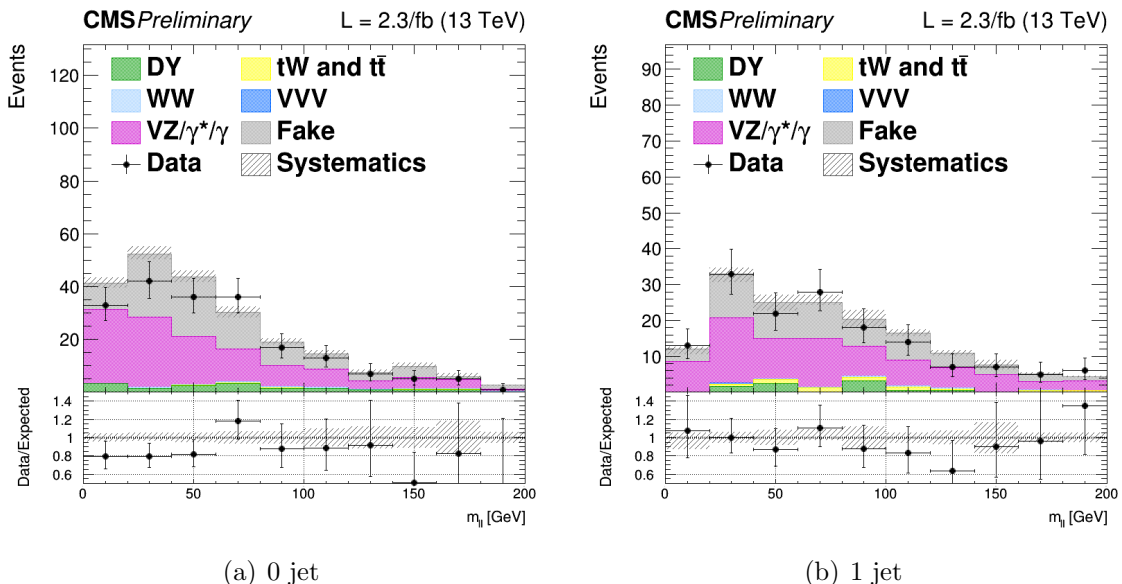


Figure 5.12.: Control plots for $m_{\ell\ell}$ in a fakes enriched phase space for events with 0 and 1 jet with $p_T > 30$ GeV, in $e\mu$ final state. Fake contribution has been scaled by 0.8 to match data.

2096 5.4.4. DY background

2097 This background contributes to the analysis phase space because of the Z/γ^* decays to a
 2098 pair of τ leptons, which consequently decays to an $e\mu$ pair. This background process is
 2099 predominant in the low m_T region, which is used as an orthogonal control region to determine
 2100 the background normalization in the 0 and 1 jet categories separately. In particular this
 2101 control region is defined by selecting events with $m_T < 60$ GeV and 30 GeV $< m_{\ell\ell} < 80$ GeV.

2102 The $m_{\ell\ell}$ distributions in these control regions for the 0 and 1 jet categories are shown in
 2103 Fig. 5.13.

2104 As for the top quark background, the normalization of this background in the 0 and 1
 2105 jet categories, is constrained directly in the fit by means of the control regions, which are
 2106 treated as two additional categories.

2107 The kinematics of this background is taken from simulation, after reweighting the Z
 2108 boson p_T spectrum to match the observed distribution measured in data. In fact, this
 2109 variable is not well reproduced by the MC generator used for simulating this process,
 2110 especially in the bulk of the distribution, the discrepancy being ascribed to the missing
 2111 contribution from resummed calculations.

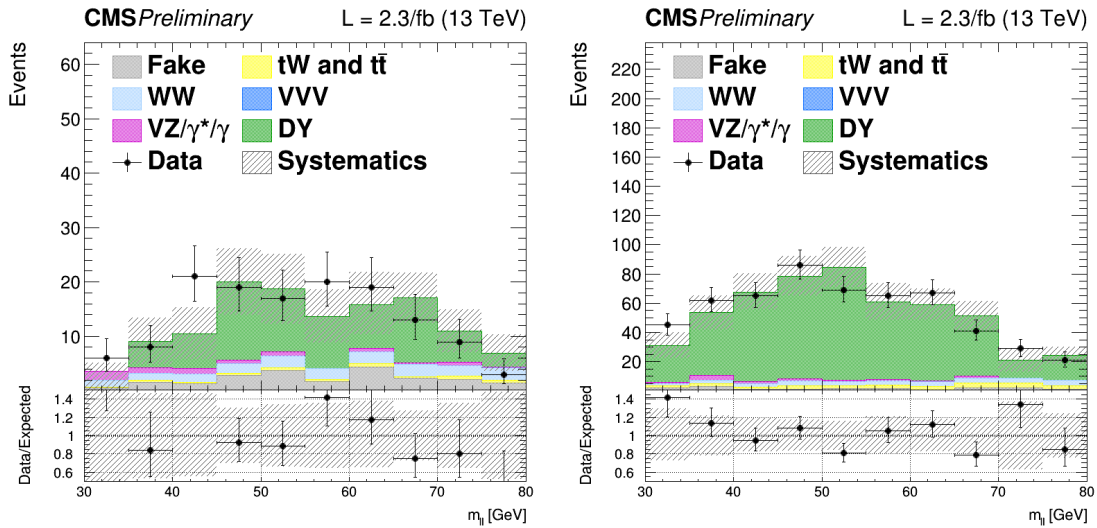


Figure 5.13.: Distributions of $m_{\ell\ell}$ for events with 0 jet (left) and 1 jet (right) in the $DY \rightarrow \tau\tau$ enriched control region. Scale factors estimated from data are applied.

2112 5.4.5. Other backgrounds

2113 The $W\gamma^*$ and the WZ electroweak processes can be gathered in the same physical process,
 2114 although the final state kinematics is rather different. In particular, the invariant mass of
 2115 the leptons arising from the γ^* decays is generally below 4 GeV, while the leptons from the
 2116 Z boson decay are characterized by a larger invariant mass. Another background which can
 2117 be experimentally identical to those is the $W\gamma$ production, where a real photon is produced
 2118 in association with a W boson and consequently undergoes a photon conversion to leptons
 2119 due to the interaction with the material constituting the first layers of the silicon tracker.

2120 All these backgrounds may contribute to the signal phase space whenever one of the three
 2121 leptons escape from the detector acceptance or is not identified. The shape and cross section
 2122 of these backgrounds are taken from simulation. The only exception is the normalization of
 2123 the $W\gamma^*$ background, being this process dominant in the low $m_{\ell\ell}$ region, which is scaled

2124 to data defining a proper control region. The control region is defined selecting events
2125 with three isolated muons, with $p_T > 10.5$ and 3 GeV for the first three leading muons
2126 respectively. The selection is further defined by $E_T^{\text{miss}} < 25$ GeV and E_T^{miss} projected to the
2127 leading muon < 45 GeV. The pair of muons with the smallest invariant mass is taken as
2128 coming from the γ^* decay. The k-factor measured in data for this background to be applied
2129 in the simulation is 1.98 ± 0.54 .

2130 All remaining backgrounds from di-boson and tri-boson production, which are of mi-
2131 nor importance in the analysis phase space, are normalized according to their expected
2132 theoretical cross sections.

2133 5.5. Systematic uncertainties

2134 The systematic uncertainties affecting this measurement can be divided into three categories:
2135 the uncertainties on the background estimation, experimental uncertainties and theoretical
2136 uncertainties.

2137 The first category includes the uncertainties related to the background normalization
2138 and shape. For the non-resonant WW production the shape is taken from simulation.
2139 The input normalization to the fit is set to the expected value from simulation, and an
2140 unconstrained nuisance parameter with a flat distribution is associated to this number.
2141 This is done separately for the two jet categories.

2142 The top quark background shape is taken from simulation after correcting for the b
2143 tagging scale factors. An uncertainty due to these scale factors is included and affects
2144 both the normalization and the shape of the top quark background. The uncertainties on
2145 the normalization are treated similarly to the WW background case, but constraining the
2146 corresponding nuisances by means of the two control regions orthogonal to the signal phase
2147 space. A similar procedure is used for the DY background.

2148 Effects due to experimental uncertainties are studied by applying a scaling and smearing
2149 of certain variables related to the physics objects, e.g. the p_T of the leptons, followed by
2150 a subsequent recalculation of all the correlated variables. This is done for simulation, to
2151 account for possible systematic mismodeling.

2152 All experimental sources, except luminosity, are treated both as normalization and shape
2153 uncertainties, and are correlated among the signal and background processes and all the
2154 categories. The following experimental uncertainties are considered:

- 2155 • the uncertainty determined by the CMS online luminosity monitoring, 2.7% for the
2156 first data collected at $\sqrt{s} = 13$ TeV;
- 2157 • the acceptance uncertainty associated with the combination of single and double lepton
2158 triggers, which is 2%;
- 2159 • the lepton reconstruction and identification efficiencies uncertainties, that are in the
2160 range 0.5-5% for electrons and 1-7% for muons depending on p_T and η ;
- 2161 • the muon momentum and electron energy scale and resolution uncertainties, that
2162 amount to 0.01-0.5% for electrons and 0.5-1.5% for muons depending on p_T and η ;

- 2163 • the jet energy scale uncertainties, that vary between 1-11% depending on the p_T and
2164 η of the jet;
- 2165 • the E_T^{miss} resolution uncertainty, that is taken into account by propagating the corre-
2166 sponding uncertainties on the leptons and jets;
- 2167 • the scale factors correcting the b tagging efficiency and mistagging rate, that are varied
2168 within their uncertainties. This systematic uncertainty is anticorrelated between the
2169 top control regions and the other ones.

2170 The uncertainties in the signal and background production rates due to theoretical
2171 uncertainties include several components, which are assumed to be independent: the PDFs
2172 and α_s , the underlying event and parton shower model, and the effect of missing higher-order
2173 corrections via variations of the renormalization and factorization scales.

2174 The effects of the variation of PDFs, α_s and renormalization/factorization QCD scales,
2175 mainly affect the signal processes, being the most important backgrounds estimated using
2176 data driven techniques. However, the uncertainties on minor backgrounds that are estimated
2177 from simulation are taken into account. These uncertainties are split in the uncertainties
2178 on the cross section, which are computed by the LHC cross section working group [102],
2179 and on the selection efficiency [103]. The PDFs and α_s signal cross section normalization
2180 uncertainties are $^{+7.4\%}_{-7.9\%}$ and $^{+7.1\%}_{-6.0\%}$ for ggH and $\pm 0.7\%$ and $\pm 3.2\%$ for VBF Higgs production
2181 mechanism. The PDFs and α_s acceptance uncertainties are less than 1% for gluon- and
2182 quark-induced processes. The effect of the QCD scales variation on the selection efficiency is
2183 around 1-3% depending on the specific process. To estimate these uncertainties, the events
2184 are reweighted according to different QCD scales or different PDF sets and the selection
2185 efficiency is recomputed each time. For the QCD scale uncertainty the maximum variation
2186 with respect to the nominal value is taken as the uncertainty. For the case of PDF and α_s
2187 uncertainties, the distribution of the selection efficiency is built taking into account all the
2188 replicas in the NNPDF3.0 set and the uncertainty is estimated as the standard deviation of
2189 that distribution.

2190 In addition, the categorization of events based on jet multiplicity introduces additional un-
2191 certainties on the ggH production mode related to missing higher order corrections. These un-
2192 certainties are evaluated following the prescription described in Sec. [subsec:stewart-tackman]
2193] and correspond to 5.6% for the 0-jet and 13% for the 1-jet bin categories.

2194 The underlying event uncertainty is estimated by comparing two different PYTHIA
2195 8 tunes, while parton shower modelling uncertainty is estimated by comparing samples
2196 interfaced with the PYTHIA 8 and HERWIG++ parton shower programs. The effect on the
2197 ggH (VBF) signal expected yield is about 5% (5%) for the PYTHIA 8 tune variation and
2198 about 7% (10%) for the parton shower description.

2199 Other specific theoretical uncertainties are associated to some backgrounds. An uncer-
2200 tainty on the ratio of the $t\bar{t}$ and tW cross sections is included. Indeed, these two processes
2201 are characterized by a different number of b-jets in the final state (2 b-jets for $t\bar{t}$ and 1
2202 for tW) and the b-veto acts differently for the two. A variation of the relative ratio of the
2203 cross sections can thus cause a migration of events from the 0 to the 1 jet categories and

2204 viceversa. The corresponding uncertainty is of 8%, according to the theoretical cross section
2205 calculations [99, 100].

2206 The $gg \rightarrow WW$ background LO cross section predicted by the MCFM generator is scaled
2207 to the NLO calculation, applying a k-factor of 1.4 with an uncertainty of 15% [98]. The
2208 interference term between the $gg \rightarrow WW$ and the ggH signal is also included and simulated
2209 with LO accuracy using MCFM. The k-factor to scale the interference term is 1.87, given by
2210 the geometrical average of the LO to NNLO $gg \rightarrow H \rightarrow WW$ scale factor (2.5) and the LO
2211 to NLO $gg \rightarrow WW$ scale factor (1.4). The uncertainty on this value is estimated as the
2212 maximum variation with respect to the two scale factors mentioned above, and is found
2213 to be of 25%. Anyway, with the current amount of integrated luminosity, the interference
2214 contribution is found to be negligible.

2215 For what the $qq \rightarrow WW$ background shape is concerned, an uncertainty related to
2216 the diboson p_T reweighting is evaluated varying the renormalization, factorization and
2217 resummation QCD scales.

2218 Finally, the uncertainties due to the limited statistical accuracy of the MC simulations
2219 are also taken into account, including an independent uncertainty for each bin of the
2220 two-dimensional distribution, and for each category. The uncertainty for a certain bin
2221 and process is given by the standard deviation of the Poisson distribution with mean
2222 corresponding to the number of MC events in that bin.

2223 5.6. Results

2224 The expected and observed signal significance are shown in Table 5.6 for all the categories
2225 separately. Also, the observed signal strengths and the corresponding uncertainties are
2226 shown. The best fit signal strength obtained combining all the categories together is found
2227 to be $0.3^{+0.5}_{-0.5}$, corresponding to an observed significance of 0.7σ , to be compared with the
2228 expected significance of 2.0σ for a Higgs boson mass of 125 GeV.

2229 Maybe I should add the nuisances impact plots...

Table 5.6.: Observed and expected significance and signal strength the SM Higgs boson with a mass of 125 GeV for the 0-jet and 1-jet, μe and $e\mu$, categories.

Category	Expected significance	Observed significance	σ/σ_{SM}
0-jet μe	1.1	1.3	$1.13^{+0.9}_{-0.9}$
0-jet $e\mu$	1.3	0.4	$0.33^{+0.7}_{-0.7}$
1-jet μe	0.8	0	$-0.11^{+0.5}_{-1.7}$
1-jet $e\mu$	0.9	0	$-0.54^{+1.4}_{-1.4}$
0-jet	1.6	1.3	$0.71^{+0.6}_{-0.5}$
1-jet	1.2	0	$-0.56^{+1.0}_{-1.0}$
Combination	2.0	0.7	$0.33^{+0.5}_{-0.5}$

Chapter 6.

2230 **Search for high mass resonances 2231 decaying to a W boson pair with first 2232 13 TeV LHC data**

2233 **6.1. Introduction**

2234 In this chapter, a search for a high mass spin-0 particle (from now on denoted as X)
2235 in the $X \rightarrow WW \rightarrow \ell\nu\ell'\nu'$ decay channel is presented, where ℓ and ℓ' refer to an different
2236 flavour lepton pair, i.e. $e\mu$. The search is based upon proton-proton collision data samples
2237 corresponding to an integrated luminosity of up to 2.3 fb^{-1} at $\sqrt{s} = 13 \text{ TeV}$, recorded by
2238 the CMS experiment at the LHC during 2015. This analysis represents a general extension
2239 of the SM Higgs boson search presented in 5 and is performed in a range of heavy scalar
2240 masses from $M_X = 200 \text{ GeV}$ up to 1 TeV , extending the range studied in a similar analysis
2241 performed using Run 1 LHC data [104], which provided upper limits on the production
2242 cross section of new scalar resonances up to 600 GeV .

2243 Despite the discovery of a particle consistent with the SM Higgs boson in 2012, there is a
2244 possibility that this particle is only a part of a larger Higgs sector, and hence only partially
2245 responsible of the EW symmetry breaking. This can be achieved in different theoretical
2246 models that extends the SM, such as the two-Higgs-doublet models [105–107], or models in
2247 which the SM Higgs boson mixes with a heavy EW singlet, which predict the existence
2248 of an additional resonance at high mass, with couplings similar to those of the SM Higgs
2249 boson, as most recently described in [108, 109].

2250 This analysis reports a generic search for a scalar particle with different resonance decay
2251 widths hypothesis, produced via the ggH and VBF production mechanisms. The results
2252 can then be interpreted in terms of different theoretical models. This analysis is heavily
2253 based on the SM Higgs search described in 5, in terms of physics objects, selections and
2254 background estimation. The differences and similarities are discussed in this chapter.

2255 **6.2. Data and simulated samples**

2256 The data sets, triggers, pile up reweighting, lepton identification and isolation used in this
2257 analysis are the same as the SM Higgs search and are described in Sec. 5.2.

Also, the same MC simulations are used for the background processes, the only exception being the DY background, for which the MG5_AMC@NLO generator is used with LO QCD accuracy, matching together events with up to four jets in addition to the vector boson with the MLM [110] matching scheme. Given that this analysis aims to probe regions of phase space where the DY contribution is very small, like in the high transverse mass region, the usage of a simulation of the inclusive DY process may lead to large uncertainties due to the limited simulation statistics in the sample. To partially overcome this issue, different DY samples are generated in restricted portions of the phase space defined by the H_T variable, i.e. the scalar sum of all the partons p_T in the event. For $H_T < 100$ GeV the inclusive simulation is used, while different samples are used for higher values of H_T . The samples are merged using the parton level information, and it has been verified that a smooth transition between different H_T regions is achieved, as shown in Fig. 6.1. The DY LO cross section obtained from the simulation is scaled using the LO to NNLO k-factor of 1.23.

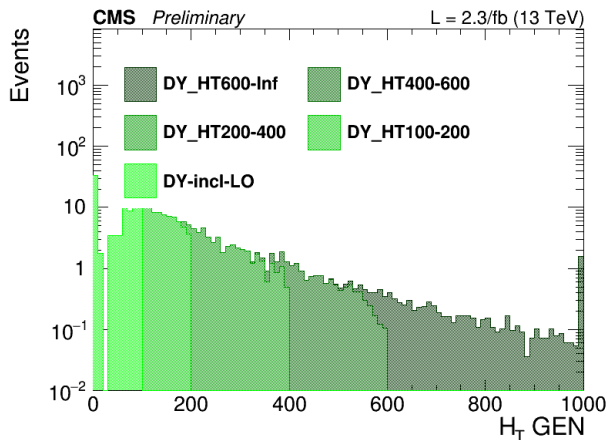


Figure 6.1.: Generator level H_T distribution for the merged DY sample.

In order to perform the resonance search in a large part of the mass spectrum, several signal samples for the gluon-gluon fusion and the vector boson fusion mechanisms have been generated corresponding to different Higgs boson masses in the range between 200 GeV and 1 TeV. The signal width for each mass point corresponds to the one expected for a SM Higgs boson at that mass. The samples are produced with a mass step of 50 GeV from 250 to 800 GeV and of 100 GeV from 800 to 1000 GeV. A finer stepping is used between 200 and 250 GeV. All the signal samples are generated with the POWHEG V2 generator, interfaced with the JHUGEN v6.2.8 generator, which handles the decay of the Higgs boson to $W^+W^- \rightarrow 2\ell 2\nu$.

The interference effects among $gg \rightarrow X \rightarrow WW$, $gg \rightarrow WW$ and $gg \rightarrow H \rightarrow WW$ are evaluated using the MCFM and JHUGEN generators, as implemented in the MELA (Matrix Element Likelihood Approach) framework [85]. Details about the interference effects are given in Sec. 6.3.

2285 6.3. Analysis strategy

2286 The analysis strategy for the first results on the high mass search in the $W^+W^- \rightarrow 2\ell 2\nu$
 2287 decay channel closely follows the strategy presented in the 13 TeV SM Higgs search in the
 2288 $H \rightarrow W^+W^- \rightarrow 2\ell 2\nu$ channel regarding the 0 and 1 jet categories. In addition a dedicated
 2289 category to the VBF production mechanism is added, given that this production mode is
 2290 particularly important in the high mass region. Indeed, assuming a SM Higgs boson, the
 2291 ratio of cross sections $\sigma_{\text{VBF}}/\sigma_{\text{ggH}}^1$ increases with the Higgs boson mass, making the VBF
 2292 production mechanism more and more important as the mass of the resonance approaches
 2293 to high values.

2294 This analysis is affected essentially by the same background processes as the SM Higgs
 2295 boson search, with the difference that in this case the SM Higgs boson processes, including
 2296 all production modes, are treated as backgrounds.

2297 In addition to requiring the events to pass the single or double lepton triggers, exactly
 2298 one electron and one muon are required to be reconstructed in the event with opposite
 2299 charges and a minimum p_T of 20 GeV for both the muon and electron. Both leptons are
 2300 required to be well identified and isolated to reject fake leptons and leptons coming from
 2301 decays in flight. To suppress background processes with three or more leptons in the final
 2302 state, such as diboson or triboson production, events with any additional identified and
 2303 isolated lepton with $p_T > 10$ GeV are rejected. To suppress the contribution of the SM
 2304 production of the Higgs boson at 125 GeV, $m_{\ell\ell}$ is requested to be higher than 50 GeV. The
 2305 other event requirements are identical to the 125 GeV Higgs boson search and are described
 2306 in Sec. 5.3.2.

2307 In addition to the 0 and 1 jet categories, a specific category sensitive to the VBF
 2308 production mode is defined exploiting the characteristic signature of this process, where
 2309 two energetic jets are emitted in the forward region of the detector and with large $\Delta\eta$
 2310 gap. Events belonging to the VBF-enriched category are selected by requiring at least
 2311 two jets with $p_T > 30$ GeV, an invariant mass $m_{jj} > 500$ GeV and a gap in pseudorapidity
 2312 $\Delta\eta_{jj} > 3.5$.

2313 In addition to the transverse mass variable m_T , which is used in the analysis selection
 2314 to define the DY background control region, an additional variable is defined, that from
 2315 now on will be labelled as “improved transverse mass” m_T^i . This variable is defined as
 2316 the invariant mass of the four momentum resulting from the sum of the two leptons four
 2317 momenta ($p_{\ell\ell}, \vec{p}_{\ell\ell}$) and four momentum $\mathbf{E}_T^{\text{miss}} = (E_T^{\text{miss}}, \vec{p}_T^{\text{miss}})$, i.e.:

$$m_T^i = \sqrt{(p_{\ell\ell} + E_T^{\text{miss}})^2 - (\vec{p}_{\ell\ell} + \vec{p}_T^{\text{miss}})^2} \quad . \quad (6.1)$$

2318 This variable allows having a better sensitivity to different resonance mass hypothesis
 2319 as shown in Fig. 6.2, where the shape of the m_T^i variable is shown for different SM Higgs
 2320 mass hypothesis and it is compared to the standard m_T variable. The usage of this variable

¹The ggH notation is used for the gluon-gluon fusion production mode, even in the cases where a non-SM Higgs boson is created in the process.

also provide a good discriminating power between signal and background, which depends on the particular signal mass hypothesis.

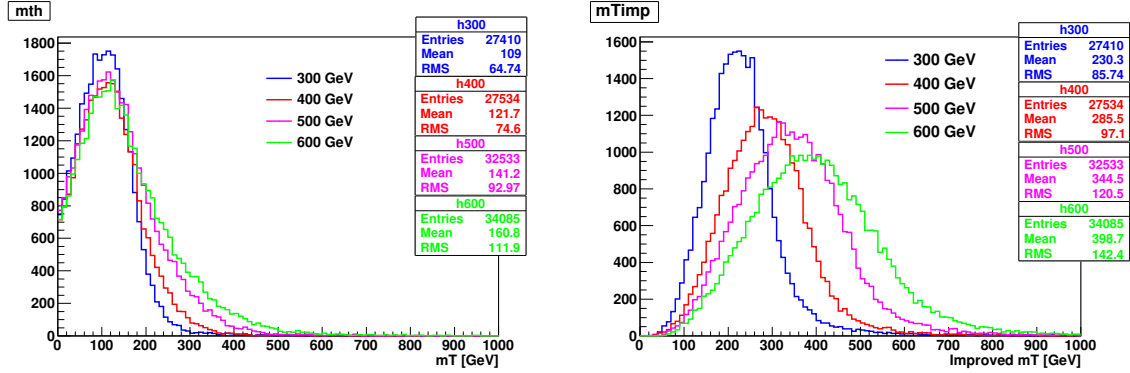


Figure 6.2.: Distribution of the m_T and m_T^i variables at generator level for different resonance mass hypothesis.

The signal extraction is based on a binned maximum likelihood fit using the m_T^i distribution for signal and background contributions as templates. The m_T^i template is defined using the following bin boundaries:

- **0/1 jet:** $[100, 150, 200, 250, 300, 350, 400, 450, 500, 600, 700, 1000]$,
- **VBF:** $[100, 150, 200, 250, 300, 350, 400, 500, 700, 1000]$,

where the first number represents the lower edge of the first bin while the other numbers represent the upper edges. The last bin is an overflow bin.

In order to test different resonance decay widths hypotheses, the signal samples, which are generated with a decay width corresponding to the expected value for a SM Higgs boson at that mass (Γ_{SM}), are reweighted to obtain the desired width value (Γ'). In particular the following values are used: $\Gamma' = \Gamma_{\text{SM}}$, $\Gamma' = 0.49 \times \Gamma_{\text{SM}}$, $\Gamma' = 0.25 \times \Gamma_{\text{SM}}$ and $\Gamma' = 0.09 \times \Gamma_{\text{SM}}$. The reweighting is performed at generator level by computing the ratio of two relativistic Breit Wigner distributions with different decay widths, $f(E, \Gamma', M_X)/f(E, \Gamma_{\text{SM}}, M_X)$, where:

$$f(E) \propto \frac{1}{(E^2 - M^2)^2 + M^2 \Gamma^2} \quad . \quad (6.2)$$

Here, $f(E, \Gamma_{\text{SM}}, M_X)$ represents the distribution used for the simulation of the signal at a mass M_X , and $f(E, \Gamma', M_X)$ the distribution with the new decay width. Each event is multiplied by this ratio (which depends on the energy E of the event) to obtain the reweighted distribution.

When a resonance with a non negligible width is considered, it is important to take into account the interference effects both with the $gg \rightarrow WW$ background and the SM Higgs boson off-shell tail. A study of the interference effects for a resonance X produced through the gluon fusion mechanism is performed within the MCFM+JHUGEN framework, and

2344 including NNLO corrections for cross section using HNNLO program [111] based on
 2345 MCFM. The matrix element package MELA supports all of these processes and allows fast
 2346 MC re-weighting and optimal discriminant calculation. The basic idea of this approach is to
 2347 compute the matrix elements of the processes under study with the MCFM and JHUGEN
 2348 generators, including the interference terms, and using these matrix elements to compute
 2349 an event weight used to reweight the simulated samples. Using this approach the simulated
 2350 events can be reweighted according to different scenarios, for instance including some or all
 2351 the interference terms, allowing a detailed study of the interference contribution. The effect
 2352 of the various interference terms for the M_X variable at generator level is shown in Fig. 6.3,
 2353 after having applied the WW baseline selections. As can be observed the contribution of
 2354 the interference of the scalar resonance with the $gg \rightarrow WW$ background and with SM Higgs
 2355 boson have opposite sign and partially cancel out. This cancellation effect is different for
 2356 different resonance masses and depends on the event selection. In particular the interference
 2357 term with the SM Higgs off-shell tail is positive for values below M_X while it turns negative
 2358 above M_X . The contribution of the interference with the $gg \rightarrow WW$ background is instead
 2359 characterized by an opposite sign lineshape, thus leading to a partial cancellation when
 2360 considering the total interference.

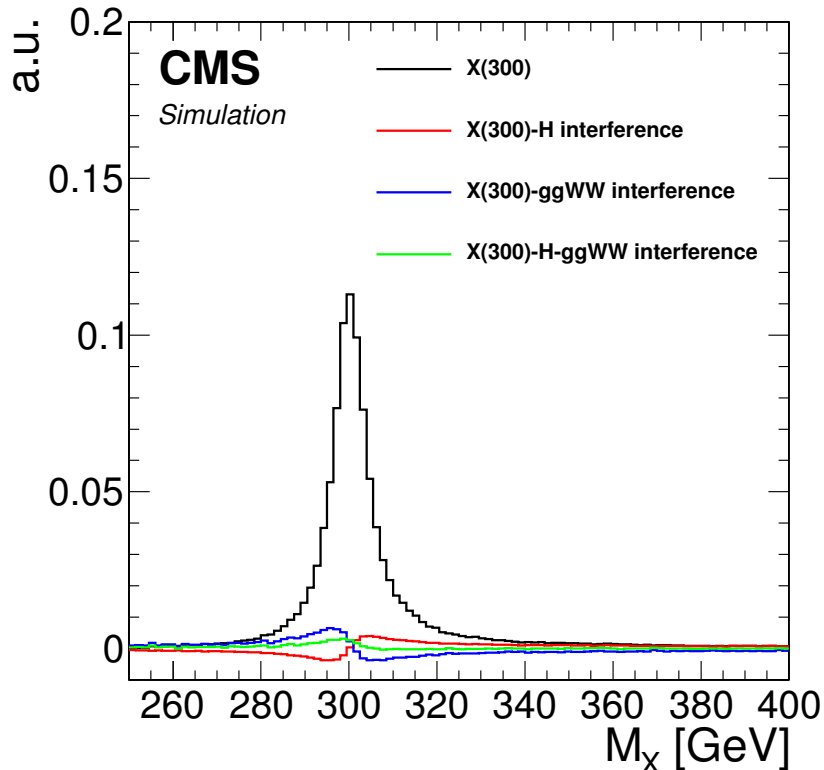


Figure 6.3.: Distribution of the M_X variable for a resonance mass of 300 GeV, showing the various interference terms after the WW baseline selections.

The effect of the resulting interference contribution including all the different terms is shown in Fig. 6.4 for the m_T^i signal templates, in the three categories separately and for different M_X hypotheses.

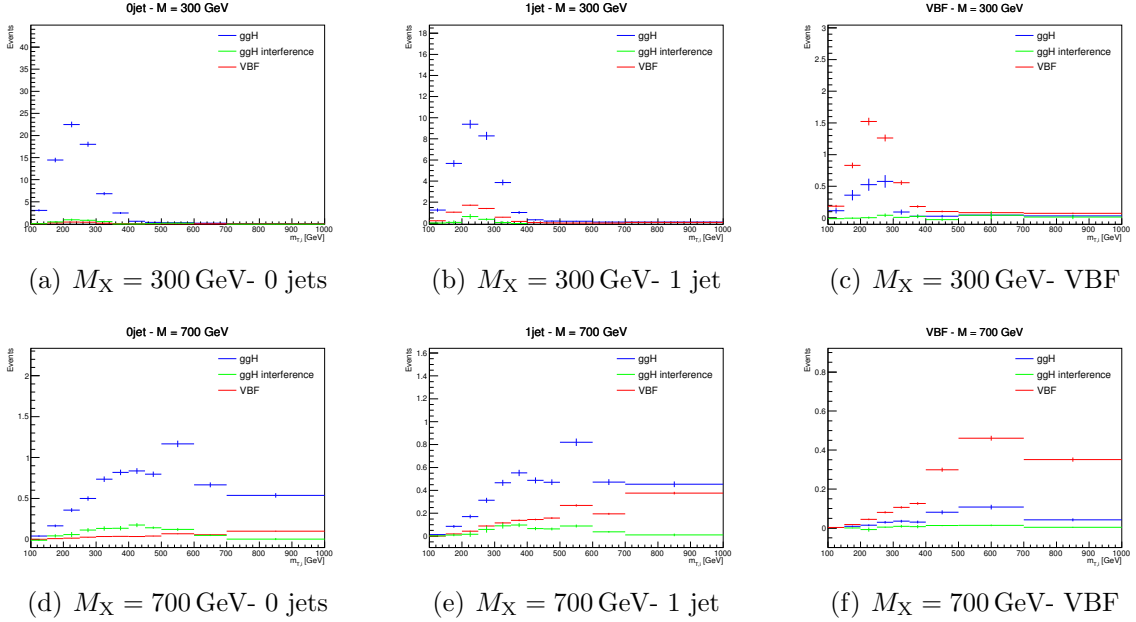


Figure 6.4.: Distributions of the m_T^i variable for $M_X = 300$ and 700 GeV , showing the signal (both the ggH and VBF processes) and the interference contributions in the three jet categories.

The interference contribution is thus not negligible, especially for large values of M_X , and is included in the analysis as part of the signal contribution. More specifically, during the fit procedure the signal yield is scaled by the signal strength parameter μ (which is the parameter of interest of the fit), while the interference yield is scaled by $\sqrt{\mu}$.

6.4. Background estimation

The background processes affecting the analysis phase space are the same as the ones contributing to the SM Higgs search described in Sec. 5.4. The techniques used for the background estimation are the same as well.

The most relevant difference is the addition of the 2 jets category. The WW, top quark and DY background normalizations are estimated in this category using data driven techniques, similarly to the other jet bins.

Given the slightly different WW baseline selection with respect to the SM Higgs search, also the control regions for the top quark and DY backgrounds estimation change, while the WW background normalization is estimated from data in the three signal regions separately, owing to the different m_T^i shapes for signal and background.

For the estimation of the top quark background, three control regions enriched in b-jets are defined by selecting events that pass the WW baseline selections and applying a b tagging requirement which depends on the jet category as follows:

- 0 jets category: at least one b-tagged jet with $20 < p_T < 30$ GeV is required;
- 1 jet category: exactly one b-tagged jet with p_T above 30 GeV is required;
- 2 jets category: at least one b-tagged jet with p_T above 30 GeV is required.

Distributions of the $m_{T,j}^i$ variable in the 0 jets, 1 jet and 2 jets top quark enriched control regions after applying the data driven estimation are shown in Fig. 6.5.

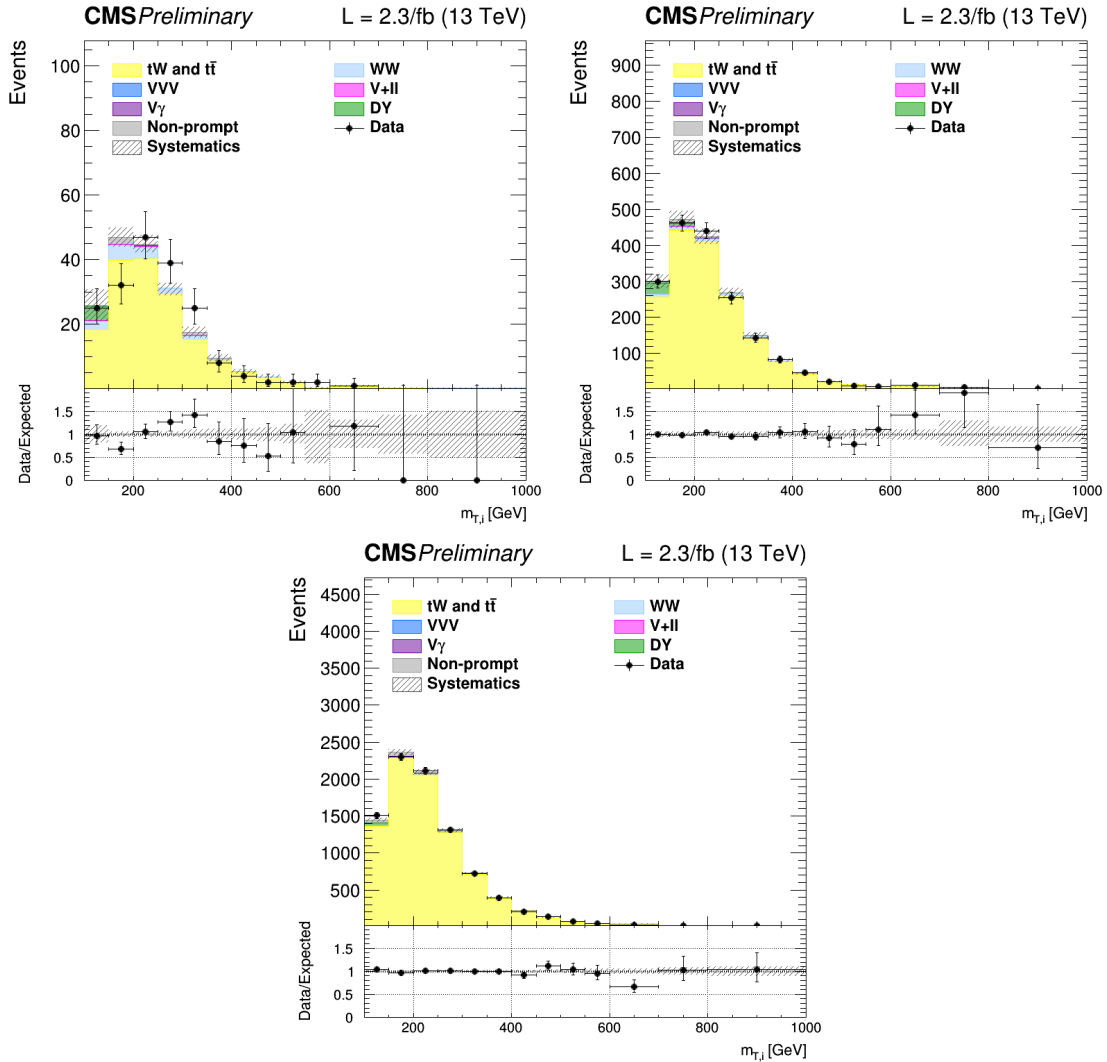


Figure 6.5.: Distributions of $m_{T,j}^i$ for events with 0 jet (top left), 1 jet (top right) and 2 jets (bottom) in top enriched control region. Scale factors estimated from data are not applied in the plots.

2387 The jet induced background, also labelled as “non-prompt” background, so as to highlight
 2388 that these events do not contain prompt leptons, is estimated using the same fake rate
 2389 method described in 4.4.3. A crosscheck is performed selecting events passing the WW
 2390 baseline selection but with an $e\mu$ pair with same charge. The m_T^i distributions for this
 2391 phase space are shown in Fig. 6.6 for the three jet categories separately, showing agreement
 2392 between data and simulation within the uncertainties.

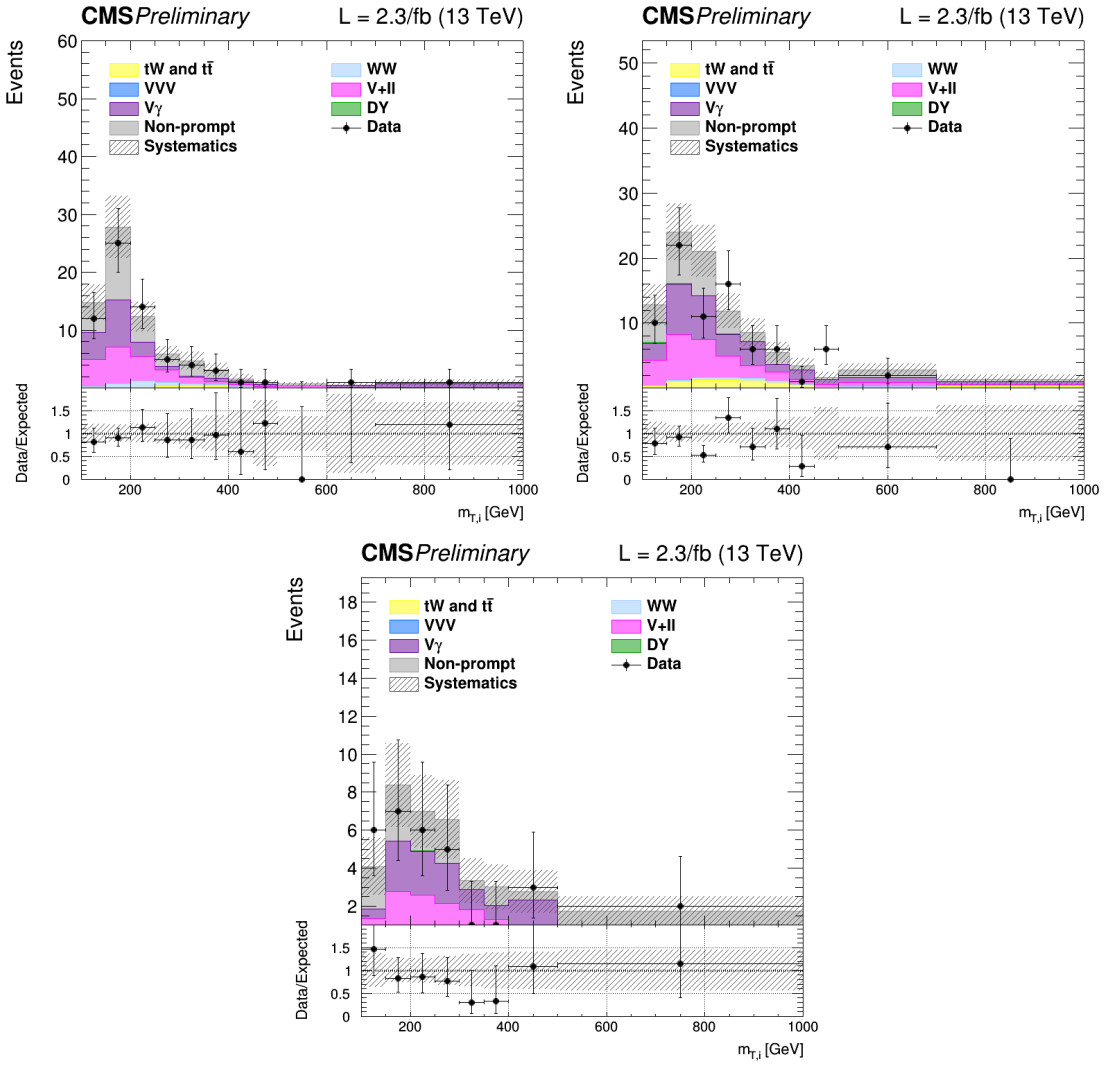


Figure 6.6.: Distributions of m_T^i for events with 0 jet (top left), 1 jet (top right) and 2 jets (bottom) in the same-charge dilepton control region. The last bin of the histograms includes overflows.

2393 Due to the cuts on the leptons p_T and on $m_{\ell\ell}$ in the WW baseline requirements, the
 2394 contribution of the DY background decaying to a pair of τ leptons is very small in the
 2395 signal regions, especially in the VBF phase space. The normalization of this background is
 2396 estimated from a control region in data, defined in the same way as explained in 5.4.4, for

²³⁹⁷ the 0 and 1 jet categories. In the VBF category, given the very small number of expected
²³⁹⁸ events, the normalization of this background is taken from simulation.

²³⁹⁹ Other minor background processes are estimated as described in 5.4.5.

²⁴⁰⁰ 6.5. Systematic uncertainties

²⁴⁰¹ The systematic uncertainties affecting this analysis are the same discussed in Sec. 5.5. The
²⁴⁰² differences with respect to the SM Higgs boson search are described below.

²⁴⁰³ The PDF and α_s uncertainties on the signal cross sections are taken from the computations
²⁴⁰⁴ performed by the LHC cross section working group [102], and are included for all
²⁴⁰⁵ the mass points. The value of these uncertainties depends on the resonance mass and vary
²⁴⁰⁶ from 3 and 5% for ggH and from 2 and 3% for VBF production modes. The PDFs and α_s
²⁴⁰⁷ uncertainties on the signal selection are evaluated for every resonance mass and are found
²⁴⁰⁸ to be less than 1% for both ggH and VBF.

²⁴⁰⁹ The theoretical uncertainties in the signal yields due to the jet categorization are
²⁴¹⁰ evaluated for all the ggH signals following the prescription described in Sec. 4.5.3.

²⁴¹¹ An additional uncertainty on the modelling of the top pair background is derived from
²⁴¹² the observed discrepancy between data and POWHEG V2 plus PYTHIA 8.1 simulation
²⁴¹³ on the top quark p_T spectrum [112], which is particularly important in the tail of the m_T^i
²⁴¹⁴ distribution. Another uncertainty affecting the m_T^i tail for the top quark background is the
²⁴¹⁵ parton shower uncertainty. This is evaluated comparing the generator level m_T^i distributions
²⁴¹⁶ corresponding to two different simulations of the $t\bar{t}$ process: one obtained using PYTHIA
²⁴¹⁷ 8.1 for the showering and hadronization of the simulated events, and the other using
²⁴¹⁸ HERWIG++. The difference between the two is used to extract a shape uncertainty, which
²⁴¹⁹ is less than 1% for low m_T^i values and reaches about 6% in the m_T^i tail.

²⁴²⁰ 6.6. Signal extraction and limit setting

²⁴²¹ The signal yield, including both the ggH and VBF production modes, is extracted performing
²⁴²² a combined fit of the three categories to the m_T^i simulation templates for backgrounds and
²⁴²³ signal, and is repeated for each resonance mass hypothesis. Moreover, fixed the mass of
²⁴²⁴ the resonance, the fit is performed again for the various hypotheses of the resonance decay
²⁴²⁵ width. A single signal strength μ is extracted from the fit, which multiplies both the ggH
²⁴²⁶ and VBF contributions. In other words it is assumed that the ratio of the two production
²⁴²⁷ mechanism stays the same as the one predicted by the SM².

²⁴²⁸ The background yields expected from simulation corresponding to the three jet categories
²⁴²⁹ and after the analysis event selection are shown in Table 6.1. The signal yields corresponding
²⁴³⁰ to a selection of mass points and assuming $\Gamma' = \Gamma_{SM}$ are shown in Table 6.2.

²This is an approximation which limits the amount of models that can be tested with the provided results.

A future development of this analysis will also include the cases for which different ggH and VBF relative contributions are expected.

Table 6.1.: Expected yields estimated from simulation (except for the non-prompt contribution which is estimated using data) for each background process in the three analysis categories, after the analysis event selection. The uncertainties are shown for the processes estimated from simulation.

Background process	0 jets	1 jet	VBF
qq \rightarrow WW	501.93 ± 0.00 (0%)	198.72 ± 0.00 (0%)	4.54 ± 0.00 (0%)
gg \rightarrow WW	37.28 ± 5.77 (15%)	19.63 ± 3.04 (15%)	1.05 ± 0.16 (15%)
Top quark	188.75 ± 0.00 (0%)	330.05 ± 0.00 (0%)	25.06 ± 0.00 (0%)
DY	33.24 ± 0.00 (0%)	12.99 ± 0.00 (0%)	0.28 ± 0.00 (0%)
Non-prompt	64.21 ± 19.26 (30%)	31.69 ± 9.51 (30%)	2.10 ± 0.63 (30%)
V γ	26.62 ± 0.72 (3%)	14.18 ± 0.38 (3%)	0.64 ± 0.02 (3%)
V γ^*	4.44 ± 1.12 (25%)	3.39 ± 0.85 (25%)	0.14 ± 0.04 (25%)
VZ	13.51 ± 0.76 (6%)	11.67 ± 0.66 (6%)	0.28 ± 0.02 (6%)
VVV	0.01 ± 0.00 (3%)	0.02 ± 0.00 (3%)	0.00 ± 0.00 (3%)
SM H \rightarrow WW	6.04 ± 0.40 (7%)	3.10 ± 0.11 (5%)	0.34 ± 0.02 (7%)
SM H \rightarrow $\tau\tau$	0.50 ± 0.05 (9%)	0.43 ± 0.04 (9%)	0.04 ± 0.00 (9%)
Total background	876.5	625.9	34.5

The strategy for computing the exclusion limits is based on the modified frequentist approach, also referred to as CL_s , as described in [101]. The first step is to construct the likelihood function $\mathcal{L}(data|\mu, \theta)$:

$$\mathcal{L}(data|\mu, \theta) = Poisson(data|\mu \cdot s(\theta) + b(\theta)) \cdot p(\tilde{\theta}|\theta) , \quad (6.3)$$

where $data$ represents the experimental observation, s and b are the expected signal and background yields respectively and θ is the full set of nuisance parameters constrained by the prior distribution functions $p(\tilde{\theta}|\theta)$. The default values for the nuisance parameters are labelled as $\tilde{\theta}$.

For a binned shape analysis, $Poisson(data|\mu \cdot s + b)$ is the product of the Poisson probabilities to observe n_i events in bin i :

$$\prod_i \frac{(\mu \cdot s_i + b_i)^{n_i}}{n_i!} e^{-\mu \cdot s_i - b_i} . \quad (6.4)$$

In order to test the compatibility of the data with the signal plus background (or the background only) hypothesis, the test statistic \tilde{q}_μ is constructed based on the profile

Table 6.2.: Expected signal yields for the ggH and VBF production modes estimated from simulation after the analysis event selection for different mass hypothesis assuming $\Gamma' = \Gamma_{\text{SM}}$ in the three analysis categories. The errors correspond to the theoretical uncertainties in the signal estimation.

Mass (GeV)	0 jets	1 jet	VBF
ggH signal yields			
200	90.21 ± 6.67 (7%)	37.47 ± 1.81 (5%)	1.25 ± 0.26 (21%)
400	66.35 ± 4.90 (7%)	32.65 ± 1.57 (5%)	2.04 ± 0.42 (21%)
600	13.86 ± 1.05 (8%)	8.56 ± 0.44 (5%)	0.68 ± 0.14 (21%)
800	3.20 ± 0.25 (8%)	2.32 ± 0.13 (6%)	0.22 ± 0.05 (21%)
1000	0.88 ± 0.07 (8%)	0.70 ± 0.04 (6%)	0.07 ± 0.02 (21%)
VBF signal yields			
200	1.54 ± 0.06 (4%)	6.18 ± 0.25 (4%)	5.05 ± 0.20 (4%)
400	0.91 ± 0.04 (4%)	3.42 ± 0.14 (4%)	3.19 ± 0.13 (4%)
600	0.50 ± 0.02 (4%)	1.95 ± 0.08 (4%)	1.88 ± 0.08 (4%)
800	0.33 ± 0.01 (4%)	1.21 ± 0.05 (4%)	1.16 ± 0.05 (4%)
1000	0.22 ± 0.01 (4%)	0.79 ± 0.03 (4%)	0.69 ± 0.03 (4%)

²⁴⁴² likelihood ratio:

$$\tilde{q}_\mu = -2 \ln \frac{\mathcal{L}(\text{data}|\mu, \hat{\theta}_\mu)}{\mathcal{L}(\text{data}|\hat{\mu}, \hat{\theta})} \quad \text{with } 0 \leq \hat{\mu} \leq \mu \quad , \quad (6.5)$$

²⁴⁴³ where $\hat{\theta}_\mu$ refers to the conditional maximum likelihood estimators of θ , given the signal
²⁴⁴⁴ strength μ . The parameter estimators $\hat{\mu}$ and $\hat{\theta}$ correspond to the global maximum of the
²⁴⁴⁵ likelihood. The $0 \leq \hat{\mu}$ constraint is imposed to have a positive signal yield, e.g. background
²⁴⁴⁶ underfluctuations are forbidden, while $\hat{\mu} \leq \mu$ is imposed to have a one-sided confidence
²⁴⁴⁷ interval. The observed test statistic for the signal strength μ under test is referred to as
²⁴⁴⁸ $\tilde{q}_\mu^{\text{obs}}$. The values of the nuisance parameters obtained maximising the likelihood function are
²⁴⁴⁹ labelled as $\hat{\theta}_0^{\text{obs}}$ and $\hat{\theta}_\mu^{\text{obs}}$ for the background only and signal plus background hypotheses,
²⁴⁵⁰ respectively. The pdf of the test statistic is constructed by generating toy MC pseudo-data
²⁴⁵¹ for both the background only and signal plus background hypotheses, i.e. $f(\tilde{q}_\mu|\mu, \hat{\theta}_\mu^{\text{obs}})$ and
²⁴⁵² $f(\tilde{q}_\mu|0, \hat{\theta}_0^{\text{obs}})$. These distributions can be used to define two p-values corresponding to the

2453 two hypotheses, p_μ and p_b :

$$p_\mu = P(\tilde{q}_\mu \geq \tilde{q}_\mu^{\text{obs}} | \text{signal + background}) = \int_{\tilde{q}_\mu^{\text{obs}}}^{\infty} f(\tilde{q}_\mu | \mu, \hat{\theta}_\mu^{\text{obs}}) d\tilde{q}_\mu \quad , \quad (6.6)$$

2454

$$1 - p_b = (\tilde{q}_\mu \geq \tilde{q}_\mu^{\text{obs}} | \text{background only}) = \int_{\tilde{q}_0^{\text{obs}}}^{\infty} f(\tilde{q}_\mu | 0, \hat{\theta}_0^{\text{obs}}) d\tilde{q}_\mu \quad . \quad (6.7)$$

2455 According to these definitions, p_μ and p_b can be identified with CL_{s+b} and $1 - \text{CL}_b$, 2456 respectively. The $\text{CL}_s(\mu)$ is calculated using the following ratio:

$$\text{CL}_s(\mu) = \frac{\text{CL}_{s+b}}{\text{CL}_b} = \frac{p_\mu}{1 - p_b} \quad . \quad (6.8)$$

2457 If, for a given signal strength μ , $\text{CL}_s \leq \alpha$, then the hypothesis is excluded with a $(1 - \alpha)$ 2458 confidence level (CL). For instance, if one wants to quote the upper limit on μ with a 95% 2459 CL, the signal strength has to be adjusted until $\text{CL}_s = 0.05$.

2460 The expected median upper limit, as well as the $\pm 1\sigma$ (68% CL) and $\pm 2\sigma$ (95% CL) 2461 bands, are determined generating a large amount of pseudo-data in the background only 2462 hypothesis and calculating CL_s and the 95% CL upper limit for each of them, as if they 2463 were real data. Then the cumulative distribution of the 95% CL upper limits is built and 2464 the median expected value is identified as the value at which the cumulative distribution 2465 crosses the 50% quantile. The $\pm 1\sigma$ ($\pm 2\sigma$) band is defined by the values at which the 2466 cumulative distribution crosses the 16% (2.5%) and 84% (97.5%) quantiles.

2467 In order to assess the sensitivity of the analysis, the expected upper exclusion limits at 2468 95% CL on the signal strength are shown in Fig. 6.7 for the three jet categories separately. 2469 For a given mass of the resonance, the limits are derived assuming a signal decay width 2470 $\Gamma' = \Gamma_{\text{SM}}$ and a cross section equal to the one expected from a SM Higgs boson at that 2471 mass. The other decay width hypothesis have also been tested, showing a very similar 2472 expected exclusion limit, suggesting that this analysis is not strongly sensitive to variations 2473 of the resonance decay width.

2474 The 0 jets category is the most sensitive especially in the low mass region, while for 2475 very large masses of the resonance the 1 jet and VBF categories start being important. 2476 This is explained mainly by the fact that the VBF contribution increases, with respect to 2477 ggH, as the mass increases. The expected exclusion limit on the signal strength after the 2478 combination of the three categories is shown in Fig. 6.8. Comparing the limits in the single 2479 categories with the combination of the three it is evident how the higher jet multiplicity 2480 categories help in improving the results for large values of M_X .

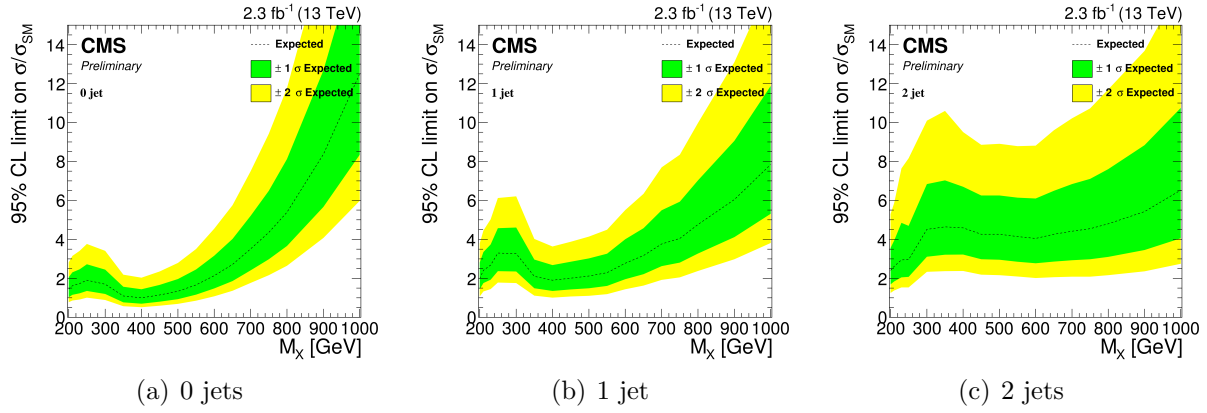


Figure 6.7.: Expected exclusion upper limits at 95% CL on the signal strength in the three categories, as a function of the resonance mass. The dashed line corresponds to median upper limit, while the green and yellow regions represent the $\pm 1\sigma$ and $\pm 2\sigma$ uncertainty bands, respectively. Limits are derived assuming a SM Higgs boson cross section and decay width for each mass point.

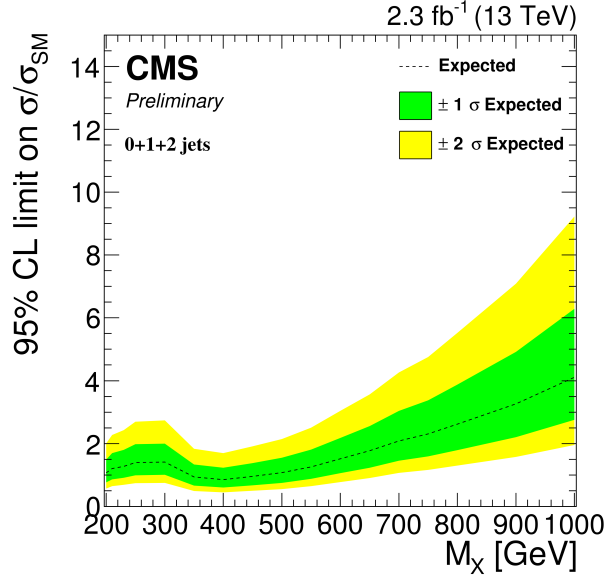


Figure 6.8.: Expected exclusion upper limit at 95% CL on the signal strength for the combination of the three categories, as a function of the resonance mass. The dashed line corresponds to median upper limit, while the green and yellow regions represent the $\pm 1\sigma$ and $\pm 2\sigma$ uncertainty bands. The limit is derived assuming a SM Higgs boson cross section and decay width for each mass point.

2481 6.7. Results

2482 The m_T^i distributions for the signal region after the full analysis selection are shown
 2483 in Fig. 6.9 for the three jet categories. Two different signal hypotheses corresponding

2484 to $M_X = 400 \text{ GeV}$ and $M_X = 800 \text{ GeV}$ are shown superimposed on the background for
 2485 comparison.

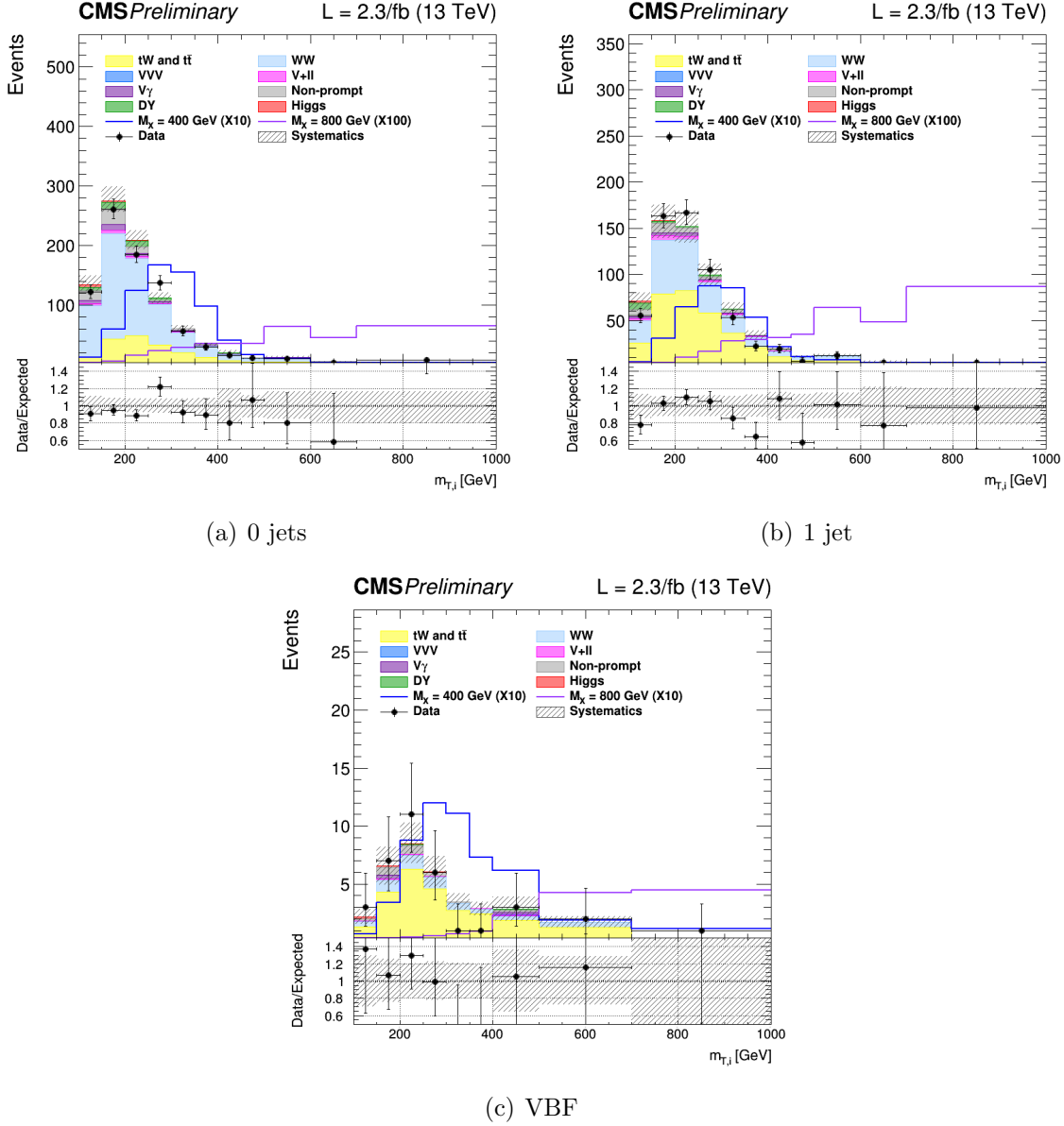


Figure 6.9.: Distributions of $m_{T,i}^i$ in the signal region for the 0 jets, 1 jet and VBF categories. Background normalisations correspond to the pre-fit value. Signal contributions for two mass hypotheses, $M_X = 400 \text{ GeV}$ and $M_X = 800 \text{ GeV}$, are shown superimposed on the background and scaled to facilitate the comparison.

2486 For every mass point from 200 GeV up to 1 TeV the observed p-value and the 95% CL
 2487 upper exclusion limit are calculated for five hypothesis of the signal width. The observed

²⁴⁸⁸ p-value as a function of the resonance mass for the combination of the three jet categories
²⁴⁸⁹ is shown in Table 6.3.

Table 6.3.: Observed p-value and corresponding significance (set to 0 in case of underfluctuations of the observed number of events) for the combination of the three jet categories for different resonance masses. Different values of the signal width are shown.

Mass [GeV]	$\Gamma = 0.09 \times \Gamma_{SM}$ p-value (signif.)	$\Gamma = 0.25 \times \Gamma_{SM}$ p-value (signif.)	$\Gamma = 0.49 \times \Gamma_{SM}$ p-value (signif.)	$\Gamma = \Gamma_{SM}$ p-value (signif.)
200	0.50 (0)	0.50 (0)	0.50 (0)	0.56 (0)
210	0.58 (0)	0.45 (0.1)	0.35 (0.4)	0.24 (0.7)
230	0.21 (0.8)	0.22 (0.8)	0.23 (0.7)	0.26 (0.6)
250	0.29 (0.5)	0.20 (0.8)	0.15 (1.0)	0.12 (1.2)
300	0.014 (2.2)	0.015 (2.2)	0.016 (2.1)	0.018 (2.1)
350	0.16 (1.0)	0.17 (1.0)	0.18 (0.9)	0.23 (0.7)
400	0.50 (0)	0.49 (0)	0.49 (0)	0.57 (0)
450	0.51 (0)	0.50 (0)	0.50 (0)	0.52 (0)
500	0.50 (0)	0.51 (0)	0.50 (0)	0.52 (0)
550	0.50 (0)	0.51 (0)	0.51 (0)	0.51 (0)
600	0.50 (0)	0.50 (0)	0.51 (0)	0.51 (0)
650	0.50 (0)	0.50 (0)	0.54 (0)	0.50 (0)
700	0.50 (0)	0.50 (0)	0.50 (0)	0.50 (0)
750	0.50 (0)	0.54 (0)	0.50 (0)	0.40 (0.3)
800	0.50 (0)	0.55 (0)	0.39 (0.3)	0.29 (0.6)
900	0.29 (0.6)	0.27 (0.6)	0.24 (0.7)	0.22 (0.8)
1000	0.18 (0.9)	0.18 (0.9)	0.18 (0.9)	0.18 (0.9)

²⁴⁹⁰ In order to be independent on the particular model assumed for the signal cross section,
²⁴⁹¹ the results are interpreted as exclusion limits on $\sigma \times \mathcal{B}$, where σ stands for the sum of
²⁴⁹² the ggH and VBF cross sections, and \mathcal{B} represents the $X \rightarrow WW \rightarrow 2\ell 2\nu$ branching ratio
²⁴⁹³ including all lepton flavours. The expected and observed upper exclusion limits on $\sigma \times \mathcal{B}$
²⁴⁹⁴ for $\Gamma' = \Gamma_{SM}$ are shown in Fig. 6.10.

²⁴⁹⁵ A mild excess is observed in the 0 jets category and, more evident, in the 1 jet category
²⁴⁹⁶ around 250-300 GeV. A deficit is instead in the VBF category around 250 GeV, which is
²⁴⁹⁷ mainly due to an underfluctuation of the background. This effect can be understood looking
²⁴⁹⁸ at the VBF shape in Fig. 6.9, where two adjacent data points, corresponding to the fifth

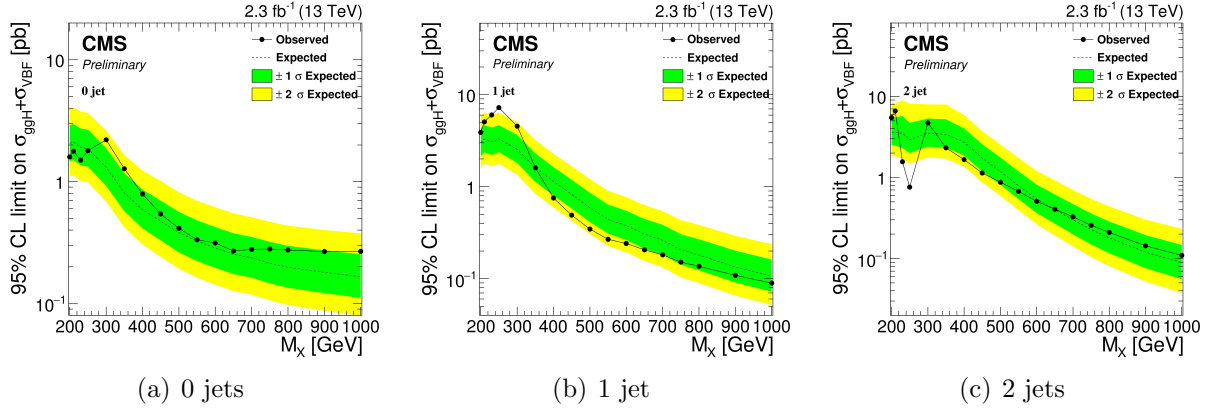


Figure 6.10.: Expected and observed exclusion upper limits at 95% CL on $\sigma \times \mathcal{B}$ in the three categories, as a function of the resonance mass. The dashed line corresponds to median upper limit, while the green and yellow regions represent the $\pm 1\sigma$ and $\pm 2\sigma$ uncertainty bands, respectively. The dotted line represents the observed limit. Limits are derived assuming $\Gamma' = \Gamma_{\text{SM}}$ for each mass point.

and sixth bins, clearly underfluctuate with respect to the background prediction, causing the dip in the observed limit.

The exclusion limit resulting from the combination of the three categories is shown in Fig. 6.11, for the five Γ' hypotheses discussed before. From the combined exclusion limits no significant evidence of a deviation from the SM prediction is observed. The presence of a scalar resonance with $\sigma \times \mathcal{B}$ higher than the values reported in Fig. 6.11 is thus excluded with a 95% CL for masses ranging from 200 GeV up to 1 TeV.

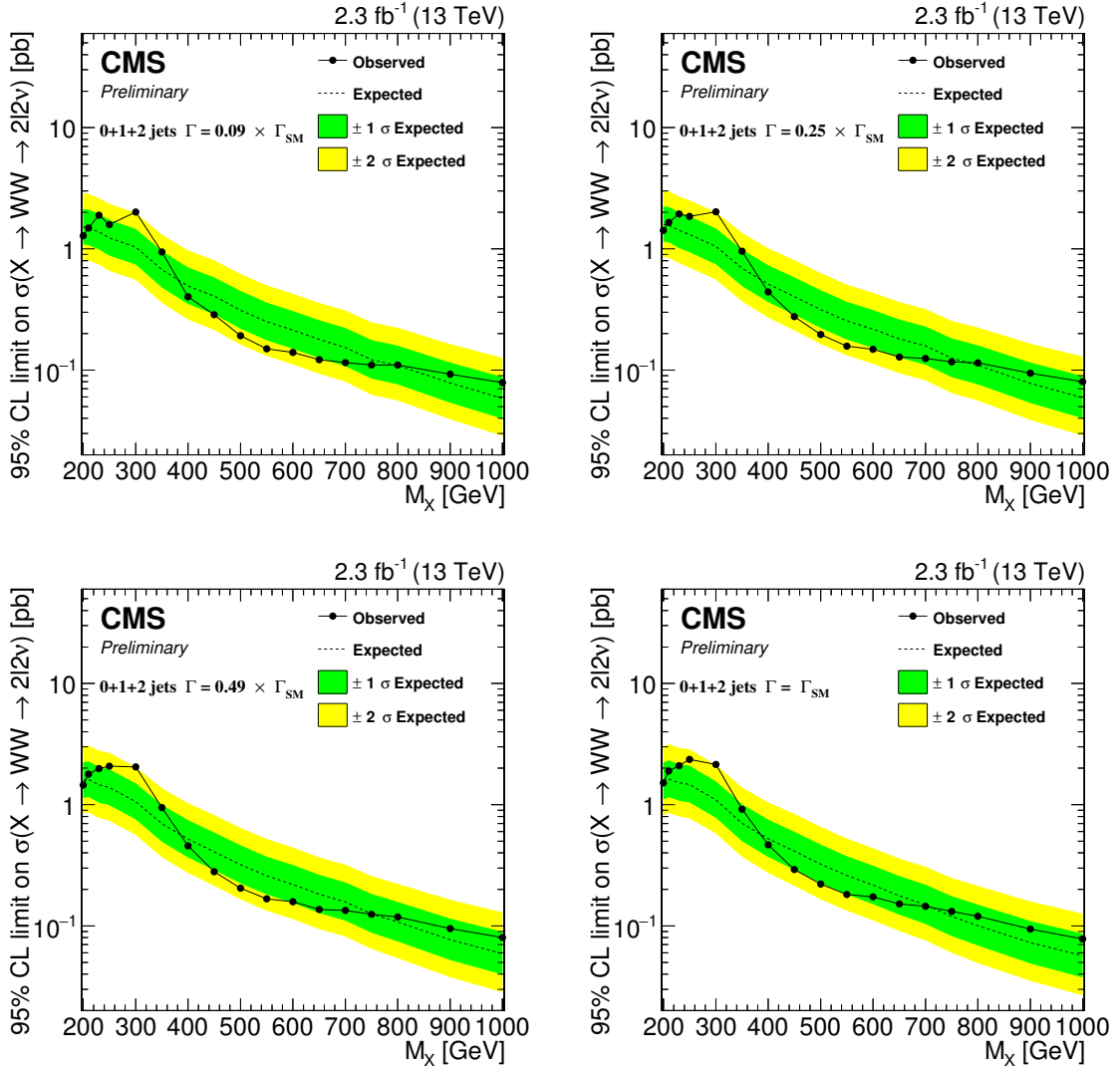


Figure 6.11.: Expected and observed exclusion limits at 95% CL on $\sigma \times \mathcal{B}$ for the combination of the three jet categories as a function of the resonance mass. The black dotted line corresponds to the observed value while the yellow and green bands represent the $\pm 1\sigma$ and $\pm 2\sigma$ uncertainties respectively. Limits are shown for four hypotheses of the resonance decay width.

Chapter 7.

Conclusions

Appendix A.

2507 Fiducial region definition and 2508 optimization

2509 The fiducial region must be chosen in such a way to be as close as possible to the selections
2510 applied in the analysis, in order to reduce the model dependence in the extrapolation step.
2511 That means that for optimizing the fiducial volume definition, the efficiency has to be
2512 maximized. Another parameter entering the game is the number of fake events, in other
2513 words the number of reconstructed events which do not belong to the fiducial phase space.
2514 This parameter should instead be as small as possible. Even if we have to observe the trend
2515 of these two quantities as a function of p_T^H , we can maximize the ratio between the overall
2516 efficiency and the overall fake rate as a proxy for establishing the “goodness” of the fiducial
2517 region.

2518 Several different fiducial region definitions were tested and the results show that:

- 2519 • **of cut:** The fiducial region definition must include only the opposite flavor combination
2520 including one electron and one muon. If we include also the combinations involving
2521 τ 's the efficiency falls down.
- 2522 • **Lepton cut:** Since the resolution on lepton transverse momentum is good, there is no
2523 need to loosen the cuts related these variables, i.e. we can use the same cuts defined
2524 in the analysis selection ($p_T^{\ell,1} > 20 \text{ GeV}$, $p_T^{\ell,2} > 10 \text{ GeV}$).
- 2525 • **Di-lepton p_T cut:** As stated in the previous point, there is no need to loosen this
2526 cut, so we kept the same value as the analysis selection, i.e. $p_T^{\ell\ell} > 30 \text{ GeV}$.
- 2527 • **Di-lepton mass cut:** $m_{\ell\ell} > 12 \text{ GeV}$ as discussed before.
- 2528 • **neutrino pair p_T cut:** Since the resolution on the measurement of the missing
2529 transverse energy is poor, the neutrino pair cut should not be included in the definition
2530 of the fiducial region, because it would increase the fake rate without increasing the
2531 efficiency, thus resulting in a lower ratio between overall efficiency and fake rate.
- 2532 • **m_T cut:** Also the m_T cut that we have in the analysis selection, i.e. $m_T > 60 \text{ GeV}$,
2533 should be loosened or removed because it involves neutrinos and then increase the
2534 fake rate. We decided eventually to keep this cut, loosening it to 50 GeV, because in
2535 addition to increase the number of fake events, it increases the efficiency as well.

2536 The fake rate and the efficiency as a function of p_T^H after the optimization discussed
2537 before are shown in figure A.1. To obtain these plots the fiducial region was modified

2538 adding in sequence the various cuts and computing the efficiency and the fake rate each
 2539 time. In that way we can asses the composition of those distributions.

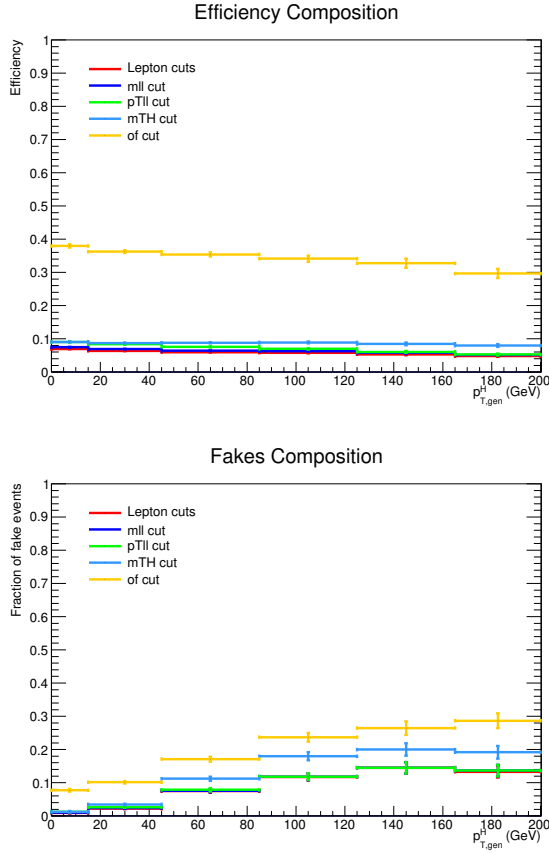


Figure A.1.: Efficiency and fake rate as a function on Higgs transverse momentum. The plots correspond to the optimized fiducial region definition and show the effect of adding each of the mentioned cuts in sequence.

2540 The efficiency and fraction of fake events have been measured also as a function of the
 2541 E_T^{miss} and m_T cuts in the fiducial region. Since these two variables are correlated, the
 2542 results are reported as two-dimensional histograms. In Fig. A.2 are reported the efficiency
 2543 and fraction of fake events for these two variables.

2544 The criterion adopted to define the fiducial region is a tradeoff between having a large
 2545 efficiency and a small fraction of fake events. Especially when looking at the low resolution
 2546 variables, such as E_T^{miss} and m_T , a suitable figure of merit has to be chosen for the estimation
 2547 of the best cuts. Several different figures of merit have been checked, such as ϵ/f , $\epsilon - f$
 2548 and $(1 - f)/\epsilon$. The results for these three different figures of merit are shown in Fig. A.3 as
 2549 a function of the E_T^{miss} and m_T cuts in the fiducial region.

2550 Following the same criterion, similar plots as above have been obtained for an alternative
 2551 model, given by varying up the ggH/VBF ratio within the experimental uncertainties. The

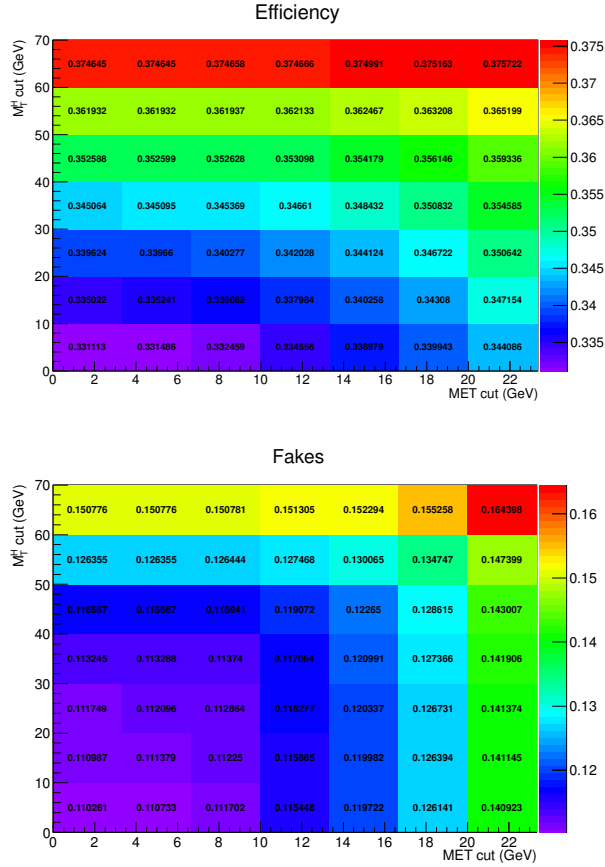


Figure A.2.: Efficiency and fake rate as a function of E_T^{miss} and m_T cuts in the fiducial region.

2552 results, shown in Fig. A.4 and Fig. A.5, show a similar trend with respect to the model
 2553 with nominal ggH/VBF ratio.

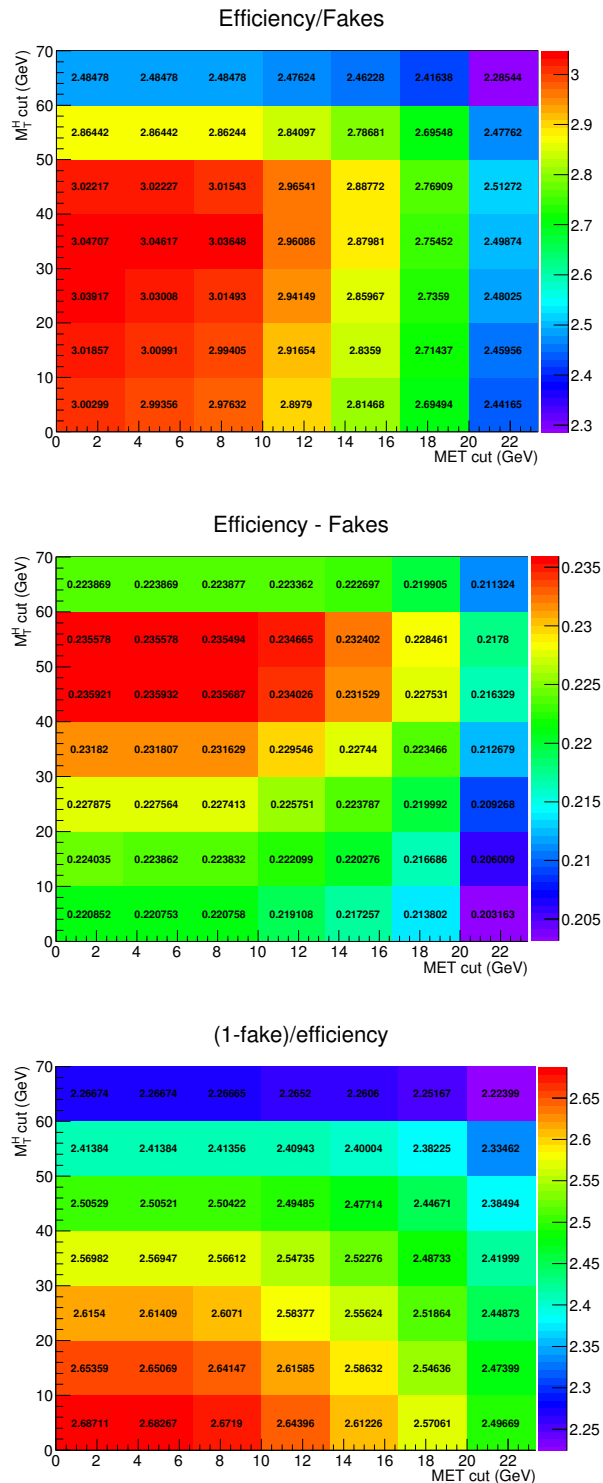


Figure A.3.: Different figures of merit as a function of E_T^{miss} and m_T cuts in the fiducial region.

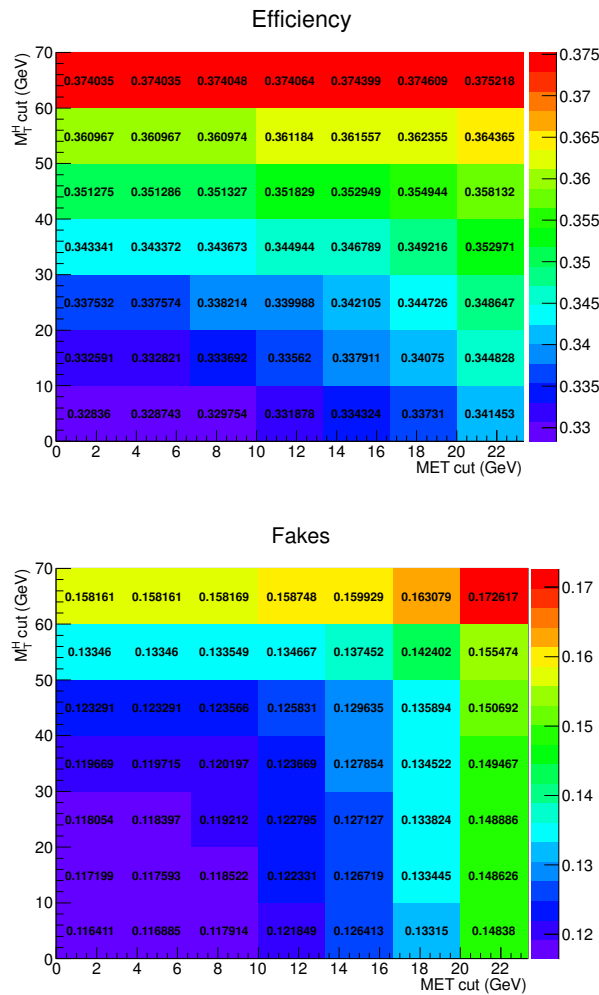


Figure A.4.: Efficiency and fake rate as a function of E_T^{miss} and m_T cuts in the fiducial region, for the alternative model with an up variation of the ggH/VBF ratio.

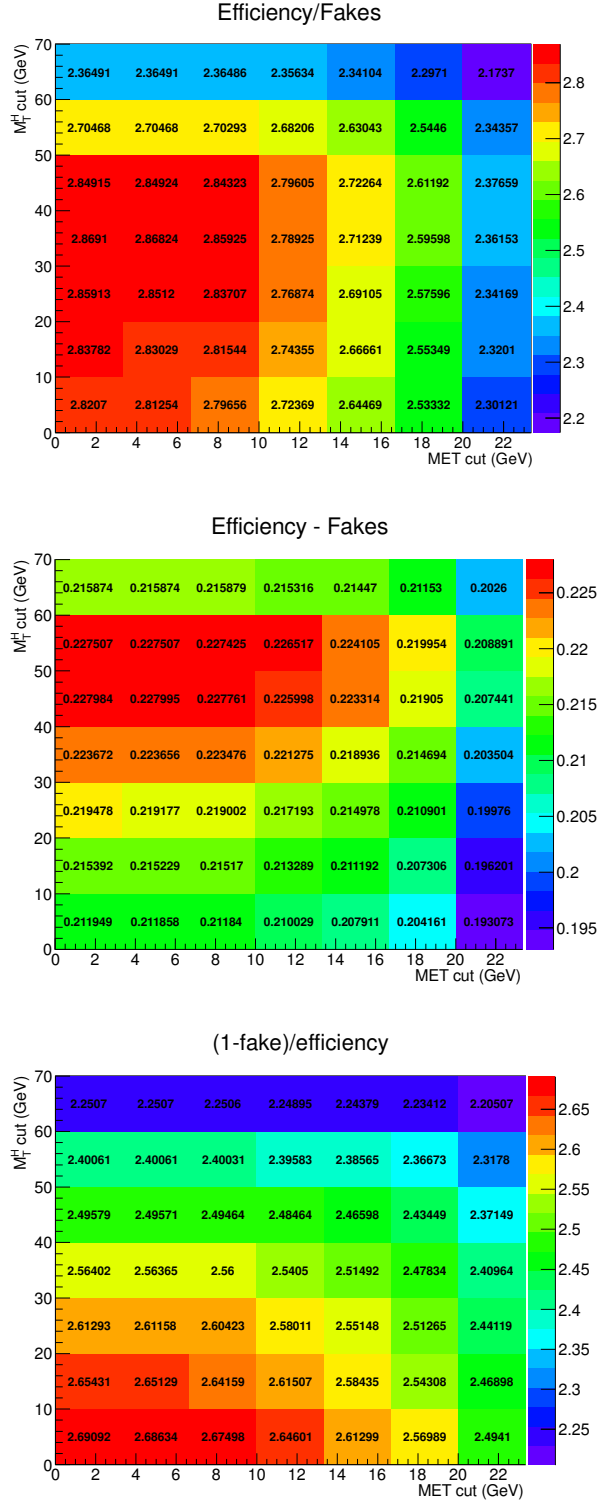


Figure A.5.: Different figures of merit as a function of E_T^{miss} and m_T cuts in the fiducial region, for the alternative model with an up variation of the ggH/VBF ratio.

2555

Bibliography

- 2556 [1] Thomas Sven Pettersson and P Lefèvre. *The Large Hadron Collider: conceptual
2557 design*. Tech. rep. CERN-AC-95-05-LHC. Oct. 1995. URL: <http://cds.cern.ch/record/291782>.
- 2559 [2] Oliver Sim Brüning et al. *LHC Design Report*. Geneva: CERN, 2004. URL: <http://cds.cern.ch/record/782076>.
- 2561 [3] Oliver Sim Brüning et al. *LHC Design Report*. Geneva: CERN, 2004. URL: <http://cds.cern.ch/record/815187>.
- 2563 [4] Michael Benedikt et al. *LHC Design Report*. Geneva: CERN, 2004. URL: <http://cds.cern.ch/record/823808>.
- 2565 [5] *LEP design report*. By the LEP Injector Study Group. Geneva: CERN, 1983. URL:
2566 <http://cds.cern.ch/record/98881>.
- 2567 [6] *LEP design report*. Copies shelved as reports in LEP, PS and SPS libraries. Geneva:
2568 CERN, 1984. URL: <http://cds.cern.ch/record/102083>.
- 2569 [7] Carlo Wyss. *LEP design report, v.3: LEP2*. Vol. 1-2 publ. in 1983-84. Geneva: CERN,
2570 1996. URL: <http://cds.cern.ch/record/314187>.
- 2571 [8] S. Chatrchyan et al. “The CMS experiment at the CERN LHC”. In: *JINST* 3 (2008),
2572 S08004. DOI: [10.1088/1748-0221/3/08/S08004](https://doi.org/10.1088/1748-0221/3/08/S08004).
- 2573 [9] G. Aad et al. “The ATLAS Experiment at the CERN Large Hadron Collider”. In:
2574 *JINST* 3 (2008), S08003. DOI: [10.1088/1748-0221/3/08/S08003](https://doi.org/10.1088/1748-0221/3/08/S08003).
- 2575 [10] A. Augusto Alves Jr. et al. “The LHCb Detector at the LHC”. In: *JINST* 3 (2008),
2576 S08005. DOI: [10.1088/1748-0221/3/08/S08005](https://doi.org/10.1088/1748-0221/3/08/S08005).
- 2577 [11] K. Aamodt et al. “The ALICE experiment at the CERN LHC”. In: *JINST* 3 (2008),
2578 S08002. DOI: [10.1088/1748-0221/3/08/S08002](https://doi.org/10.1088/1748-0221/3/08/S08002).
- 2579 [12] G. Anelli et al. “The TOTEM experiment at the CERN Large Hadron Collider”. In:
2580 *JINST* 3 (2008), S08007. DOI: [10.1088/1748-0221/3/08/S08007](https://doi.org/10.1088/1748-0221/3/08/S08007).
- 2581 [13] O. Adriani et al. “The LHCf detector at the CERN Large Hadron Collider”. In:
2582 *JINST* 3 (2008), S08006. DOI: [10.1088/1748-0221/3/08/S08006](https://doi.org/10.1088/1748-0221/3/08/S08006).
- 2583 [14] *The CMS magnet project: Technical Design Report*. Technical Design Report CMS.
2584 Geneva: CERN, 1997. URL: <http://cds.cern.ch/record/331056>.
- 2585 [15] *The CMS electromagnetic calorimeter project: Technical Design Report*. Technical
2586 Design Report CMS. Geneva: CERN, 1997. URL: <http://cds.cern.ch/record/349375>.

- [16] Philippe Bloch et al. *Changes to CMS ECAL electronics: addendum to the Technical Design Report*. Technical Design Report CMS. Geneva: CERN, 2002. URL: <http://cds.cern.ch/record/581342>.
- [17] *The CMS hadron calorimeter project: Technical Design Report*. Technical Design Report CMS. Geneva: CERN, 1997. URL: <http://cds.cern.ch/record/357153>.
- [18] *The CMS muon project: Technical Design Report*. Technical Design Report CMS. Geneva: CERN, 1997. URL: <http://cds.cern.ch/record/343814>.
- [19] S. Dasu et al. “CMS. The TriDAS project. Technical design report, vol. 1: The trigger systems”. In: (2000).
- [20] Sergio Cittolin, Attila Rácz, and Paris Sphicas. *CMS The TriDAS Project: Technical Design Report, Volume 2: Data Acquisition and High-Level Trigger. CMS trigger and data-acquisition project*. Technical Design Report CMS. Geneva: CERN, 2002. URL: <http://cds.cern.ch/record/578006>.
- [21] CMS Collaboration. *Particle-Flow Event Reconstruction in CMS and Performance for Jets, Taus, and E_T^{miss}* . CMS Physics Analysis Summary CMS-PAS-PFT-09-001. 2009. URL: <http://cdsweb.cern.ch/record/1194487>.
- [22] Serguei Chatrchyan et al. “Description and performance of track and primary-vertex reconstruction with the CMS tracker”. In: *JINST* 9.10 (2014), P10009. DOI: 10.1088/1748-0221/9/10/P10009. arXiv: 1405.6569 [physics.ins-det].
- [23] Pierre Billoir and S. Qian. “Simultaneous pattern recognition and track fitting by the Kalman filtering method”. In: *Nucl. Instrum. Meth. A* 294 (1990), p. 219. DOI: 10.1016/0168-9002(90)91835-Y.
- [24] M. Spira et al. “Higgs boson production at the LHC”. In: *Nucl. Phys. B* 453 (1995), pp. 17–82. DOI: 10.1016/0550-3213(95)00379-7. arXiv: hep-ph/9504378 [hep-ph].
- [25] Robert Harlander and Philipp Kant. “Higgs production and decay: Analytic results at next-to-leading order QCD”. In: *JHEP* 12 (2005), p. 015. DOI: 10.1088/1126-6708/2005/12/015. arXiv: hep-ph/0509189 [hep-ph].
- [26] V. Ravindran, J. Smith, and W. L. van Neerven. “NNLO corrections to the total cross-section for Higgs boson production in hadron hadron collisions”. In: *Nucl. Phys. B* 665 (2003), pp. 325–366. DOI: 10.1016/S0550-3213(03)00457-7. arXiv: hep-ph/0302135 [hep-ph].
- [27] Stefano Catani and Massimiliano Grazzini. “An NNLO subtraction formalism in hadron collisions and its application to Higgs boson production at the LHC”. In: *Phys. Rev. Lett.* 98 (2007), p. 222002. DOI: 10.1103/PhysRevLett.98.222002. arXiv: hep-ph/0703012 [hep-ph].
- [28] Charalampos Anastasiou et al. “Higgs Boson Gluon-Fusion Production in QCD at Three Loops”. In: *Phys. Rev. Lett.* 114 (2015), p. 212001. DOI: 10.1103/PhysRevLett.114.212001. arXiv: 1503.06056 [hep-ph].

- [29] X. Chen et al. “NNLO QCD corrections to Higgs boson production at large transverse momentum”. In: (2016). arXiv: 1607.08817 [hep-ph].
- [30] Massimiliano Grazzini and Hayk Sargsyan. “Heavy-quark mass effects in Higgs boson production at the LHC”. In: *JHEP* 09 (2013), p. 129. DOI: 10.1007/JHEP09(2013)129. arXiv: 1306.4581 [hep-ph].
- [31] Aleksandr Azatov and Ayan Paul. “Probing Higgs couplings with high p_T Higgs production”. In: *JHEP* 01 (2014), p. 014. DOI: 10.1007/JHEP01(2014)014. arXiv: 1309.5273 [hep-ph].
- [32] Robert V. Harlander and Tobias Neumann. “Probing the nature of the Higgs-gluon coupling”. In: *Phys. Rev. D* 88 (2013), p. 074015. DOI: 10.1103/PhysRevD.88.074015. arXiv: 1308.2225 [hep-ph].
- [33] David Marzocca, Marco Serone, and Jing Shu. “General Composite Higgs Models”. In: *JHEP* 08 (2012), p. 013. DOI: 10.1007/JHEP08(2012)013. arXiv: 1205.0770 [hep-ph].
- [34] Andrea Banfi, Adam Martin, and Veronica Sanz. “Probing top-partners in Higgs+jets”. In: *JHEP* 08 (2014), p. 053. DOI: 10.1007/JHEP08(2014)053. arXiv: 1308.4771 [hep-ph].
- [35] Georges Aad et al. “Fiducial and differential cross sections of Higgs boson production measured in the four-lepton decay channel in pp collisions at $\sqrt{s} = 8$ TeV with the ATLAS detector”. In: *Phys. Lett. B* 738 (2014), p. 234. DOI: 10.1016/j.physletb.2014.09.054. arXiv: 1408.3226 [hep-ex].
- [36] Georges Aad et al. “Measurements of fiducial and differential cross sections for Higgs boson production in the diphoton decay channel at $\sqrt{s} = 8$ TeV with ATLAS”. In: *JHEP* 09 (2014), p. 112. DOI: 10.1007/JHEP09(2014)112. arXiv: 1407.4222 [hep-ex].
- [37] Georges Aad et al. “Measurements of the Total and Differential Higgs Boson Production Cross Sections Combining the $H \rightarrow \gamma\gamma$ and $H \rightarrow ZZ^* \rightarrow 4\ell$ Decay Channels at $\sqrt{s} = 8$ TeV with the ATLAS Detector”. In: *Phys. Rev. Lett.* 115 (2015), p. 091801. DOI: 10.1103/PhysRevLett.115.091801. arXiv: 1504.05833 [hep-ex].
- [38] Vardan Khachatryan et al. “Measurement of differential cross sections for Higgs boson production in the diphoton decay channel in pp collisions at $\sqrt{s} = 8$ TeV”. In: *Eur. Phys. J. C* 76 (2016), p. 13. DOI: 10.1140/epjc/s10052-015-3853-3. arXiv: 1508.07819 [hep-ex].
- [39] Vardan Khachatryan et al. “Measurement of differential and integrated fiducial cross sections for Higgs boson production in the four-lepton decay channel in pp collisions at $\sqrt{s} = 7$ and 8 TeV”. In: *JHEP* 04 (2016), p. 005. DOI: 10.1007/JHEP04(2016)005. arXiv: 1512.08377 [hep-ex].

- [40] LHC Higgs Cross Section Working Group. *Handbook of LHC Higgs cross sections: 3. Higgs properties*. CERN Report CERN-2013-004. 2013. DOI: 10.5170/CERN-2013-004. arXiv: 1307.1347 [hep-ph].
- [41] Serguei Chatrchyan et al. “Measurement of Higgs boson production and properties in the WW decay channel with leptonic final states”. In: *JHEP* 01 (2014), p. 096. DOI: 10.1007/JHEP01(2014)096. arXiv: 1312.1129 [hep-ex].
- [42] G. Cowan. “A survey of unfolding methods for particle physics”. In: *Conf. Proc.* C0203181 (2002), p. 248.
- [43] Michael Krämer, Stephen Mrenna, and Davison E. Soper. “Next-to-leading order QCD jet production with parton showers and hadronization”. In: *Phys. Rev. D* 73 (2006), p. 014022. DOI: 10.1103/PhysRevD.73.014022. arXiv: hep-ph/0509127 [hep-ph].
- [44] Stefano Frixione, Paolo Nason, and Carlo Oleari. “Matching NLO QCD computations with Parton Shower simulations: the POWHEG method”. In: *JHEP* 11 (2007), p. 070. DOI: 10.1088/1126-6708/2007/11/070. arXiv: 0709.2092 [hep-ph].
- [45] Nils Lavesson and Leif Lonnblad. “Extending CKKW-merging to one-loop matrix elements”. In: *JHEP* 12 (2008), p. 070. DOI: 10.1088/1126-6708/2008/12/070. arXiv: 0811.2912 [hep-ph].
- [46] Simone Alioli et al. “NLO Higgs boson production via gluon fusion matched with shower in POWHEG”. In: *JHEP* 04 (2009), p. 002. DOI: 10.1088/1126-6708/2009/04/002. arXiv: 0812.0578 [hep-ph].
- [47] Paolo Nason and Carlo Oleari. “NLO Higgs boson production via vector-boson fusion matched with shower in POWHEG”. In: *JHEP* 02 (2010), p. 037. DOI: 10.1007/JHEP02(2010)037. arXiv: 0911.5299 [hep-ph].
- [48] Simone Alioli, Sven-Olaf Moch, and Peter Uwer. “Hadronic top-quark pair-production with one jet and parton showering”. In: *JHEP* 01 (2012), p. 137. DOI: 10.1007/JHEP01(2012)137. arXiv: 1110.5251 [hep-ph].
- [49] J. Alwall et al. “The automated computation of tree-level and next-to-leading order differential cross sections, and their matching to parton shower simulations”. In: *JHEP* 07 (2014), p. 079. DOI: 10.1007/JHEP07(2014)079. arXiv: 1405.0301 [hep-ph].
- [50] T. Binoth et al. “Gluon-induced W-boson pair production at the LHC”. In: *JHEP* 12 (2006), p. 046. DOI: 10.1088/1126-6708/2006/12/046. arXiv: hep-ph/0611170 [hep-ph].
- [51] Marco Bonvini et al. “Signal-background interference effects for $gg \rightarrow H \rightarrow W^+W^-$ beyond leading order”. In: *Phys. Rev. D* 88 (2013), p. 034032. DOI: 10.1103/PhysRevD.88.034032. arXiv: 1304.3053 [hep-ph].
- [52] Giampiero Passarino. “Higgs CAT”. In: *Eur. Phys. J. C* 74 (2014), p. 2866. DOI: 10.1140/epjc/s10052-014-2866-7. arXiv: 1312.2397 [hep-ph].

- 2703 [53] Torbjörn Sjöstrand, Stephen Mrenna, and Peter Skands. “PYTHIA 6.4 physics and
2704 manual”. In: *JHEP* 05 (2006), p. 026. DOI: 10.1088/1126-6708/2006/05/026.
2705 arXiv: hep-ph/0603175 [hep-ph].
- 2706 [54] Hung-Liang Lai et al. “Uncertainty induced by QCD coupling in the CTEQ global
2707 analysis of parton distributions”. In: *Phys. Rev. D* 82 (2010), p. 054021. DOI:
2708 10.1103/PhysRevD.82.054021. arXiv: 1004.4624 [hep-ph].
- 2709 [55] Hung-Liang Lai et al. “New parton distributions for collider physics”. In: *Phys. Rev.*
2710 *D* 82 (2010), p. 074024. DOI: 10.1103/PhysRevD.82.074024. arXiv: 1007.2241
2711 [hep-ph].
- 2712 [56] LHC Higgs Cross Section Working Group. “Handbook of LHC Higgs Cross Sections”.
2713 In: *arXiv:1101.0593* (2011).
- 2714 [57] Simone Alioli et al. “A general framework for implementing NLO calculations in
2715 shower Monte Carlo programs: the POWHEG BOX”. In: *JHEP* 06 (2010), p. 043.
2716 DOI: 10.1007/JHEP06(2010)043. arXiv: 1002.2581 [hep-ph].
- 2717 [58] S. Agostinelli et al. “GEANT4: A simulation toolkit”. In: *Nucl. Instrum. Meth. A*
2718 506 (2003), p. 250. DOI: 10.1016/S0168-9002(03)01368-8.
- 2719 [59] D. de Florian et al. “Higgs boson production at the LHC: transverse momentum
2720 resummation effects in the $H \rightarrow 2\gamma$, $H \rightarrow WW \rightarrow l\nu l\nu$ and $H \rightarrow ZZ \rightarrow 4l$ decay
2721 modes”. In: *JHEP* 06 (2012), p. 132. DOI: 10.1007/JHEP06(2012)132. arXiv:
2722 1203.6321 [hep-ph].
- 2723 [60] E. Bagnaschi et al. “Higgs production via gluon fusion in the POWHEG approach in
2724 the SM and in the MSSM”. In: *JHEP* 02 (2012), p. 088. DOI: 10.1007/JHEP02(2012)
2725 088. arXiv: 1111.2854 [hep-ph].
- 2726 [61] Stefano Actis et al. “NLO Electroweak Corrections to Higgs Boson Production at
2727 Hadron Colliders”. In: *Phys. Lett. B* 670 (2008), p. 12. DOI: 10.1016/j.physletb.
2728 2008.10.018. arXiv: 0809.1301 [hep-ph].
- 2729 [62] Stefano Catani et al. “Soft gluon resummation for Higgs boson production at hadron
2730 colliders”. In: *JHEP* 07 (2003), p. 028. DOI: 10.1088/1126-6708/2003/07/028.
2731 arXiv: hep-ph/0306211 [hep-ph].
- 2732 [63] Yanyan Gao et al. “Spin determination of single-produced resonances at hadron
2733 colliders”. In: *Phys. Rev. D* 81 (2010), p. 075022. DOI: 10.1103/PhysRevD.81.
2734 075022. arXiv: 1001.3396 [hep-ph].
- 2735 [64] Sara Bolognesi et al. “Spin and parity of a single-produced resonance at the LHC”.
2736 In: *Phys. Rev. D* 86 (2012), p. 095031. DOI: 10.1103/PhysRevD.86.095031. arXiv:
2737 1208.4018 [hep-ph].
- 2738 [65] Ian Anderson et al. “Constraining anomalous HVV interactions at proton and
2739 lepton colliders”. In: *Phys. Rev. D* 89 (2014), p. 035007. DOI: 10.1103/PhysRevD.
2740 89.035007. arXiv: 1309.4819 [hep-ph].

- [66] Torbjorn Sjöstrand, Stephen Mrenna, and Peter Z. Skands. “A Brief Introduction to PYTHIA 8.1”. In: *Comput. Phys. Commun.* 178 (2008), p. 852. DOI: 10.1016/j.cpc.2008.01.036. arXiv: 0710.3820 [hep-ph].
- [67] Vardan Khachatryan et al. “Measurement of the $t\bar{t}$ production cross section in the $e\mu$ channel in proton-proton collisions at $\sqrt{s} = 7$ and 8 TeV”. In: (2016). arXiv: 1603.02303 [hep-ex].
- [68] Stanislaw Jadach, Johann H. Kuhn, and Zbigniew Was. “TAUOLA: A Library of Monte Carlo programs to simulate decays of polarized tau leptons”. In: *Comput. Phys. Commun.* 64 (1990), p. 275. DOI: 10.1016/0010-4655(91)90038-M.
- [69] CMS Collaboration. “Standard Model Cross Sections for CMS at 7 TeV”. In: *CMS Generator Group Twiki* (2010).
- [70] John M. Campbell, R. Keith Ellis, and Ciaran Williams. “Vector boson pair production at the LHC”. In: *JHEP* 07 (2011), p. 018. DOI: 10.1007/JHEP07(2011)018. arXiv: 1105.0020 [hep-ph].
- [71] J. Ohnemus. “Order alpha-s calculations of hadronic W+- gamma and Z gamma production”. In: *Phys. Rev.* D47 (1993), pp. 940–955. DOI: 10.1103/PhysRevD.47.940.
- [72] JetMET group. “Jet energy uncertainties, https://twiki.cern.ch/twiki/bin/view/CMS/JECUncertaintySources#2012_JEC”. In: (). URL: https://twiki.cern.ch/twiki/bin/view/CMS/JECUncertaintySources%5C#2012_JEC.
- [73] Sergey Alekhin et al. “The PDF4LHC Working Group Interim Report”. 2011.
- [74] Michiel Botje et al. “The PDF4LHC Working Group Interim Recommendations”. 2011.
- [75] Richard D. Ball et al. “Impact of Heavy Quark Masses on Parton Distributions and LHC Phenomenology”. In: *Nucl. Phys. B* 849 (2011), p. 296. DOI: 10.1016/j.nuclphysb.2011.03.021. arXiv: 1101.1300 [hep-ph].
- [76] A. D. Martin et al. “Parton distributions for the LHC”. In: *Eur. Phys. J. C* 63 (2009), p. 189. DOI: 10.1140/epjc/s10052-009-1072-5. arXiv: 0901.0002 [hep-ph].
- [77] Iain W. Stewart and Frank J. Tackmann. “Theory uncertainties for Higgs and other searches using jet bins”. In: *Phys. Rev. D* 85 (2012), p. 034011. DOI: 10.1103/PhysRevD.85.034011. arXiv: 1107.2117 [hep-ph].
- [78] “Procedure for the LHC Higgs boson search combination in summer 2011”. In: (2011).
- [79] Glen Cowan et al. “Asymptotic formulae for likelihood-based tests of new physics”. In: *Eur. Phys. J. C* 71 (2011). [Erratum: Eur. Phys. J.C73,2501(2013)], p. 1554. DOI: 10.1140/epjc/s10052-011-1554-0, 10.1140/epjc/s10052-013-2501-z. arXiv: 1007.1727 [physics.data-an].
- [80] Tim Adye. “Unfolding algorithms and tests using RooUnfold”. 2011.

- [81] Andreas Hocker and Vakhtang Kartvelishvili. “SVD approach to data unfolding”. In: *Nucl. Instrum. Meth. A* 372 (1996), p. 469. DOI: 10.1016/0168-9002(95)01478-0. arXiv: hep-ph/9509307 [hep-ph].
- [82] G. D’Agostini. “A Multidimensional unfolding method based on Bayes’ theorem”. In: *Nucl. Instrum. Meth. A* 362 (1995), pp. 487–498. DOI: 10.1016/0168-9002(95)00274-X.
- [83] Vardan Khachatryan et al. “Precise determination of the mass of the Higgs boson and tests of compatibility of its couplings with the standard model predictions using proton collisions at 7 and 8 TeV”. In: *Eur. Phys. J. C* 75 (2015), p. 212. DOI: 10.1140/epjc/s10052-015-3351-7. arXiv: 1412.8662 [hep-ex].
- [84] Paolo Nason. “A New method for combining NLO QCD with shower Monte Carlo algorithms”. In: *JHEP* 11 (2004), p. 040. DOI: 10.1088/1126-6708/2004/11/040. arXiv: hep-ph/0409146 [hep-ph].
- [85] S. Bolognesi, Y. Gao and A.V. Gritsan *et al.* “JHUGen”. In: URL <http://www.pha.jhu.edu/spin/> (2011).
- [86] Gionata Luisoni et al. “ $HW^\pm/HZ + 0$ and 1 jet at NLO with the POWHEG BOX interfaced to GoSam and their merging within MiNLO”. In: *JHEP* 10 (2013), p. 083. DOI: 10.1007/JHEP10(2013)083. arXiv: 1306.2542 [hep-ph].
- [87] Tom Melia et al. “W+W-, WZ and ZZ production in the POWHEG BOX”. In: *JHEP* 11 (2011), p. 078. DOI: 10.1007/JHEP11(2011)078. arXiv: 1107.5051 [hep-ph].
- [88] T. Gehrmann et al. “ W^+W^- Production at Hadron Colliders in Next to Next to Leading Order QCD”. In: *Phys. Rev. Lett.* 113.21 (2014), p. 212001. DOI: 10.1103/PhysRevLett.113.212001. arXiv: 1408.5243 [hep-ph].
- [89] Patrick Meade, Harikrishnan Ramani, and Mao Zeng. “Transverse momentum resummation effects in W^+W^- measurements”. In: *Phys. Rev.* D90.11 (2014), p. 114006. DOI: 10.1103/PhysRevD.90.114006. arXiv: 1407.4481 [hep-ph].
- [90] Prerit Jaiswal and Takemichi Okui. “Explanation of the WW excess at the LHC by jet-veto resummation”. In: *Phys. Rev.* D90.7 (2014), p. 073009. DOI: 10.1103/PhysRevD.90.073009. arXiv: 1407.4537 [hep-ph].
- [91] John M. Campbell, R. Keith Ellis, and Ciaran Williams. “Bounding the Higgs width at the LHC: Complementary results from $H \rightarrow WW$ ”. In: *Phys. Rev.* D89.5 (2014), p. 053011. DOI: 10.1103/PhysRevD.89.053011. arXiv: 1312.1628 [hep-ph].
- [92] Richard D. Ball et al. “Parton distributions with QED corrections”. In: *Nucl. Phys.* B877 (2013), pp. 290–320. DOI: 10.1016/j.nuclphysb.2013.10.010. arXiv: 1308.0598 [hep-ph].
- [93] Richard D. Ball et al. “Unbiased global determination of parton distributions and their uncertainties at NNLO and at LO”. In: *Nucl. Phys.* B855 (2012), pp. 153–221. DOI: 10.1016/j.nuclphysb.2011.09.024. arXiv: 1107.2652 [hep-ph].

- 2817 [94] Vardan Khachatryan et al. “Event generator tunes obtained from underlying event
2818 and multiparton scattering measurements”. In: (2015). arXiv: 1512.00815 [hep-ex].
- 2819 [95] Peter Richardson and Alexandra Wilcock. “Monte Carlo Simulation of Hard Radia-
2820 tion in Decays in Beyond the Standard Model Physics in Herwig++”. In: *Eur. Phys.*
2821 *J. C74* (2014), p. 2713. DOI: 10.1140/epjc/s10052-014-2713-x. arXiv: 1303.4563
2822 [hep-ph].
- 2823 [96] J. Bellm et al. “Herwig++ 2.7 Release Note”. In: (2013). arXiv: 1310.6877 [hep-ph].
- 2824 [97] *SM Higgs production cross sections at $\sqrt{s} = 13\text{-}14 \text{ TeV}$* . <https://twiki.cern.ch/twiki/bin/view/LHCPhysics/CERNYellowReportPageAt1314TeV>.
- 2826 [98] Fabrizio Caola et al. “QCD corrections to W^+W^- production through gluon fusion”.
2827 In: *Phys. Lett. B754* (2016), pp. 275–280. DOI: 10.1016/j.physletb.2016.01.046.
2828 arXiv: 1511.08617 [hep-ph].
- 2829 [99] *NLO single-top channel cross sections*. <https://twiki.cern.ch/twiki/bin/view/LHCPhysics/SingleTopRefXsec>.
- 2831 [100] *NNLO+NNLL top-quark-pair cross sections*. <https://twiki.cern.ch/twiki/bin/view/LHCPhysics/TtbarNNLO>.
- 2833 [101] *Procedure for the LHC Higgs boson search combination in Summer 2011*. Tech. rep.
2834 CMS-NOTE-2011-005. ATL-PHYS-PUB-2011-11. Geneva: CERN, Aug. 2011.
- 2835 [102] *LHC Higgs Cross Section Working Group*. <https://twiki.cern.ch/twiki/bin/view/LHCPhysics/LHCHXSWG>.
- 2837 [103] Jon Butterworth et al. “PDF4LHC recommendations for LHC Run II”. In: *J. Phys.*
2838 *G43* (2016), p. 023001. DOI: 10.1088/0954-3899/43/2/023001. arXiv: 1510.03865
2839 [hep-ph].
- 2840 [104] Vardan Khachatryan et al. “Search for a Higgs Boson in the Mass Range from 145
2841 to 1000 GeV Decaying to a Pair of W or Z Bosons”. In: *JHEP* 10 (2015), p. 144.
2842 DOI: 10.1007/JHEP10(2015)144. arXiv: 1504.00936 [hep-ex].
- 2843 [105] G. C. Branco et al. “Theory and phenomenology of two-Higgs-doublet models”.
2844 In: *Phys. Rept.* 516 (2012), p. 1. DOI: 10.1016/j.physrep.2012.02.002. arXiv:
2845 1106.0034 [hep-ph].
- 2846 [106] N. Craig and T. Scott. “Exclusive signals of an extended Higgs sector”. In: *JHEP*
2847 11 (2012), p. 083. DOI: 10.1007/JHEP11(2012)083. arXiv: 1207.4835 [hep-ph].
- 2848 [107] H. Haber and O. Stal. “New LHC benchmarks for the CP-conserving two-Higgs-
2849 doublet model”. In: *Eur. Phys. J. C* 75 (2015), p. 491. DOI: 10.1140/epjc/s10052-
2850 015-3697-x. arXiv: 1507.04281 [hep-ph].
- 2851 [108] Suyong Choi, Sunghoon Jung, and P. Ko. “Implications of LHC data on 125 GeV
2852 Higgs-like boson for the Standard Model and its various extensions”. In: *JHEP* 1310
2853 (2013), p. 225. DOI: 10.1007/JHEP10(2013)225. arXiv: 1307.3948.

- 2854 [109] Tania Robens and Tim Stefaniak. “Status of the Higgs singlet extension of the
2855 standard model after LHC run 1”. In: *Eur. Phys. J. C* 75 (2015), p. 105. DOI:
2856 10.1140/epjc/s10052-015-3323-y. arXiv: 1501.02234 [hep-ph].
- 2857 [110] Johan Alwall et al. “Comparative study of various algorithms for the merging of
2858 parton showers and matrix elements in hadronic collisions”. In: *Eur. Phys. J. C* 53
2859 (2008), pp. 473–500. DOI: 10.1140/epjc/s10052-007-0490-5. arXiv: 0706.2569
2860 [hep-ph].
- 2861 [111] Massimiliano Grazzini. “NNLO predictions for the Higgs boson signal in the $H \rightarrow WW \rightarrow$
2862 $\ell\nu\ell\nu$ and $H \rightarrow ZZ \rightarrow 4\ell$ decay channels”. In: *JHEP* 02 (2008), p. 043. DOI: 10.1088/
2863 1126-6708/2008/02/043. arXiv: 0801.3232 [hep-ph].
- 2864 [112] Vardan Khachatryan et al. “Measurement of the differential cross section for top
2865 quark pair production in pp collisions at $\sqrt{s} = 8$ TeV”. In: *Eur. Phys. J. C* 75.11
2866 (2015), p. 542. DOI: 10.1140/epjc/s10052-015-3709-x. arXiv: 1505.04480
2867 [hep-ex].

